(LMSC/D834896) COMPACT MAGNETOGRAPH Final Report (Lockheed Missiles and Space Co.) 98 p HC A05/MF A01 CSCL 14B

N82-29578

Unclas

G3/35 15229

LOCKHEED

MISSILES & SPACE COMPANY, INC. • SUNNYVALE, CALIFORNIA

LMSC/D834896

Final Report

COMPACT MAGNETOGRAPH
Contract No. NASW-3457
February, 1982

Alan M. Title
Bruce A. Gillespie
James W. Mosher

SUMMARY

A study of the problems of a compact magnetograph has been carried out. On the basis of the study, an optimal compact magnetograph has been constructed and the ability to detect magnetic fields, verified. The problem of the coupling of magnetic, velocity, and thermal affects has been a primary driver for the design. To this end, a novel split Fabry-Perot etalon was specially fabricated as the primary wavelength selector.

COMPACT MAGNETOGRAPH VERIFICATION PROGRAM

1. Introduction

The purpose of this study was to verify the concept of a compact magnetograph system based on solid Fabry-Perot interferometers as the spectral isolation elements. The first step in the verification process was a detailed study of the theory of operation of several Fabry-Perot systems, the suitability of various magnetic lines, signal levels expected for different modes of operation, and the optimal detector systems. The study was carried out by Dr. James Mosher and is the appendix of this report.

The Mosher study was quite complete and highly influenced the direction of the experimental phases of the program. In particular, it emphasized the severe requirements that the lack of a polarization modulator placed upon the electronic signal chain. The original concept for the magnetograph did not include a modulator because of the reliability and high voltage problems. However, because of the study, a number of approaches for modulation were investigated experimentally. As a result the PLZT modulator was chosen as a satisfactory component with both high reliability and relatively low voltage requirements. Another major problem that was focussed by the Mosher report was the coupled issues of thermal control, line centering, and line offset because of solar rotation and spacecraft velocity. To a large extent the thermal, line centering, and velocity offset problems were solved by a novel Fabry-Perot configuration that was not considered in the original report, but was suggested privately by Mosher in the form of a sketch of the "ideal magnetograph."

Section two of this report discusses the magnetograph configuration decided upon for test. Much of the justification for the work described in section two is contained in the appendix, which is the Mosher report.

2. Compact Magnetograph Test Design

2.1 Optical System

Shown in Figure 1 is the optical layout of the compact magnetograph test system. Figure 2 shows a photograph of the system on the Lockheed echelle spectrograph optical bench. The magnetograph was fed by a 20-centimeter diameter heliostat which normally is used to feed a 2-meter echelle spectrophotometer. The entrance slit of the spectrograph is visible at the right-hand edge of the photograph. The location of the magnetograph on the spectrometer optical bench allowed easy verification of spectral alignment and operation of the magnetograph system.

In the order that the light strikes them, the components of the magnetograph and their functions are:

1. Objective. The 127 cm focal length objective serves to form a solar image of convenient size in the plane of the field stop. The image scale in the focal plane is 6.16 microns per arcsecond.

2. Field Stop. The field stop serves to define the magnetograph sample region. Apertures in the size range from 25 to 250 microns were tested. This corresponds to solar regions from 4 to 40 arcseconds in diameter.

3. Collimating Field Lens. The field lens is positioned its focal length from the field stop. The center line of the optical system passes through both the center of the hole in the stop and the field lens. The angle the aperture subtends at the field stop determines the spread of the beam from the stop. The size of the field lens must be sufficient to gather all the light that passes through the aperture, that is, the diameter of the field lens, D_f, must be

$$D_f = A + \frac{D_o}{f_o} f_f$$

where D_0 is the diameter of the objective, f_f and f_0 are the focal lengths of field lens and objective, and A is the size of the aperture hole.

4. Modulator. The modulator is an electrically driven waveplate which can be driven $\pm\lambda/4$ at 6302 (0-200 volts). Together with the polarizing prism the modulator provides switching between analysis for right and left circularly polarized light. It also allows analysis for linear polarization when off or at $\lambda/2$.

5. Blocking Filter. The blocking filter isolates the magnetic sensitive line λ6302 and has a FWHM of 1.3 Å. The FWHM is sufficiently narrow to isolate a single passband pair of the Fabry-Perot. The blocking filter is operated in a temperature controlled oven. The control is to $\pm.1^0$C which corresponds to ±.007 Å wavelength.

6. Polarizing Prism Assembly. The polarizing prism is of the McNeille type. It passes p wave light, light polarized parallel to the plane of incidence, and reflects s wave light, light polarized perpendicular to the plane of incidence. The right angle prism redirects the s wave light parallel to the p wave but displaced about one centimeter. When the modulator acts as a quarter waveplate at 45^0 to the p direction, it converts right (left) circularly polarized light to linearly polarized parallel to the p (s) directions. Switching the waveplate to $-\lambda/4$ converts left (right) circularly polarized light to linearly polarized light parallel to the p (s) direction. Therefore, the combination of waveplate and prism produces a pair of beams which pass either RCP or LCP and can be switched to the orthogonal states on command.

7. Fabry-Perot. The Fabry-Perot interferometer used in this system is, to the best of our knowledge, unique. It is essentially two separate etalons on a single substrate. Each of the etalons produces a standard Fabry-Perot channel spectrum with 90 mÅ FWHM and 1.4 Å interorder separation. However, the channel spectra are separated from each other by 170 mÅ. The pair of etalons are adjacent along a diameter of a 50-cm diameter disk; that is, the etalons are D shaped. When either of

the D's are placed in front of a spectrograph slit, a normal channel spectrum is observed. Moving the substrate to observe the other D causes a similar spectrum but shifted 170 mÅ. If the subtrate is rotated so that slit covers both D's, a double peaked spectrum is observed. The double peaked spectrum, the solar spectrum near 6302, and the profile of the blocking filter, are shown in Figure 3.

In the magnetograph, one D is in the p beam and the other is in the s beam. When the etalon is at the proper temperature, the p beam channel passes light in a 90 mÅ band centered +85 mÅ from the iron line at 6302.5, while the s beam passes light in a 90 mÅ band centered at -85 mÅ from 6302.5. These are referred to as the red and blue channels, respectively.

8. Fabry Lenses. The Fabry lenses focus the essentially collimated beams from the Fabry-Perot onto the detectors.

9. Detector. The diagram shows a pair of PIN diode detectors. The actual experiments described below used photomultipliers in these positions.

2.2 Principles of Operation

2.2.1 Signal States

From the above description, the magnetograph optical layout produces a pair of beams centered at plus and minus 85 mÅ from line center. Control of the waveplate allows analysis for RCP in $+\Delta\lambda$ and LCP in $(-\Delta\lambda)$: State I; or analysis of LCP in $+\Delta\lambda$ and LCP in $-\Delta\lambda$: State II, or p polarized in $+\Delta\lambda$ and s polarized light in $-\Delta\lambda$: State III, or s polarized light in $+\Delta\lambda$ and p polarized light in $-\Delta\lambda$: State IV.

Table 1

State	Waveplate	Red Band	Blue Band
		$+\Delta\lambda$	$-\Delta\lambda$
I	$+\lambda/4$	RCP	LCP
II	$-\lambda/4$	LCP	RCP
III	Off	P	S
IV	$\lambda/2$	S	P

By proper addition and subtraction of the photo signal in both channels in the various states, sufficient information for longitudinal magnetic and velocity field can be collected. For example, switching between States I and II yields in both the plus and minus channels a magnetogram signal. Because the States I and II send opposite circular polarization into opposite sides of the line, the signals in both wavelengths are in phase. For a pure magnetograph a single detector would suffice which could collect light from either or both the plus and minus delta lambda channels.

States III and IV can be used for velocity measurements. If the input light is unpolarized, no transverse field, half the light goes to each of the wavelength samples. Thus, an inbalance in the channels measures velocity. The use of the system states is described in some detail in Sections 2.4 and 5.1 of Mosher's report.

2.2.2 The Temperature-Velocity Problem

2.2.2.1 Earth Operation

The magnetograph was designed specifically to minimize the temperature-velocity problem. Operated on Earth the solution is nearly optimal. Key to the design is the use of an etalon with two bandpasses on a single substrate. Because of this, whatever the tilt of the etalon or its temperature the pair of peaks maintain their separation in wavelength. A null velocity signal can be obtained without knowledge of either the absolute temperature or tilt of the etalon by balancing the signal that arrives in the plus and minus delta lambda channels. Unfocussed sunlight provides a null or nearly null velocity source. The capability of switching from State III to State IV allows calibration for internal polarization.

The bandpass channels span (-130 mÅ, -40 mÅ) and (+40 mÅ, +130 mÅ). Because the solar rotation rate is 2 km/sec, one limb has a relative velocity with respect to the other of 4 km/sec which, at λ6302 Å, corresponds to a relative wavelength shift of 84 mÅ. Therefore, it is necessary to shift the position of the etalon angle only once to cover east and west halves of the solar image.

The wavelength to temperature sensitivity of the etalon is .0468 Å/°C or 21.4°C/Å. The velocity sensitivity to wavelength is 2.1 x 10^{-5}Å/meter/sec. Therefore, the temperature sensitivity to wavelength is 4.5 x 10^{-4}C°/m/sec. To detect a velocity of 5 meters per second requires temperature stability or temperature knowledge of .0022°C. For a resistance thermometer at 30°C the resistance change per degree is 160 Ω/°C. To measure 5 meters/sec, we must detect a change in resistance of .377 ohms on a basic resistance of the sensor of 4000 ohms. Thus, the measurement accuracy required is on part in 10^4. This is straightforward and can be done with off-the-shelf 4 1/2 digit multimeters.

It should be emphasized that it is not necessary to stabilize the temperature to 10^{-3} degree accuracy. It is only required that the temperature be monitored. This has been done in the laboratory using a 4 1/2 digit multimeter attached to resistance thermometers in the etalon cell. The temperature variation observed varied slowly and could be easily compensated for by the meter itself.

The digital multimeter used was a Fluke 8800 calculating multimeter. This device can store a program and display and output a digital signal based upon the calculations. Using the temperature resistance tables and the etalon properties, the meter was programmed to read out resistance, temperature, wavelength, and velocity offset. One could observe that in the 5 m/sec range the velocity did not vary rapidly in time.

As discussed in the Mosher report, the temperature is not a problem for the magnetic measurements. A temperature stability of .1°C causes wavelength stability of less than 5 mA which has virtually zero effect.

2.2.2.2 Spacecraft Operation

The principal problem of operation on a spacecraft is the potential for high line-of-sight velocity. A circular near-Earth orbit implies a tangential velocity of 7.5 km/sec. Depending on the inclination of the orbit to the ecliptic and the azimuth with respect to the Earth-sun line, the relative velocity from sunrise to sunset can be as large as 15 km/sec. Fifteen kilometers per second causes wavelength shift of 315 mÅ which can be compensated by an etalon tilt of 0.810 degrees. This large tilt causes considerable concern about the effective FWHM of the etalon. For perfectly collimated light, the change in FWHM is negligible for the tilt angles of interest. However, the finite size of the field stop results in imperfect collimation by the field lens. The shift in wavelength with angle for a Fabry-Perot is

$$\frac{\Delta\lambda}{\lambda} = - \frac{\theta^2}{2n^2}$$

and the effective width with a beam of angular width δ is

$$\mathrm{FWHM}(\delta) = \left((\mathrm{FWHM})^2 + \mathrm{SPREAD}(\delta)^2\right)^{1/2}$$

If we accept a 25 percent broadening of the FWHM, then the tolerance for Spread(δ) is 50 mÅ. To a good approximation

$$\text{Spread}(\delta) = \frac{(\delta^2 + 4\theta\delta)}{2n^2}\,\lambda$$

where δ is the width of the quasi-collimated beam and θ is the tilt angle. At normal incidence, the allowed δ is

$$\delta = \left[\frac{2n^2(.05)}{6302}\right]$$

or

$$\delta = .0056 \text{ radians.}$$

For a 25 mm focal length collimating field lens this implies an aperture diameter

$$A = (.0056)(2)(25 \times 10^3)$$

or

$$A = 281 \text{ microns.}$$

Now, for the 15 km/sec case (θ = .01414 radians), the value of δ for a 50 mÅ beam spread is

$$\delta = \frac{(.05)n^2}{6302(4)(.01414)}$$

or

$$\delta = 5.6 \times 10^{-4} \text{ radians.}$$

This drops the acceptable maximum aperture size to about 28 microns.

The size of the aperture can be increased by increasing the focal length of the collimating lens. Therefore, one effect of the high tilt is the range in aperture size because it is not practical to use apertures much smaller than 5 microns.

A much more serious problem is that the etalon must be constantly tilted throughout the orbit to center the magnetograph. The price of this is mechanical complexity and perhaps velocity accuracy. The accuracy problem may be solved by precision optical encoders on the tilt axis.

2.3 Modulators

The primary modulators used in ground based magnetographs are KDP plates, Kerr cells, and quartz acoustic modulators. The number of types used reflects the fact that none of the modulators are entirely satisfactory. Both KDP plates and Kerr cells require several thousand volts for $\lambda/2$ wave retardation. The Kerr cells suffer the additional disadvantage that they are liquid filled, while KDP plates are notorious for being ultra sensitive to thermal and mechanical shocks. The quartz modulators operate by mechanical deformation of the crystal which induces strain birefringence. Unfortunately they operate in a mechanical resonant mode at about 50 kHz. This is rather higher than is desirable in a simple signal chain. However, the quartz modulators could be successfully used.

In the compact magnetograph we have chosen to use a PLZT modulator manufactured by Motorola. These devices require about 200 volts for a half wave at λ6302. They have the disadvantage that the electrodes are in the aperture. The electrode coverage is about 2 percent, so that in our collimated mode, we suffer a 2 percent light loss. The devices were developed as the active component of fast shutters in atomic blast goggles. In their intended application, they are placed between crossed polarizers and are biased to $\lambda/2$ in the mid visible.

The intended application of the PLZT materials requires that they meet severe military specifications for ruggedness, reliability, and uniformity. The samples we have tested are quite uniform. They have proved satisfactory and should be easily space qualified. Because of their ruggedness and proven reliability, we have decided to include them in the compact magnetograph.

2.4 Filters

2.4.1 Blocking Filters

When the compact magnetograph was originally proposed the best all-deposited filters had FWHM's of 6 to 8 Å. These filters were of the three-cavity design and had transmissions between 40 to 60 percent when blocked for the UV and IR. The width of these filters, combined with the finesse of 15 to 20 for solid etalons required a tandem etalon design.

Discussions with Spectrofilms in Andover, Massachusetts, indicated it might be possible to construct all-deposited filters with FWHM's less than 2 Å. Two such filters were manufactured, one with a FWHM of 1.3 Å and the other of 1.6 Å. Both filters are two-cavity designs, are fully blocked, and have 25 percent transmission. These filters allow going to a single solid etalon rather than the dual etalons previously required. This is an immense simplification in the system. To compensate for spacecraft velocity would otherwise require control of a pair of etalons.

With new coating control techniques, which should be possible with a dye laser monitoring system on the coating chamber, it is reasonable to hope that 1 Å filters with greater than 50 percent transmission can be made.

2.4.2 Novel Etalon

The novel etalon has been discussed above, but it is worth discussing of the manufacturing technique. First, it must be noted that before the 1.3 Å blocker was available the split etalon could not be considered. A system of two split etalons would be too complex.

The split etalon was manufactured from an existing 90 mÅ bandpass solid Fabry-Perot. The device was a freestanding wafer of fused silica about 1 mm thick. The etalon was returned to Perkin-Elmer and stripped of its dielectric mirrors. The cleaned substrate was then coated with SiO_2 and the rate of deposition, monitored. Once the rate was known, a mask was inserted over half the etalon. After a time such that 190 Å of material was deposited, the source shutter was closed. This process resulted in an etalon whose halves had slightly different thicknesses and hence offset spectral channels. The design objective was that the channel spectra were separated by twice the FWHM. Because the etalons are on the same substrate they will always be subject to the same conditions, in particular, temperature and tilt.

The technique of preferentially coating a desired thickness variation on an etalon is, we think, a significant advance.

2.5 Operations

The initial plan was to operate the compact magnetograph with a pair of PIN diodes and synchronously detecting in phase with the quartz acoustic modulator. The electronics built for this task simply did not perform as expected. We feel that there is nothing fundamentally wrong with the design or the diodes; however, time and the funds available under this contract did not allow development of the high-frequency amplifier chain.

The second electronics chain was based upon a photomultiplier, a lock-in amplifier, and PLZT plate. The operating frequency was 30 Hz. From the Mosher report, about 10^8 photons per second per 10-arcsecond region were received. Only one signal channel was used, plus delta lambda. The scans were made by allowing the solar image to drift across the aperture with the drive off. Because there was no velocity compensation, the magnetic sensitivity decreased across the disk as the effective location of the plus delta lambda channel with respect to line center decreased. In addition, because of the operation in the spectrograph room, the solar beam reflected off a heliostat and two folding flats.

Shown in Figure 4 are a series of scans across the solar image. The basic triangular shape is due to the residual circular polarization introduced by the non-normal reflection from the mirrors and the reduction of sensitivity as the wavelength channel moves toward line center. However, in the neighborhood of a sunspot, a magnetic field is clearly detected.

3.0 Future Activities

At the completion of this contract a great deal remains to be done to have a working magnetograph. A raster scan control program must be developed and the electronics chain must be improved as the minimum first step. Then some sophisticated software needs to be developed to establish the ultimate accuracies obtainable for the measurement of velocities.

Hopefully funds will be found to place a compact magnetograph in operation. However, this program has demonstrated that a compact magnetograph is feasible.

Figure Captions

Figure 1. Optical layout of compact magnetograph.

Figure 2. Photograph of magnetograph on echelle spectrograph.

Figure 3. Solar spectrum in the neighborhood of λ6302.5 together with spectral traces of both channels of the Fabry-Perot and 1.3 Å blocker. All figures are to the same wavelength scale.

Figure 4. Drift scans across the solar image. Region of sunspot marked by dots. Magnetic signal region underlined.

ORIGINAL PAGE IS
OF POOR QUALITY

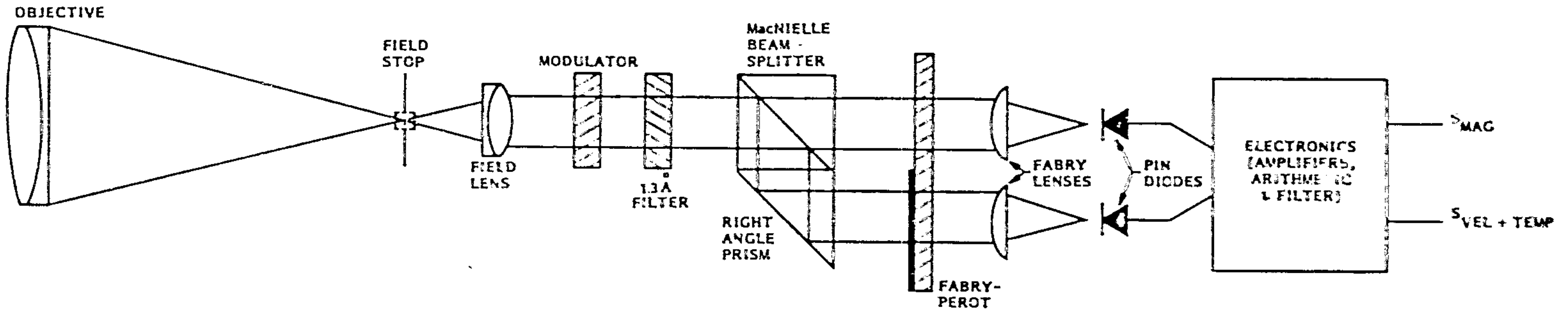

COMPACT MAGNETOGRAPH PROTOTYPE

ORIGINAL PAGE
BLACK AND WHITE PHOTOGRAPH

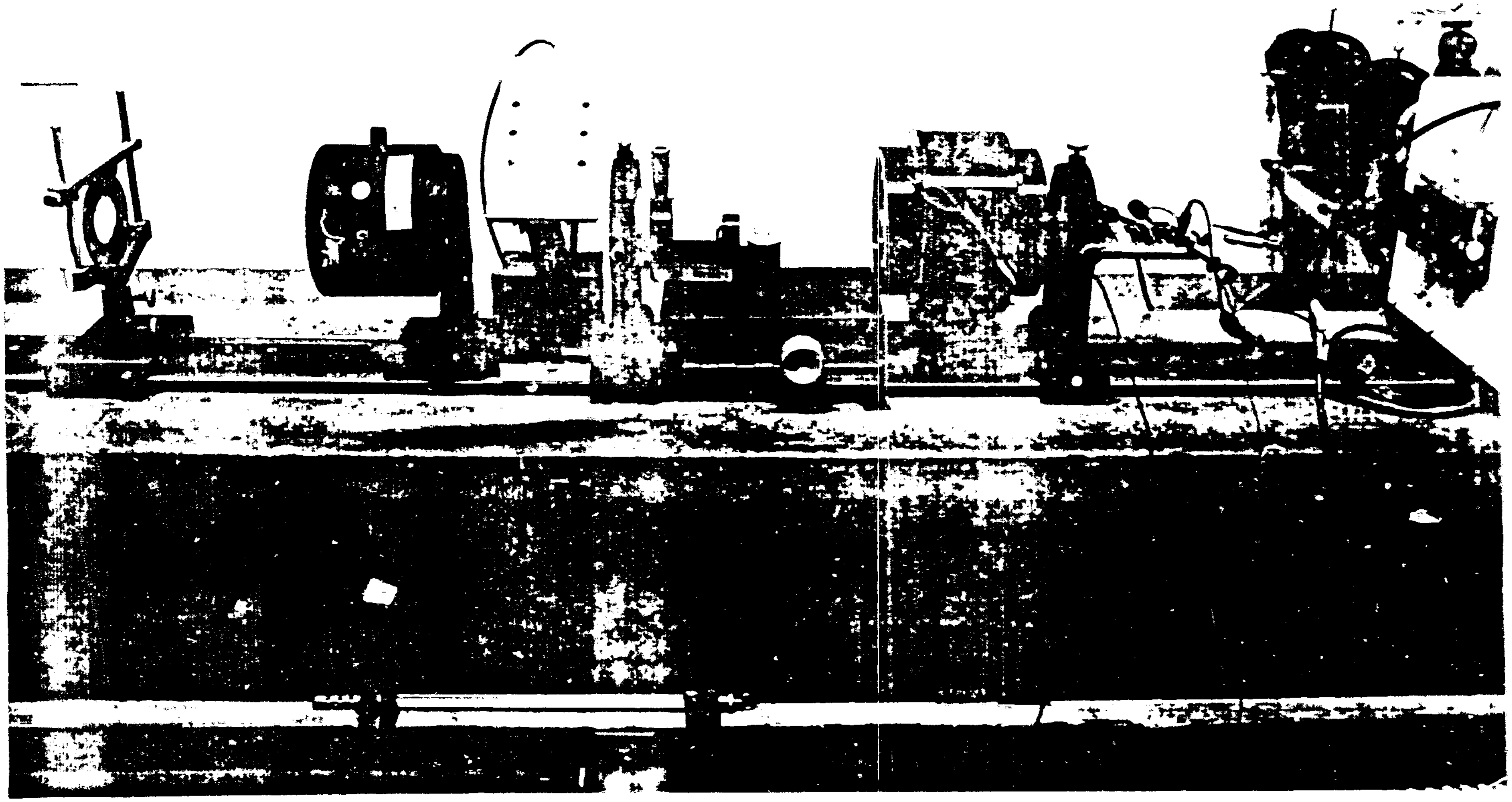

FIGURE 2

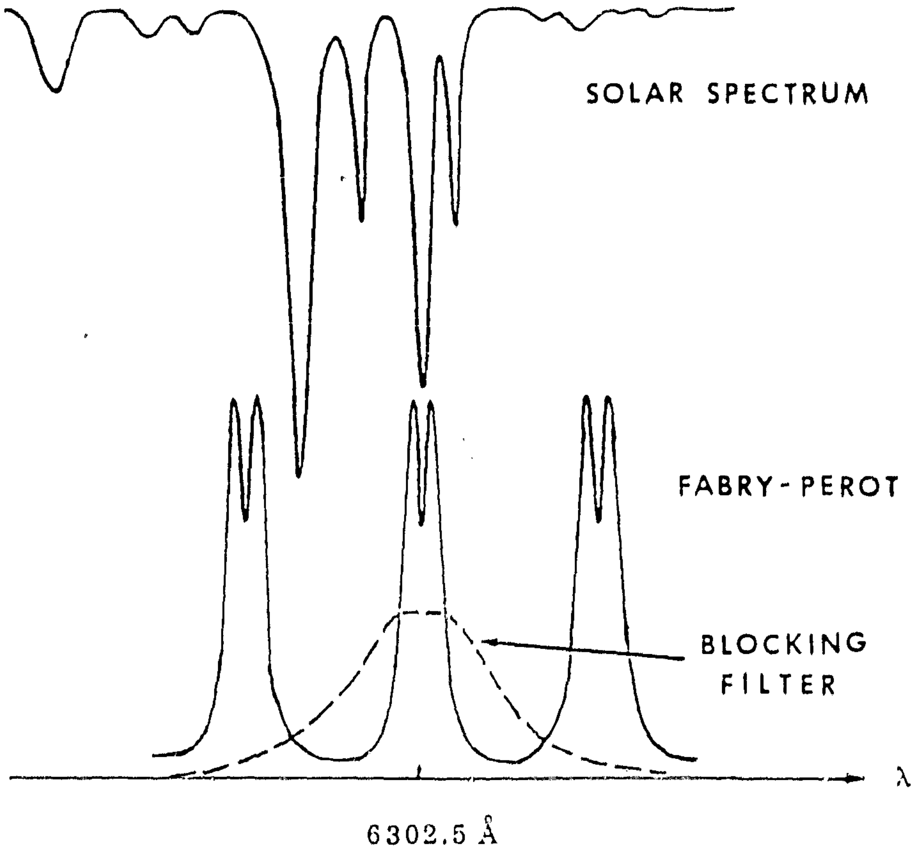

Figure 3

SOME THOUGHTS ON THE DESIGN OF A COMPACT MAGNETOGRAPH USING FABRY PEROT FILTERS

December, 1980

TABLE OF CONTENTS

2. Basic Design

    2.3 Corrections Needed for Large Sampling Apertures

3. Calculation of Expected Magnetic Signal and Ideal Integration Times

    3.1 Approximate Determination of the Physical Conditions Corresponding to the Lower Mount Wilson Contours

    3.4 Detailed Calculation of the Magnetic Signal and Integration Time for a Perfect Detector

    3.5 Optimization of the Magnetic Signal

4. Operational Considerations

4.2 Selection of a Suitable Detector

4.3 Calibration of the Detector

5. Suggested Designs

5.4 Clarification of the Designs

LIST OF TABLES

CONSIDERATIONS IN THE DESIGN OF A
COMPACT MAGNETOGRAPH EMPLOYING FABRY-PEROT FILTERS

1. Objectives

The purpose of the proposed program is to demonstrate the feasibility of measuring solar magnetic and velocity fields by means of a compact system using Fabry Perot filters. The immediate goal is to construct a prototype system capable of producing a Mount Wilson-like raster scan of longitudinal magnetic fields with a sampling aperture of 10-20 arc seconds and negligible noise at the "5 gauss" level. A two-inch entrance aperture is desired, but a larger one may be used to compensate for the inefficiency of the available detectors.

2. Basic Design

2.1 Schematic Layout

For small sampling apertures, a very simple design is possible:

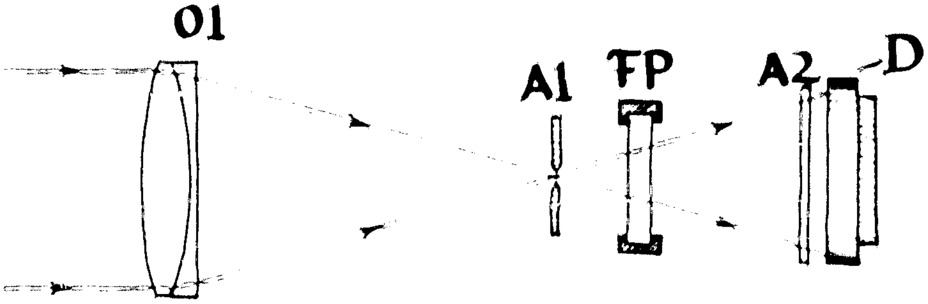

Figure 2.1: Optical elements of a compact magnetograph (horizontal scale highly compressed).

A1 is the 10 arc second field stop placed at the prime focus of the objective lens O1. FP is the Fabry Perot filter, A2 is a cemented quarter waveplate and polarizing mask (see Figure 2.4a), while D is the detector (currently assumed to be a 244 x 248 element CID array with a faceplate measuring 9 x 11 mm Figure 4.2.2a). The only elements not shown are the blocking filters, which would presumably be placed between the field stop and the Fabry Perot.

As long as the aperture A1 is small compared to both the objective diameter and the diameter of the "image" on the detector, the positions of FP, A2, and D after the field stop are arbitrary, permitting a free manipulation of the amount of filter and detector used by the light path. In fact, the polarization mask A2 can be placed anywhere in the system, even in front of the objective. None of the indicated parts are intended to move, except for purposes of alignment. Different points on the sun are examined by changing the pointing of the entire assembly, and the filters are tuned by temperature, rather than tilting.

2.2 Properties of Fabry-Perot Filters

According to McLeod's book (Thin Film Optical Filters), the transmission coefficient through a single element Fabry Perot filter is given by:

$$T(\lambda) = \frac{T_0}{1 + \frac{4F^2}{\pi^2} \sin^2 \left[\frac{2\pi n_s d_s \cos \theta_s}{\lambda} \right]} \qquad (2.2a)$$

where T_0 is the peak transmission coefficient (determined by absorptive losses in the mirror coatings and substrate), and the "finesse", F, is an empirical coefficient related to the reflectivity, R_s, of the partially tranparent mirrors. For ideal, plane parallel mirrors:

$$F = \frac{\pi \sqrt{R_s}}{(1-R_s)} \qquad (2.2b)$$

n_s and d_s are the index of refraction and thickness of the substrate material between the mirrors, and θ_s is the angle of the light path (inside the substrate) relative to the normal direction.

Mathematically, for moderate or large values of F, this equation describes a series of sharp, widely-spaced peaks. The peak wavelengths, $\lambda_0(k)$, are determined by the condition that the sine-term should vanish:

$$\lambda_0(k) = \frac{2n_s\, d_s \cos \theta_s}{k}, \quad k = 1,2,3,..... \qquad (2.2c)$$

If the general equation is expanded about one of these points, a somewhat more useful approximate form can be obtained for the transmission coefficient:

$$T(\lambda) \simeq \frac{T_0}{1 + \frac{4F^2}{\pi^2} \sin^2 \left[\frac{\pi(\lambda-\lambda_0)}{\mathrm{FWHM}} \right]} \simeq \frac{T_0}{1 + \left[\frac{2(\lambda-\lambda_0)}{\mathrm{FWHM}} \right]^2} \qquad (2.2d)$$

where

$$\mathrm{FWHM} = \frac{\lambda_0^{\,2}}{2n_s\, d_s \cos \theta_s\, F} \qquad (2.2e)$$

is the full width of the transmission peak at half-maximum.

Using this notation, the spacing between successive peaks can be written as:

$$\text{spacing} = F * \text{FWHM} \qquad (2.2f)$$

Also, the extinction ratio is:

$$T_{max}/T_{min} = 1 + \frac{4F^2}{\pi^2} \qquad (2.2g)$$

For the present purposes, one of the most important aspects of the Fabry Perot equation is the dependence of the transmission profile on angle. It is evident that the primary effect will be a shift in the wavelengths of the transmission peaks. This shift is determined by the condition that the argument of the sine term must be kept equal to kπ. In approximate form this requires:

$$\lambda_0(\theta) = \lambda_0(\theta=0) * \left[1 - \frac{\theta_i^2}{2n_s^2}\right] \qquad (2.2h)$$

where θ_i is the external angle of incidence (i.e., measured outside the substrate) and n_s is the index of refraction of the substrate.

For the design indicated in the first figure, it is evident that each radial position in the detector plane corresponds to a different angle through the filter and therefore to a different wavelength of peak transmission. The maximum angle is simply related to the f-number of the beam through the filter, which, in absence of vignetting and diffraction, would be the same as the f-number of the objective lens, i.e.:

$$\theta_{max}\ (\text{radians}) = 0.5/\text{f-number} = 0.5*\text{f-ratio} \qquad (2.2i)$$

Given this radial dependence of wavelength the "image" on the detector plane is expected to look like:

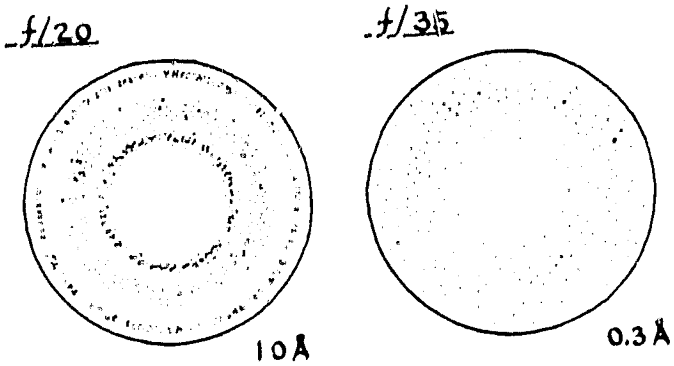

Figure 2.2.a. Intensity pattern expected on detector plane with different f-numbers. The shaded portions represent the solar line absorption.

where it has been assumed that the FeI absorption line at 6302.6Å is being observed. This line has a total width of about 0.3Å, which is just covered at f/30. At f/20, the range of wavelength coverage is increased to where the neighboring telluric lines can be seen. The outer one is to the red, and the inner one to the blue. The nature of the spectral dispersion produced by the Fabry Perot operating in this mode is such that an equal area of the detector is available for each fixed increment (e.g., 0.1Å) of wavelength.

Not only does each point in the image correspond to a specific wavelength of peak transmission, but by the same ray tracing argument, it originates from a specific point on the objective lens. That is, the rays forming the outer edge of the detector plane image originate from the outer edge of the objective, those ending in the center began in the center, and so on. It is as if, in other words, a suitably scaled image of the detector plane were marked on each element along the optical path (in particular, the objective lens, the filter, and the polarizing mask). A consequence is that radial non-uniformities or splotchiness in these elements cannot easily be distinguished from genuine spectral information.

In order to maintain the equal area condition, a "properly" centered spectral line should appear with its absorption core $1/\sqrt{2}$ of the way from center to edge of the detection field. Under such circumstances, the principal transmitted wavelength at any point in the detector plane is given by:

$$\lambda(r) = \lambda_o - r^2 \Delta\lambda_{max} \qquad (2.2j)$$

where λ_o is the wavelength of the line core, r is the radial position (normalized to 1 at the edge of the field), and:

$$\Delta\lambda_{max} = \frac{1}{2} \lambda_o \left(1 - \frac{\theta^2_{max}}{2\, n^2_s}\right) \qquad (2.2k)$$

(c.f. equation 2.2i).

This ideal configuration can be disrupted by drifts in filter temperature (which move the bandpass red-ward by approximately .036Å/°C due to the expansion of the substrate), and by errors in the mounting of the filter (if the

(and $\frac{\partial n}{\partial T}$)

angles are comparable to those in the cone of light):

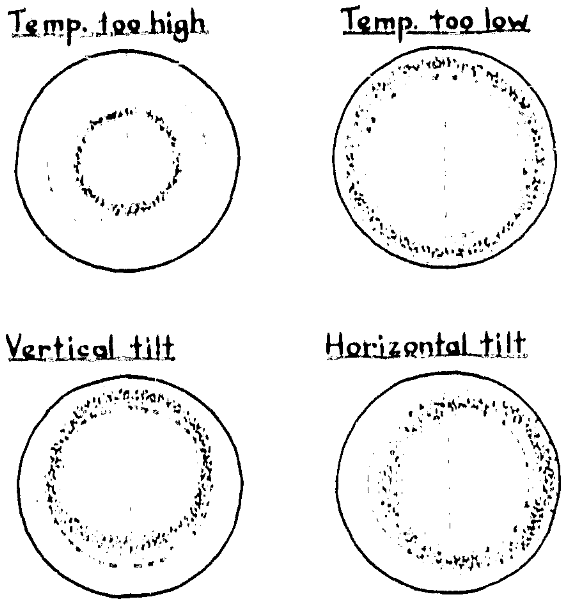

Figure 2.2b: Aberrations expected in the image plane for temperature and mounting errors. The dashed lines represent the boundaries of the detection zones (cf. Figure 2.4a). The temperature-associated changes could equally well be induced by line-of-sight velocities.

In the absence of the telluric lines as a reference, the "temperature too high" case cannot, incidentally, be distinguished from a motion of the solar absorbing material away from the observer, nor the "temperature too low" case from a motion towards the observer.

2.3 Corrections Needed for Large Sampling Apertures

2.3.1 Telecentric Corrector Lens

If very large sampling areas are to be used, additional precautions have to be incorporated into the design. These consist of the introduction of a telecentric corrector lens in front of the field stop, and of an objective-imaging field lens between the filter and the detector. The first modification becomes necessary if the size of A1 is comparable to the diameter of O1:

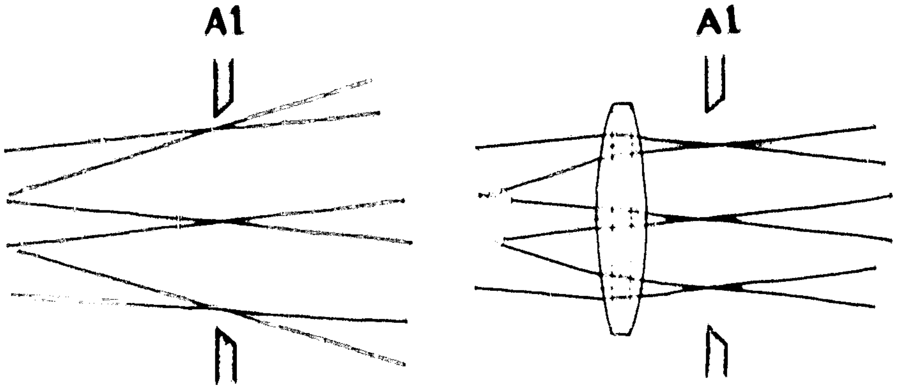

Figure 2.3.1: Function of telecentric corrector lens (highly exaggerated). The lens is placed immediately before the field stop. Left side = before correction. Right side = after correction.

The telecentric corrector is a lens whose focal length is equal to its distance from the objective lens. Without it, the cones of light forming the outer portions of the solar image (at prime focus) would have a slight systematic tilt relative to those forming the center. This tilt would be translated into a wavelength bias as the light passes through the Fabry Perot filter.

If R is the radius of the objective (01), r the radius of the field stop (A1), and ℓ their separation (which is equal to the focal length of 01), then the basic half angle of the cones forming the image is:

$$\theta_{cone} = R/\ell \text{ (radians)} \tag{2.3.1a}$$

(which determines the maximum wavelength range accessible to the detector if the full cone is utilized). Since the central rays of all of the cones originate at the center of 01, the maximum systematic tilt imposed by the finite size of A1 is:

$$\theta_{tilt} = r/\ell \text{ (radians)} \tag{2.3.1b}$$

and wavelength bias is roughly:

$$\delta\lambda = -\frac{\theta tilt^2}{2n_s^2}\lambda_o \tag{2.3.1c}$$

In general, this will be found to be very small. For example, for a 2" (5 cm) f/35 objective one would have ℓ = 175 cm, and a 10 arc sec (diameter) field stop would have r = .004 cm. This would give a systematic bias of only about 8×10^{-7} Å at λ6302.

Even if the wavelength bias were larger, it would not necessarily be serious. It means that at the detector, the line will not be equally well "centered" for all possible positions in the sampling aperture. For longitudinal field measurements, this affects only the sensitivity (slightly) and not at all the zero. For Doppler measurements at a fixed solar position, it would mean that there would be a slight apparent blue shift as the size of the aperture A1 was increased.

2.3.2 Lens to Reimage Objective

The second modification, the lens to re-image the objective after the light passes through the filter becomes necessary if the size of the field stop A1 is to be comparable to that of the detector, D, which would be placed approximately at the focal point of this new lens:

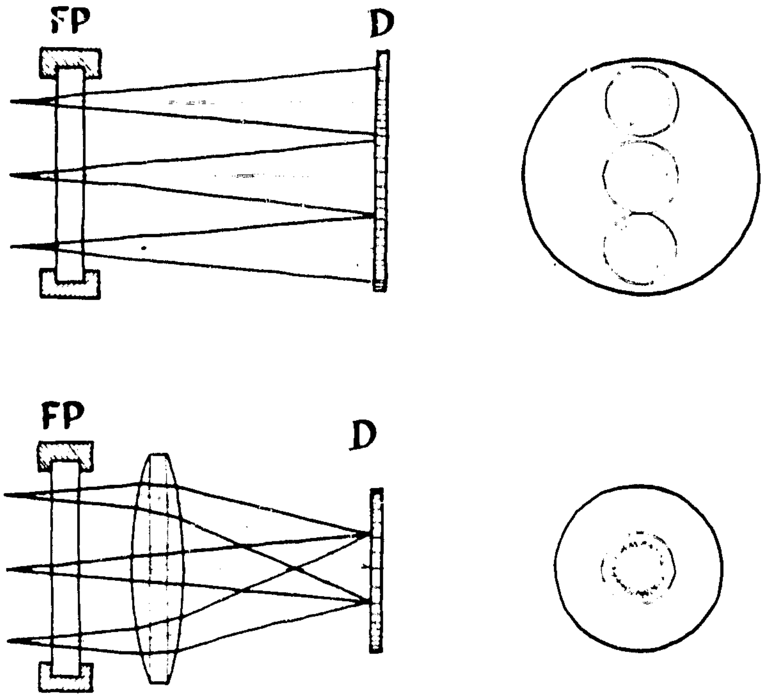

Figure 2.3.2: Function of the objective re-imaging lens (highly exaggerated). The lens is placed between the filter and the detector. Upper = without correction. Lower = with correction. The views on the right show the intensity pattern falling on the detector.

As indicated, in the absence of the field lens, the Fabry Perot spectral ring patterns generated by cones originating at different points within A1 would be misregistered on the detector. For a telecentric system, this lateral misregistration is exactly equal in magnitude to the lateral dispersion in their sources at A1. Thus, the maximum misregistration is equal to r, the radius of A1. The amount of misregistration which can be tolerated depends on the amount of spectral resolution which is to be achieved in the detector plane. For normal magnetic measurements, only a rather coarse segregation of wavelengths is required, and it would certainly be more than sufficient if the various cones were registered to within, say, one-tenth of the detector radius (which is assumed to be equal to the radius of any one of the cones). If the distance from A1 to D is ℓ', then this radius will be $R' = \ell' R/\ell$; and the condition $r < 0.1R'$ is therefore equivalent to $\ell' > 10r\,\ell/R$. For the 2" f/35 objective with $r = .004$ cm, the auxilliary field lens would be unnecessary if $\ell' > 3$ cm, that is, if $R' > 0.4$ mm.

While these two additional lenses add a certain theoretical niceness to the design, they should be avoided if possible. Not only will their absence improve the optical transmission of the system, but it will minimize the possibility of dirt, optical imperfections, and secondary reflections interfering with the interpretation of the spectral patterns.

2.4 Extraction of Magnetic and Temperature Signals

The optical design described above provides a simple mechanism for dispersing the incident sunlight into its constituent wavelength components. Given this dispersion, the presence of longitudinal solar magnetic fields can be detected by searching for a net circular polarization in the wings of a magnetically-sensitive solar absorption line.

In most successful photoelectric designs of the past this has been accomplished by using the combination of a modulated electro-optic crystal and fixed linear polaroid to act as a valve admitting alternately the two circular polarizations at a fixed wavelength or bandpass in one line wing. If a flickering intensity is discovered, the presence of a field is inferred. The photon statistics, which dictate the time required to measure this modulation to a desired degree of accuracy can generally be improved by broadening the bandpass so as admit a considerable portion of the line wing about the point of maximum modulation. The light level can be further increased with no sacrifice in modulation by substituting a polarizing beam splitter for the single polaroid, so that instead of discarding half the light, the two wings can be sampled simultaneously (the right-handed component being passed in one wing and the left-handed component in the other) and the results combined with suitable phasing. In principle, although this has evidently not been tried in practice, it is also possible by means of a sufficiently complicated exit slit arrangement to photometrically combine the results from several lines (for earth-based observations, as pointed out by Livingston (Aph. J. 153, 929, 1968), such a scheme is limited by the differential refraction of the earth's atmosphere if high spatial resolution is being contemplated).

The Fabry Perot magnetograph deviates from this accepted design in that no modulating element is contemplated (although one could be incorporated, as indicated in section 4.8). Rather, the light originating at a specific point in the wing of the line is to be geometrically subdivided into two equal portions which are to be monitored by separate detectors, one for right-handed and the other for left-handed photons. Once the zero level has been determined, additional imbalances between the two detectors which arise as the system is scanned across the sun will be interpreted as evidence for the presence of fields of the appropriate sign and strength. The avoidance of systematic biases unrelated to the presence of fields obviously requires careful craftsmanship in the design and operation of instrument, the challenge being rather comparable to that involved in attempting to obtain acceptable magnetic cancellations by means of the "dual" exit slit spectroheliographic cancellation technique of Leighton and the Aerospace Corporation.

Another important design consideration is that of keeping the bandpass of the Fabry Perot filter properly centered on the wing of the line, so that adequate sensitivity and a stable calibration can be maintained. At present, it is felt that in order to achieve this objective it will be necessary to be able to monitor the position of the line core in real time, which means that the detector will have to have both wings of the line accessible to it (by use of suitably small f-number). This "small" f-number (small meaning a divergent/convergent beam) is not particularly desirable for magnetic measurements, for recalling that the detector plane geometry is effectively painted on the objective lens a smaller and smaller portion of the incident sunlight is being used for the magnetic measurement as the range of wavelength coverage is increased. However, if it is dictated by the requirements of temperature control, then it is certainly desireable to make the best of a bad situation by performing the magnetic sampling in such a way that both wings of the line can be used, rather than ignoring one wing completely. The simplest magnetic/temperature sampling scheme involves four detector elements, and can be indicated schematically as follows:

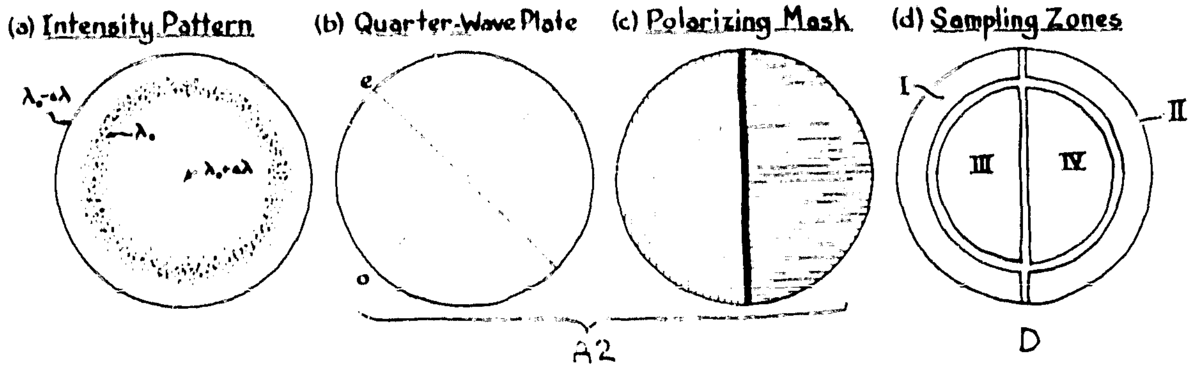

Figure 2.4a: A simple 4 sector scheme for sampling the magnetic and temperature (velocity) signals. The polaroid configuration shown here is later referred to as "Mask I".

The incident intensity pattern, centered on a spectral line, is passed first through a fixed quarter wave plate, and then through a polaroid mask consisting of two orthogonal linear polaroids whose axes are at 45° to those of the quarter wave plate. One orientation of polaroid will pass right-hand circular photons, while the other will pass left-hand circular. Detector segments I(RHC) and II(LHC) are in the blue wing of the line, while III(RHC) and IV(LHC) are in the red wing. The magnetic signal is obtained by combining the polarization differences from the two wings (which can be thought of as independent samples, and should be of equal magnitude, but opposite in sign). The temperature signal is obtained by comparing the total intensities collected in the two wings.

$$\text{Magnetic signal} = \left((I_{I} - I_{II}) + (I_{IV} - I_{III}) \right)/I_{tot} \qquad (2.4a)$$

$$\text{Temperature signal} = \left((I_I + I_{II}) - (I_{III} + I_{IV}) \right)/I_{tot} \qquad (2.4b)$$

$$\text{where } I_{tot} = I_I + I_{II} + I_{III} + I_{IV} \qquad (2.4c)$$

These two signals are constructed in such a way as to be independent both of each other and of the overall intensity level. The division by I_{tot} is necessary to maintain the normalization (i.e., the "sensitivity") of the signals in the presence of varying light levels. The signals are coupled in the sense that the sensitivity of the magnetic signal will fall off if the temperature (or velocity) is such that the filter is very far off line center (cf. Section 4.4).

Note that a small part of the light around the core of the line is indicated as not being sampled by the detectors. This is intentional, because, as will become evident later, to include this weakly modulated light would slightly degrade the signal to noise. This exclusion can be accomplished either at the detector, or by including a suitable occulting ring in the polarization analyzing mask.

A slightly more complicated polarizing mask could also be used:

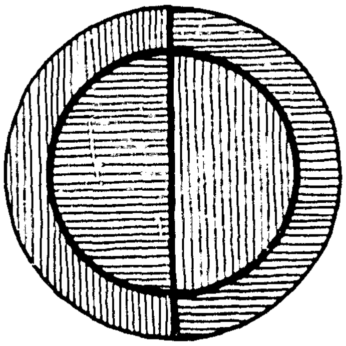

Figure 2.4b: "Mask II", an alternative polaroid configuration.

In this case, the magnetic signal would be derived from $(I_I - I_{II}) + (I_{III} - I_{IV})$. The motivation for considering this more complicated mask is explained in the following figure, where, the expected intensity patterns are shown (in exaggerated form) for (on the left) a situation in which the RHC absorption profile is shifted to the blue and the LHC profile to the red, and (on the right) for one in which the magnetic shifts are in the opposite direction. It is evident that if the simpler mask (I) is used, the expected patterns are similar to those which could be produced if the filter were accidentally tilted. More importantly, Mask II converts the magnetic blinking from an annular to a left-right pattern which permits a very simple two detector sensing system to be used (see Section 5.1).

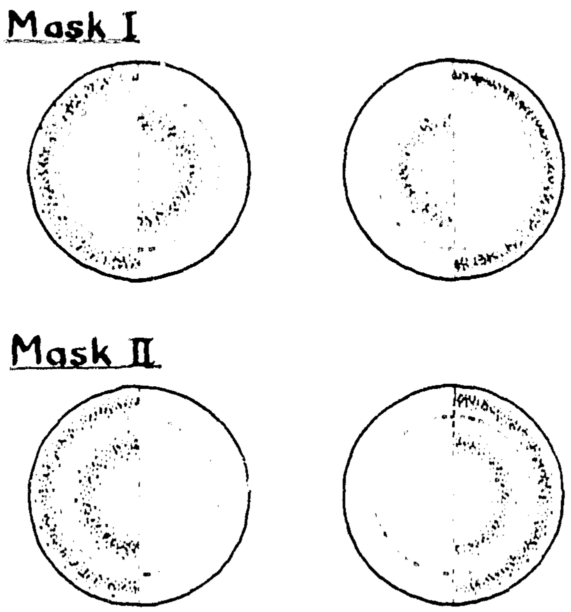

Figure 2.4c: Intensity patterns expected on the detector for a Zeeman-split line. Positive field (left), negative field (right).

Although it has been suggested that the dissection of the detector image into the required sectors will be accomplished by sorting the readout from a higher-resolution CID-type image plane readout, this is not an essential feature of the scheme. Indeed, if the number of sectors is kept small, one could imagine feeding the appropriate light, by means of prisms, to physically separate devices (for example photodiodes or photomultiplier tubes - see Section 4.2, and the specific designs in Section 5).

Under some circumstances, more detailed spectral information, that is, the ability to dissect the 'image" into finer wavelength rings, may be desireable. For example, if observations are made at high spatial resolution, the variation of polarization with wavelength in spectral line wings carries important information as to the nature of the fine scale fields. In particular, the point of maximum modulation is an indication of the true field strength (if it is greater than about 1000 gauss), and the magnitude of the signal is an indication of the amount of line weakening. Under the present circumstances, however, this would not seem to be a very serious consideration. Not only is the 2" aperture instrument inappropriate for high-resolution observations, but the field stop required for 1 arc second resolution would be objectionably small. With a diameter of only 0.8 microns, the field stop would begin to become the element determining (by diffraction) the angle of the cone passing through the filter. While this particular problem could be gotten around by adding extra lenses, the light level passed by the small aperture would be insufficient to permit the measurements to be made in a reasonable time compared to the lifetime of the magnetic elements.

If the spectral information is not to be used for such purposes, there is no persuasive reason to divide the basic sectors into finer wavelength rings.

3. Calculation of Expected Magnetic Signal and Ideal Integration Times

The practical feasibility of any solar magnetograph design hinges primarily on two factors: the expected light level and the strength of the expected magnetic signal. In general, the latter can be predicted only if one has a fairly accurate picture of the true solar fields, and of the behavior of the magnetically sensitive line to be used. In recent years, the difficulty of making such predictions has become increasingly apparent, the primary complications being (a) that with finite resolution the field cannot be regarded as being homogeneous, but rather is some not-very-well determined composite of small (possibly unresolved) areas of strong field, interspersed with much larger portions of undisturbed photosphere; and (b) that in the areas of strong field the line profile may be quite different from that normally measured in undisturbed areas (due, presumably to differences in temperature, ionization balance and mass motions).

3.1 Approximate Determination of the Physical Conditions Corresponding to the Lower Mount Wilson Contours

3.1.1 True vs. Apparent Strength of Weak Fields

It is generally appreciated that when the Mount Wilson magnetograph registers "5 gauss" or any other field strength, what is actually being registered is an average over its sampling aperture (currently about 12.6 arc sec). If the line profile is a function of the field strength, the weighting function in the average can be complicated.

In the simplest models, it is assumed that what is present is a mixture of an area with zero field, and an area with some moderate or large fixed field strength, and that the appearance of a spectrum of field strengths is created by a variation in the fraction of area occupied by that fixed strength field from point to point. In other words, the total intensity of light in the aperture can be represented as

$$I(\lambda) = (1-f)\cdot I_0(\lambda) + f\cdot I_m(\lambda, B_0) \qquad (3.1.1)$$

where $I_0(\lambda)$ is the normal line profile in the undisturbed photosphere, $I_m(\lambda, B_0)$ is the magnetically disturbed line profile characteristic of a spatially resolved area with the true field strength B_0, and f is the "fill factor", that is, the fraction of area occupied by the field B_0. (Actually, for longitudinal fields there are two magnetic profiles, one for the right-hand circular, and one for the left-hand circular component, which are shifted oppositely in wavelength from the undisturbed position).

Information as to the magnetic profiles is not yet in a definitive state. For most photospheric lines the magnetic profile can be assumed to be shallower than the undisturbed ones (except in sunspots, where the lines deepen) as evidenced by the fact that the network points tend to be brighter than their surroundings at most positions in the lines (e.g., Sheeley, Solar Phys., 1, 171, 1967); Schoolman and Ramsey, Solar Phys., 50, 25, 1976). To actually establish the profile $I_m (\lambda, B_0)$ appearing in the preceding equation by direct observation it would be necessary to obtain a tracing in a single circular polarization of the profile for an area on the solar surface which is spatially resolved and uniformly occupied by a purely longitudinal field. At present, it is not even known if such an observation is even theoretically possible.

3.1.2 Normal and Disturbed Profiles of λ5250

The best indirect observational evidence regarding the magnetically disturbed profile of a single Zeeman component of the λ5250 line (which is used by the Mount Wilson magnetograph) is supposedly that obtained by Harvey and Livingston (Solar Phys., 10, 283, 1969; Figure 3b), who studied the variation in sensitivity of a magnetograph using this line as a function of the exit slit position in the line wing. They inferred a moderate broadening of the line profile in the magnetic elements, and a very great loss in central depth. In fact, they indicate that in the core of the line, the magnetic elements would be three or more times as bright as their surroundings (as a result of line weakening and Zeeman splitting). This does not appear to be entirely consistent with other observations, and it seems possible that in their analysis they may have confused the effects of saturation with those of line weakening. A re-evaluation of their sensitivity curve in terms of an inherently strong field might lead to a much more modest estimate of change in the line profile.

Additional information on the profile of a single Zeeman component of 5250 is provided by Stenflo (Solar Phys., 42, 79, 1975). He shows a much more moderate loss in central intensity (70-100% brightening in the line core), but the origin of his profiles is unclear.

As to direct tracings of the 5250 profile in spatially resolved magnetically disturbed regions, the only results to have been published (Harvey and Livingston, 1969 Figure 2, and Chapman and Sheeley, Solar Phys., 51, 61, 1977, Figure 2) appear to have been made without polarizing optics, which severely limits their usefulness. Nonetheless, these two results, one obtained photoelectrically and the other photographically, are in very good agreement. For strong non-sunspot magnetic fields they show the unpolarized 5250 profile broadening from 75 to 100 mA FWHM (Harvey and Livingston) or 88 to 109 mA FWHM (Chapman and Sheeley). Both show the undisturbed central intensity as being 26% of the continuum. In the magnetic gap it rises to 48% (Harvey and Livingston) or 57% (Chapman and Sheeley). If one assumes that the intrinsic width of the line profile is the same in the magnetic and non-magnetic regions, then in both cases the broadening could be explained by a longitudinal magnetic field of about 600 gauss. Under such an interpretation the true loss in central intensity is less than it appears in the unpolarized profile, since part of the loss is due to the Zeeman splitting. The true central intensity for the individual Zeeman components would need to be 32% of continuum(for Harvey and Livingston) or 48% (for Chapman and Sheeley). This amounts to an increase in central brighrness of 23% in the former case and 48% in the latter (as compared to the undisturbed profiles of the same components).

The published profiles of 5250 are all of a nearly "Gaussian" form:

$$I = I_o\left[1 - D_o\, e^{-.693\, \left(\frac{2\Delta\lambda}{FWHM}\right)^{n}}\right] \qquad (3.1.2)$$

In this notation, the results for the various disturbed and undisturbed line profiles can be summarized as follows:

Table 3.1.2 5250 Line Profiles

	Case	D_ω	FWHM	n	Source
Normal:	-	.73	82	2.2	Kitt Peak Prelim. Atlas
	-	.65	105	2.0	Sac Peak Atlas
	a	.73	71	1.8	Harvey and Livingston (Fig. 3a)
	b	.72	83	2.5	Stenflo (Fig. 5)
	c	.74	88	2.0	Chapman and Sheeley (Fig. 2)
	d	.74	71	1.8	Harvey and Livingston (Fig. 2)
Disturbed:	a	.25	103	2.2	Harvey and Livingston (Fig. 3b)
	b	.53	77	2.4	Stenflo (Figure 5)
*	c	.52	88	2.0	Chapman and Sheeley (Fig. 2)
*	d	.68	71	1.8	Harvey and Livingston (Fig. 2)

In the last two cases (marked by *'s) the magnetically disturbed parameters have been guessed from the unpolarized profiles as explained above.

The two profiles derived from the figures of Harvey and Livingston (cases "a" and "d"), seem to represent the extremes of reasonable thought regarding the possible extent of line weakening in 5250.

3.1.3 Estimate of the Signal Strength Required to Register "5 Gauss"

Given these profiles, it is a fairly straightforward matter to calculate the anticipated response of the Mt. Wilson magnetograph. According to Howard and Stenflo (Solar Phys., 22, 402, 1972), the magnetograph operates at λ5250 in the fashion indicated schematically in the following figure:

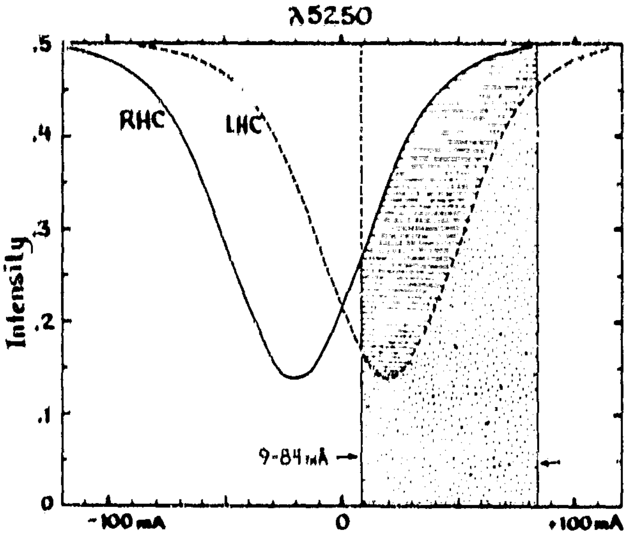

Figure 3.1.3: Sampling of magnetically-split line by the Mount Wilson magnetograph. The profiles shown are for a pure longitudinal field of 500 gauss with no line weakening. The difference signal is measured as the exit spectrum is modulated between the two circular polarizations.

that is, all of the light falling between 9 and 84 mA of the nominal line core is sampled sequentially in the right and left hand circular polarizations (actually, the two wings of the line are sampled independently, and the results combined to improve statistics). The signal is defined as:

$$S_{mag} = (I_{rhc} - I_{lhc})/(I_{rhc} + I_{lhc}) \qquad (3.1.3)$$

and converted into an equivalent field strength by comparison with a nominal calibration. The calibration, which is derived empirically, is the signal expected if the undisturbed profile is artificially displaced by an amount corresponding to the specified field strength. For a 5-gauss field (which shifts the line by ± .193 mA), using the various "normal" profiles given in the first part of Table II, calibration signals of (2.2 - 2.7) x 10^{-3} are anticipated. The average is 2.5 x 10^{-3}. It is not known if this is the actual empirical signal strength used as "5 gauss" at Mount Wilson, but it is probably close.

3.1.4 Combinations of Field Strength and Fill Factor Producing a 5 Gauss Signal

If the true intrinsic field strength, B_0, is anything greater than about 15 gauss it should be possible to find a "fill factor", f, which will reproduce exactly the nominal five-gauss signal. If we define $f \cdot B_0$ as the "true average" field stength in the aperture, then the following result is obtained:

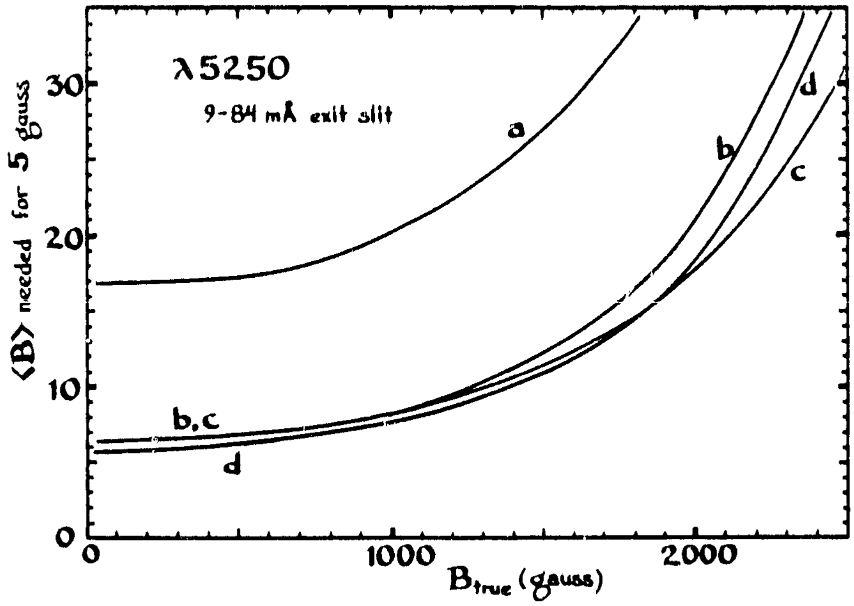

Figure 3.1.4: True average field strength ⟨ B ⟩ required to produce a signal of 5 gauss in the Mount Wilson magnetograph as a function of the intrinsic strength of the unresolved magnetic elements. The letters refer to the different possible assumptions about the shape of the magnetic and non-magnetic line profiles given in Table 3.1.2.

In all cases, the real average field strength has to be greater than 5 gauss to compensate for the line weakening. If the true field strength is very high, the average must be even higher to compensate for "saturation" as well - that is, the point of maximum signal is shifted out of the bandpass. The Harvey and Livingston result of case (a) seems to be far out of line with the other three, but it should be remembered that this is the one which most nearly purports to be a "direct" measurement of the magnetically disturbed profile (cf. § 3.1.2).

The figure suggests that average field strengths of 6-20 gauss are are likely to be encountered in the kind of features which produce "5-gauss" contours on the Mount Wilson magnetograms. The true field strength is not very well known, but it is probably around 1000 gauss. Very much smaller strengths can be ruled out by a comparison of the measured flux (which is a lower limit on the true flux), with the observed size of the features (which is an upper limit on the true size). Very much larger strengths can be ruled out by the absence of any obvious resolvable splitting in the high resolution unpolarized spectra.

3.1.5 Confirmation of Intrinsic Field Strength from Choice of Mount Wilson Exit Slit Positions

The idea that the intrinsic field strengths are less than or on the order of 1000 gauss also gains some support from the choice of exit slit positions which have been found historically to produce the best magnetograms in the least time. As pointed out above, as the field strength increases, the point of maximum modulation moves out in the wings, and the optimum integration time for a fixed signal to noise is obtained by using a bandpass "centered" on this peak signal, but incorporating a wide enough range to include all the useable light around it. (What is meant by "useable" is difficult to define in general, but it is easily determined in practice by moving the limits until the minimum integration time is found). The choice of optimum bandpass is, incidentally, very little affected by assumptions regarding fill factor.

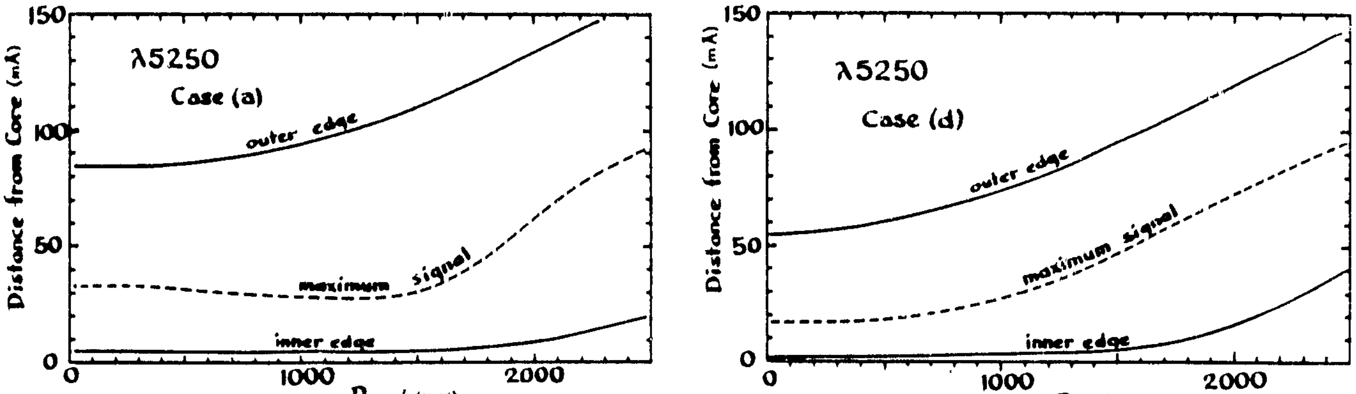

Figure 3.1.5a: Variation of point of maximum signal and optimum bandpass for different inherent strengths of the magnetic elements. The optimum bandpass is defined as that permitting the magnetic measurement to be made with fixed signal to noise in the minimum time. A small fill factor is assumed.

In the following figure, the integration time required to bring out the 5-gauss contour with a fixed signal to noise ratio using the Mount Wilson magnetograph's 9-84 mÅ bandpass is compared with that which would be required if the optimum bandpass were used.

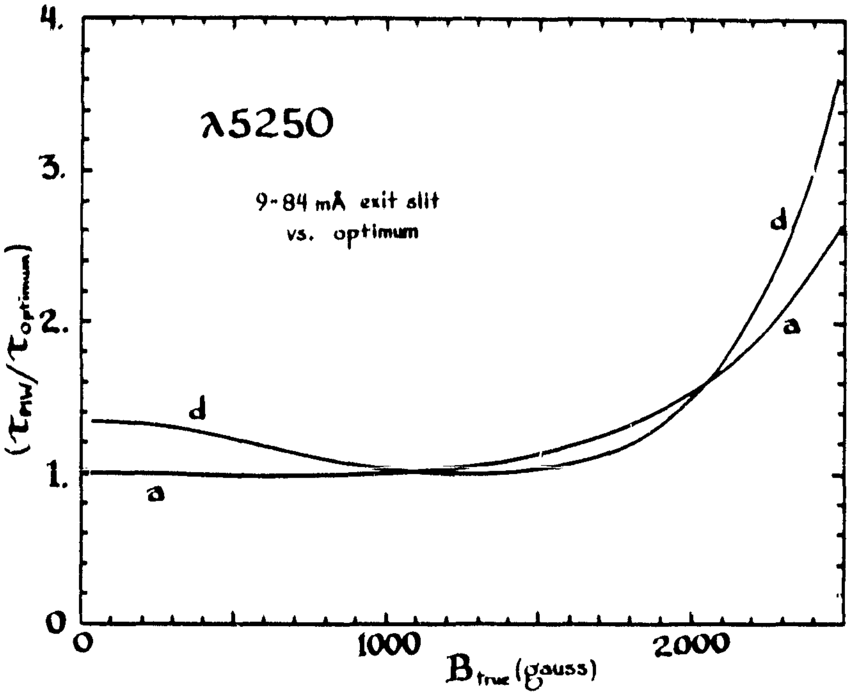

Figure 3.1.5b: Ratio of Mount Wilson integration time to that possible with optimum bandpass for various true field strengths and the two extreme assumptions regarding line profile changes. A small fill factor is assumed.

It is clear that regardless of the assumptions about line profile behavior, the magnetograph would be operating in a very inefficient mode if the true field strength responsible for the weak fields were much over 2000 gauss. A similar argument can be made for the Kitt Peak magnetograph, which, in its 40-channel form (Livingston, Ap.J., 153, 929, 1968) used a bandpass 40-70 mA in the 5250 wings. The motivation for this choice, which is never optimum, is unclear (probably an effort to obtain a "linear" response), but once again even greater inefficiency would be present if the true fields were over about 2 kilogauss.

3.2 Adoption of a Standard Weak Field Condition

Based on the results of the preceding section, the following combinations of inherent field strength and fill factor have been found to be consistent with the registration of a 5-gauss signal by the Mount Wilson magnetograph under the two extreme assumptions regarding the variation of the 5250 profile from magnetic to non-magnetic elements (cases a & d of Table 3.1.2):

Table 3.2: Combinations of Field Strength and Fill Factor which Could Exist at the Mt. Wilson 5 Gauss Contour.

True Field (Gauss)	Fill Factor (a)	Fill Factor (d)
100	1.68E-1	5.64E-2
500	3.44E-2	1.21E-2
1000	2.01E-2	7.56E-3
1500	1.78E-2	7.19E-3
2000	2.00E-2	9.06E-3
2500	2.73E-2	1.51E-2

These factors should be particularly useful in predicting the signal strengths for compact magnetograph filter combinations using various lines since they are based on actual observations of the sun by an instrument with a comparable sampling aperture and represent roughly the weakest field strength which we wish to measure. The numbers given are estimates of the true area occupied by magnetic field. For any specific line, the expected magnetic signal will be additionally attenuated by the weakening of the line profile. For 5250, this effect should be self-correcting; that is, the stated fill factors combined with the profile changes of cases (a) and (d), as appropriate, should reproduce the observed signals very closely (even if the assumed profile changes are not quite correct) (see end of Sec. 3.5.5). For other lines, the results will be uncertain to the extent that the line weakenings are not well known.

In general, the effect of line weakening (which reduces the wing slope) is very similar to that of assuming a smaller-than-true fill factor. If there is no change in width, the effective fill factor is reduced in proportion to the loss in central depth of the line.

It may also be noted that for almost any magnetograph design, if the fill factor is very small, the predicted signal will be proportional to it, although the constant of proportionality depends on the intrinsic field strength, and the design parameters. Also, with a small fill factor, the bulk of the light comes from the undisturbed profile, and is therefore nearly independent of the fill factor, so that the integration time required to achieve a specific signal to noise level should be inversely proportional to the square of the signal.

Although, the intrinsic strength of the solar network elements (if single-valued) and the weakening or the 5250 profile in them are neither very well established at present, to continue to treat these as free variables makes unwieldy the number of possible combinations which need to be considered in comparing various magnetograph designs. From the preceding section, it is clear that much of the network field is probably in the range 500-1500 gauss. We therefore adopt as a standard weak field condition, a situation in which spatially unresolved magnetic elements of intrinsic strength 1000 gauss occupy .014 of the available area. According to Table 3.2, such a combination (with a true average field strength of 14 gauss) should correspond fairly closely to the 5-gauss nominal level of the Mount Wilson magnetograms.

In comparing various magnetograph designs, the choice of the fill factor is not terribly important, since the design which is optimum for one small fill factor should also be optimum for any other small fill factor. On the other hand, a design which provides the optimum integration time for an assumed field strength of 1000 gauss will not necessarily be the best if the actual strength if 500 or 1500 (primarily because the bandpass apropriate to one field strength will not be appropriate to the other). The most serious design errors would arise if the true strength is much greater than about 1500 gauss in which the case the point of maximum modulation begins to move significantly out in the wings, making it desirable to reject light near the core, and accept light farther out (cf. Figure 3.1.3). Observationally, this does not seem very likely. Additional design errors can occur if the behavior of the line chosen is very different than expected in the magnetic elements.

3.3 Possible Lines for Use with the Compact Magnetograph

The most recent listing of good Zeeman triplets is that of Harvey (Solar Phys. 28, 9, 1973). Because the displacement of each of the circularly polarized components from the nominal line center (in Angstroms) is given by

$$\Delta\lambda = 4.67 \times 10^{-13}\ g\ \lambda^2\ B \qquad (3.3a)$$

with λ in Angstroms and B in gauss, and since the turbulent width only increased in proportion to λ, the preference tends to be for lines towards the red end of the spectrum. The following figure illustrates some of the lines which have been frequently used or suggested. The profiles, which represent the intensity of an undisturbed region at disk center, are taken from the Kitt Peak Preliminary Photometric Atlas (Brault and Testerman, 1972 microfilm). They are not corrected for the instrumental width of the spectrograph which is on the order of 10 mÅ. The lines all show a slight asymmetry, with the red side (presumably formed by cool descending material) being slightly steeper than the blue (formed by relatively hot rising material).

By replotting the curves on graph paper it was determined that (within the uncertainty imposed by the asymmetry) each could be fit by a simple expression of the form:

$$I(\lambda) = I_o \left\{ 1 - \frac{D_o}{1 + \left| \frac{2(\lambda-\lambda_o)}{\mathrm{FWHM}} \right|^n} \right\} \qquad (3.3b)$$

where I_o is the continuum intensity and λ_o is the central wavelength. The coefficients required to fit the indicated lines were:

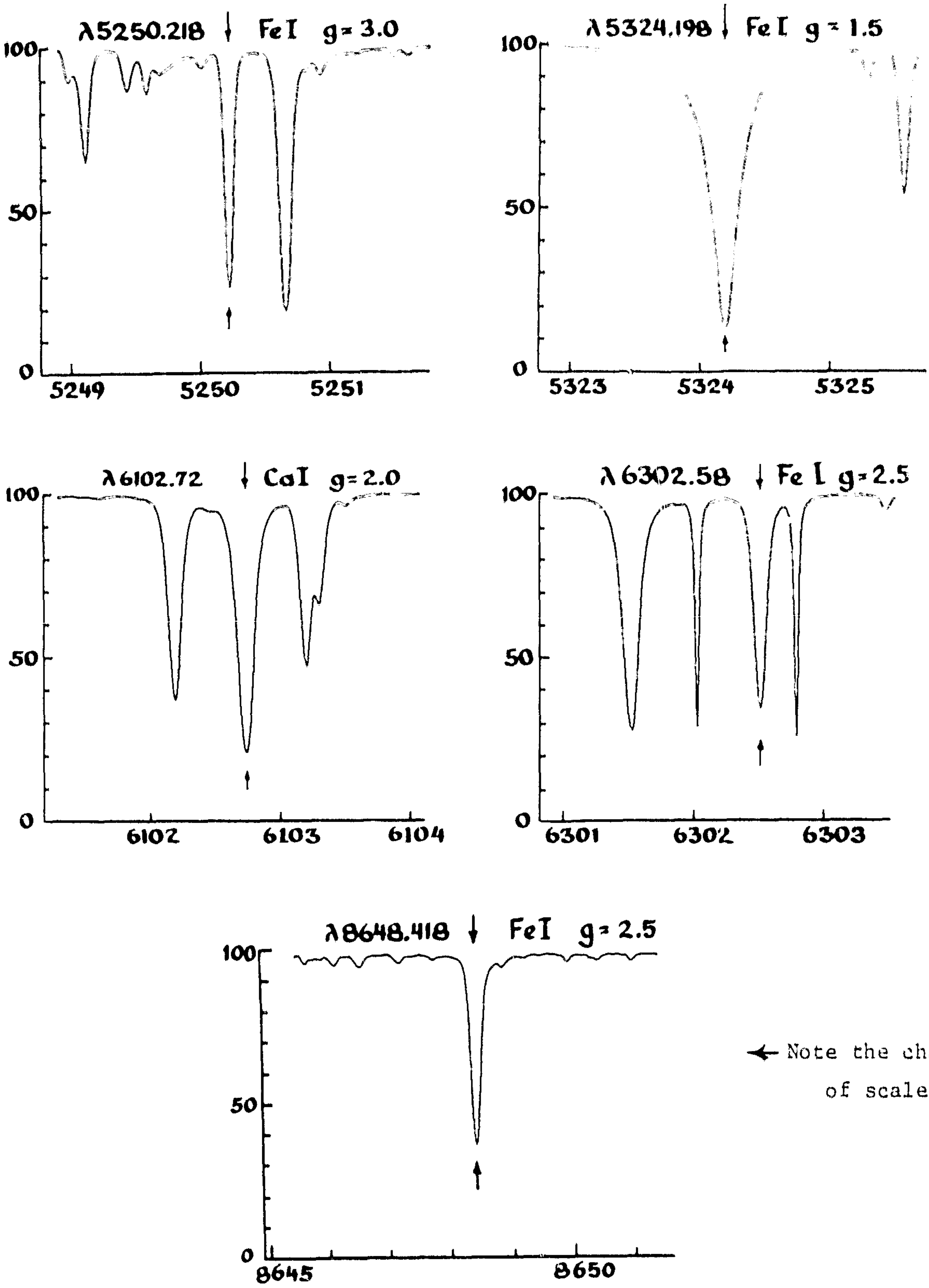

← Note the change of scale

Figure 3.3.1: Profiles of selected magnetically-sensitive lines from the Kitt Peak Photometric Atlas.

Table 3.3: Undisturbed Profiles of Magnetically Sensitive Lines

λ_0(Å)	D_0	FWHM	n	I_0	T_{atm}
5250.218	0.73	82 mÅ	3.0	3.86 E3	0.81
5324.198	.86	256 mÅ	1.9	3.77 E3	.81
6102.72	.78	152 mÅ	2.6	3.16 E3	.84
6302.58	.65	110 mÅ	2.5	3.03 E3	.86
8648.418	.62	184 mÅ	2.8	1.78 E3	.95

The unpolarized disk-center continuum intensities (outside the earth's atmosphere), which are in ergs/sr-cm^2-mÅ-sec, are from Allen's Astrophysical Quantities. They can be converted into photons/second by observing that one photon = 1.99 x $10^{-8}/\lambda$ ergs if λ is Angstroms. T_{atm} is the transmission coefficient at the stated wavelength for a light path through 1 atmosphere of "clear" air. The actual transmission is probably quite a bit lower.

3.4 Detailed Calculation of the Magnetic Signal and Integration Time for a Perfect Detector.

Given the fill factors of Sec. 3.2, the line profiles of Sec. 3.3, the Fabry Perot filter transmission properties of Section 2.2, and some assumption about the behavior of the line profile in the magnetic regions, it is a relatively straightforward matter to calculate the expected light levels in the two circular polarizations for a compact magnetograph configuration. At each angle in the detector plane, the filter profile (which is everywhere essentially the same, but shifted in wavelength) has to be multiplied by the incident solar intensity, and these answers added up over the range of angles which are to be used.

3.4.1 Calculation of the Signal for a Specific Filter Combination and Detector Plane Geometry

It can be shown that the number dN of photons available per second in a narrow range of width dλ in the Fabry Perot ring plane is given by:

$$dN^{rhc}_{lhc} = .465\ldots\ I_{cont}\ L^2 D^2 \lambda\ T_{atm}\ T_{opt}\ f^{rhc}_{lhc}\ \frac{d\lambda}{\Delta\lambda} \qquad (3.4.1a)$$

where I_{cont} = continuum intensity (ergs-sr^{-1}-cm^{-2}-mÅ^{-1}sec^{-1}; Table 3.3)

L^2 = area of sampling aperture (in square arc seconds)

D = diameter of objective (cm), half of the area of which is used for collecting each circular polarization

λ = wavelength (Å)

T_{atm} = transmission coefficient of atmosphere

T_{opt} = transmission coefficient of the optical components, including the filters (at their peak)

and $\Delta\lambda$ = total wavelength range covered by the objective.

The values used are indicated in Section 3.4.3. The factor f is a normalized convolution of the filter and spectral profiles:

$$f^{rhc}_{lhc}(r) = \int_{-\infty}^{+\infty} \frac{I^{rhc}_{lhc}(\lambda)\; T_{fil}(\lambda,r)\; d\lambda}{I_{cont}} \qquad (3.4.1b)$$

where $T_{fil}(\lambda,r)$ is the transmission profile of the filter combination at the radial position r in the detector plane (cf. eqns. 2.2d and 2.2j) and $I^{rhc}_{lhc}(\lambda)$ is the intensity profile of the spectral line in the area sampled, which depends on the field strength and fill factor in the manner indicated in equation 3.1.1 and has roughly the shape given in equation 3.3b. Note that the maximum value of I^{rhc}/I_{cont} or I_{lhc}/I_{cont} = 0.5 in the extreme wings of the line since I_{cont} includes both circular polarizations. The factor f is dimensional, and has units of Å. It varies with position in the detector plane, because the line profile is constant, but the filter profile shifts.

Now if the accessible range of wavelength in the detector plane is λ_o to λ_o-$\Delta\lambda$ angstroms, the actual measurement of magnetic signal will be based on the comparison of right- and left-handed counts detected in some finite range, say from λ_1 to λ_2 (where it understood that these fall within the accessible range). The total rates accepted by the detector will then be:

$$R^{rhc}_{lhc} = .465..\; I_{cont}\; L^2 D^2 \lambda\; T_{atm}\; T_{opt}\; F^{rhc}_{lhc} \qquad (3.4.1c)$$

where $$F^{rhc}_{lhc} = \frac{1}{\Delta r} \int_{r_1}^{r_2} f^{rhc}_{lhc}(r)\, dr \qquad (3.4.1d)$$

r_1 and r_2 are the radial positions in the detector plane corresponding to the limiting wavelengths and Δr is the total range in the same units. Exactly the same rate would be obtained if (as is more likely the case) the range of coverage extends from $\lambda_0 + \Delta\lambda$ to $\lambda_0 - \Delta\lambda$. This is because in the latter case one would be able to sample two wavelength ranges placed symmetrically in the wings. That is, the same rate is obtained sampling -40 to -50 mÅ with a total coverage of 0 to -90 mÅ as that obtained sampling +40 to +50 mÅ plus -40 to -50 mÅ with a total coverage of +90 to -90 mÅ.

As with the Mount Wilson magnetograph, the magnetic signal, S, is expressed as a modulation factor, and defined as:

$$S = \frac{(R_{rhc} - R_{lhc})}{(R_{rhc} + R_{lhc})} \qquad (3.4.1e)$$

Its magnitude depends, obviously, not only on the filter/line combination, but also on the limiting wavelengths which are selected, and on the magnetic field, which determines the amount of difference between $I_{rhc}(\lambda)$ and $I_{lhc}(\lambda)$. It does not depend on the overall normalization on factors.

3.4.2 Conversion of Signal Strength and Light Level into an Integration Time

Normally, the rates of collection of right-handed and left-handed photons will be very nearly equal:

$$R_{rhc} \simeq R_{lhc} = R_o \qquad (3.4.2a)$$

and also essentially equal to the rates which would be observed in a magnetically undisturbed region (since the fill factor is low). Due to photon counting statistics, it is evident that even in absence of any real difference between R_{rhc} and R_{lhc} there will still be an observed signal. The rms value of this null (noise) signal is:

$$\delta S = \pm \frac{1}{\sqrt{2R_o T}} \qquad (3.4.2b)$$

where T is the sampling time (in seconds). The errors from measurement to measurement will be distributed normally, that is, we expect errors of various magnitudes with the following frequencies:

Table 3.4.2: Probability of Exceeding Various Multiples of the rms Error.

Magnitude of Error	Frequency
$\geq \delta S$	1 in 3.15
$\geq 2\ \delta S$	1 in 22.0
$\geq 3\ \delta S$	1 in 370
$\geq 4\ \delta S$	1 in 15,800
$\geq 5\ \delta S$	1 in 1,740,000

In making a Mount Wilson-like raster scan of the full sun with a 12.6 arc second aperture, there are approximately 18,200 independent measurements involved, and the "threshold" field is generally taken as the lowest level which can be plotted with a negligible probability of erroneous contours. From Table 3.4.2 it is apparent that this would be about 4 times the rms noise level. That is, to be "useable" we have to require that the signal be detectable with a signal to noise of 4 or better:

$$\delta S \leq S_{min}/4 \qquad (3.4.2c)$$

In principle (for an ideal detector) this condition can be satisfied for any signal strength, S, simply by extending sufficiently the integration time:

$$T \geq 8/(R_o * S^2_{min}) \qquad (3.4.2d)$$

In practice, of course, the threshold can only be reduced to the point at which the systematic errors begin to show.

3.4.3 Optical Parameters Used in the Calculations

In the following calculations, the estimates of expected signal strengths and light levels are based on the following assumptions:

$D = 5.08$ cm (2 inches)
$L = 10$ arc seconds
$T_{opt} = 0.198$

The solar line profiles and atmospheric transmission taken from Table 3.3, and the Fabry Perot filter profiles are based on the parameters in Table 3.3, (the overall profile being taken as the product of the two treated separately, and the peak transmission being incorporated in T_{opt}). The estimate of T_{opt} is based on 45% transmission for the blocking filters, 70% for each of the two Fabry Perots and 90% for the analyzing polaroid in the "accepted" direction.

The integration times so-calculated are then, in some sense "ultimate" values. In reality the atmospheric (and probably the optical) transmission coefficients will be less than assumed. Also, the detector will have a less than perfect quantum efficiency and inject additional non-statistical noise. To compensate for these "errors", the calculated integration times will need to be increased, possibly by a large amount (see Section 4.2).

3.5 Optimization of the Magnetic Signal

3.5.1 Available Filters

Two different sets of Fabry Perot filters are under consideration for use in the compact magnetograph. Their characteristics are described in the following table:

Table 3.5.1: Possible Filters for Use in the Magnetograph

	Substrate Thickness (d_s)	Substrate Index (n_s)	Finesse
Existing set:	1.0 mm	1.45	27
	0.1 mm	1.45	20
Hoya filters:	.030 inch	1.5	20 (not yet made)
	.020 inch	1.5	20 (not yet made)

The spacing of the transmission peaks is such that either set could be used with a square 8 Å (i.e., ± 4 Å) blocker at 6302:

(a) Existing Filters:

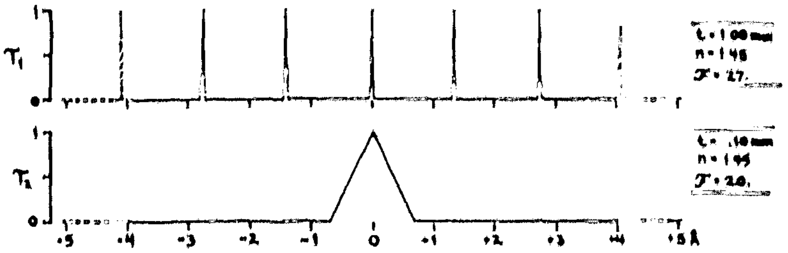

(b) Hoya Filters:

Figure 3.5.1: Bandpass patterns of the two filter sets. The dashed portions would be rejected by the blocking filters.

In the case of the Hoya filters, at least, the two components would be physically contacted so that the two sharp, spectrally matched central peaks could remain matched as the temperature is varied. If the contacting is performed in such a way that the two elements interact coherently (which probably means that the surfaces have to be accurately parallel) then the combination will act as a two cavity etalon. This gives a slightly different transmission profile than might be expected from the product of the two filters treated independently. In particular, it is expected that the transmission would be slightly lower in far wings, some of the missing light showing up in a slightly squarer central peak. As indicated above, this would tend to improve its usefulness in the magnetograph, but since the exact profile was not calculated, the two elements were treated independently.

3.5.2 Optimization of the f-number

The considerations involved in securing the optimum magnetic performance (minimum integration time) are similar to those discussed in connection with the performance of the Mount Wilson magnetograph (Section 3.1.5), but the number of free parameters is somewhat larger. As with a spectrograph, in order to obtain the optimum magnetic signal, some care must be exercised in the choice of both the width and shape of the filter profile and in selecting the range of the output to be sampled. A very broad filter will obviously produce a poor signal, since the effective line profile will be washed out and incapable of significant modulation. On the other hand, if the width is reduced too much, the modulation will not increase after a point, but the light level will go down, causing an increase in the integration time required to measure the signal. Similarly, if the filter has too broad of wings, the introduction of the extra, umodulated stray light, will both decrease the signal and increase the noise level, again leading to longer integration times.

The range of transmitted wavelengths available to the detectors is determined, in the case of the compact magnetograph, by the f-ratio of the beam through the filter. Ideally, one would want to use a very large f-number (i.e., nearly collimated light), and tune the filter so that the filter's transmission peak for light falling anywhere in the detector plane (and equivalently for light originating anywhere on the objective) corresponds to the optimum point of modulation in the wing of the spectral line. Unfortunately, it is felt that active temperature control will be needed to hold the filter within tolerances, and therefore, a smaller f-number (i.e. a divergent or convergent) beam has to be used, so that a wide enough range of transmitted wavelengths will be present at the detector plane to permit the core of the line to be located. As indicated earlier, this would be done in such a way that the filter would transmit the core of the line at a point 0.707... of the way from center to edge, which would make light falling at the center and outer edge of the detector plane correspond to points symmetrically spaced in the red and blue wings (respectively). The total wavelength range from the center to the edge of the detector plane is given by:

$$\Delta\lambda_{tot} = \frac{\lambda_0}{8(n_s \cdot f\#)^2} \qquad (3.5.2)$$

How large should this wavelength range be? If it is too small, the only part of the line accessible to examination will be that near the center of the line, which is dim and not very sensitive to the magnetic splitting. On the other hand, if the range is too large, much of the objective area will be wasted in collecting light far out in the wings of the line, which is bright, and again, not very well modulated. Clearly there must be some optimum between these two unfavorable extremes. This optimum can most easily be evaluated numerically by calculating the integration time required with various f-numbers. As with the Mount Wilson-type magnetograph (cf. Fig. 3.1.5a), the integration time can also be somewhat improved by rejecting a little of the light very close to the line core. As an example, with 6302, if the intrinsic field strength is 1000 gauss or less, the minimum integration is typically found by allowing the detector to view the range -90 to 90 mÅ around line center, which requires an f-number of about 45.

The detailed dependence of the optimum range (which depends very little on the assumed filter profile) is given in Figure 3.5.2 for a typical case as a function of the intrinsic field strength.

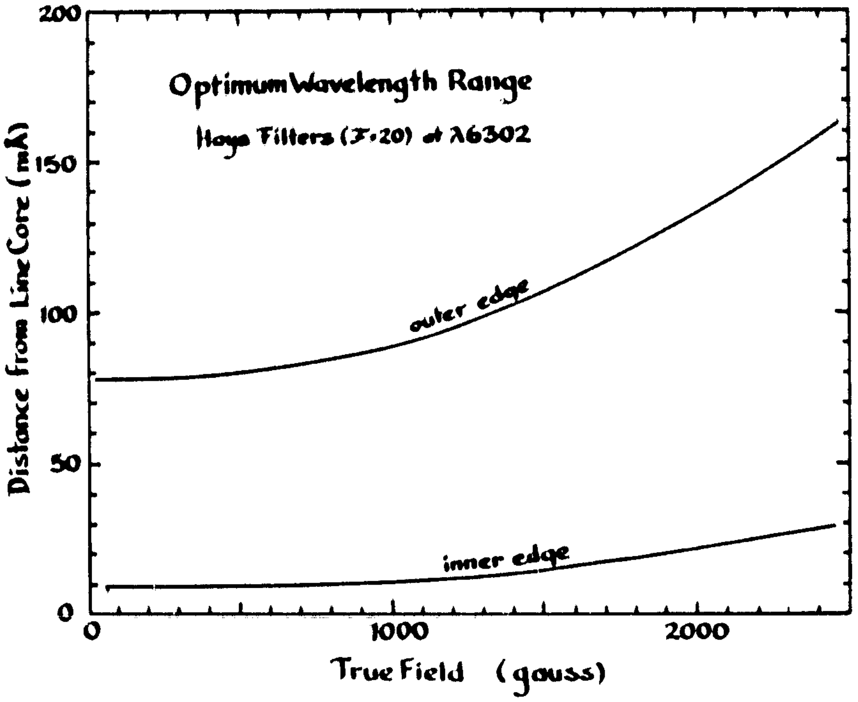

Fig. 3.5.2: Optimum sampling range in the detector plane for a compact magnetograph viewing both wings of 6302 (as a function of field strength).

The nature of this optimum is such that if for some other reason (e.g., to view a telluric line) the instrument is designed so that a larger range is available to the detector, it will actually be desirable (for purposes of the magnetic measurements) to mask off or otherwise reject this additional light. The integration times will obviously need to be increased to compensate for the area of the objective which is not being used but if the additional light had not rejected they would have had to have been increased even further to make up for the added noise introduced by the extraneous photons.

In summary, if both wings of the line need to be viewed there will always be some optimum range giving the best tradeoff between signal strength and light level. The f-number should be chosen to reproduce as nearly as possible this range, and the detector should be designed to sample from near line center to the extreme edge of the range. The optimum range depends, however, on the inherent field strength.

3.5.3 Importance of Profile Shape

The importance of the profile shape and the blocking of the sidelobes is reflected in the following table, where the performance of the magnetograph has been evaluated imagining that we could substitute for the actual Fabry Perots an ideal filter having the same angular dependence, but various simplified transmission profiles. The Fabry-Perot type peaks are assumed to be blocked for all wavelengths beyond the middle of the first free spectral range.

In each case, the optimum FWHM for the configuration has been evaluated, and the integration times are on the assumption that the optimum wavelength range is sampled in the detector plane. The signal strengths are based on a 1000 gauss field with a fill factor of .014. The line 6302 is assumed to have 74% of its normal depth in the magnetic features (26% line weakening). The count rates are in photons/sec, and the integration times in seconds for an ideal detector.

Table 3.5.3a: Performance of Various Ideal Bandpasses in a Compact Magnetograph Configuration at 6302Å (Perfect Detector).

	Range	R_{rhc}	R_{lhc}	S_{mag}	T(S/N=4)
Square Bandpass (90 mÅ FWHM)	10-80	8.932E7	8.880E7	2.96E-3	9.92E-3
Two narrow Fabry Perot peaks in series (90 mÅ each – 58 mÅ effective FWHM)	10-90	7.588E7	7.549E7	2.55E-3	1.63E-2
One Fabry Perot peak (40 mÅ FWHM)	10-90	7.977E7	7.944E7	2.05E-3	2.40E-2

The actual performance which could be obtained with the planned filters (as specified in Table 3.5.1) under the same circumstances, but including the full profile out to the blocking points at ± 4Å (see Figure 3.5.1) would be:

Table 3.5.3b: Performance Obtainable with Available Filters Under the Same Circumstances

	Range	R_{rhc}	R_{lhc}	S_{mag}	$\mathcal{T}(S/N=4)$
Hoya filters ($\mathcal{F}=20$) (67 mÅ eff. FWHM)	10-90 mÅ	1.041E8	1.037E8	2.01E-3	1.91E-2
Existing filters (51 mÅ eff. FWHM)	10-90 mÅ	1.089E8	1.085E8	1.63E-3	2.79E-2

It is evident from the two tables that while the square bandpass is certainly the best, some of the Fabry-Perot configurations don't finish very far behind. In fact, if the Hoya filters were finished to a slightly higher finesse, and so that they had equal FWHM's (rather than equal finesse), their theoretical performance would be virtually indistinguishable from that of the "two narrow Fabry Perot peaks", the importance of the few additional unblocked sidelobes being negligible; and if they were combined coherently, so as to make a "two-cavity" etalon, their performance would probably be even close to that of the ideal square bandpass.

The performance of the "existing" filters, which <u>is</u> to some extent limited by the side-lobes, would not be significantly improved by going to a higher finesse.

3.5.4 Optimization of Filter Width

The dependence of the integration time on the width of the filter transmission peaks is shown in Figure 3.6b, where the performance of the Hoya filters has been considered as a function of finesse (which is related to the filter width via equation 2.2e). It is assumed that both filters are coated to the same finesse, and that their transmission profiles can be combined incoherently.

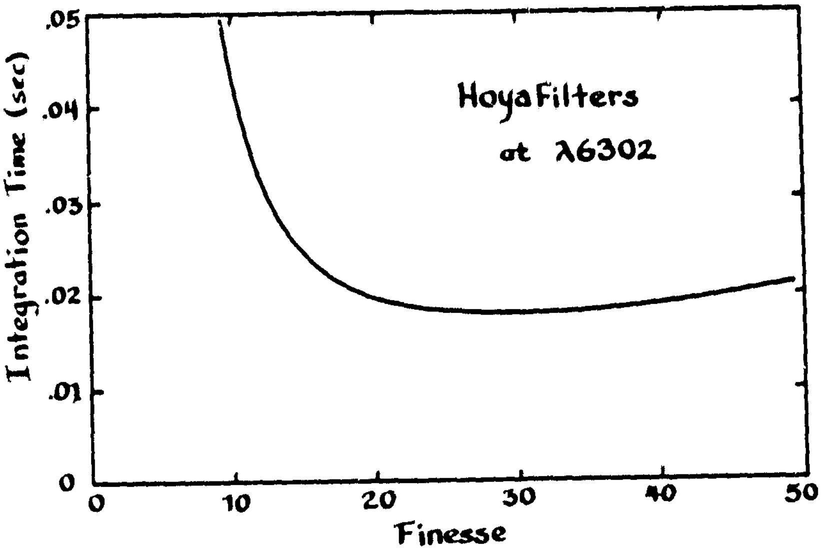

Figure 3.5.4: Integration time required to measure a weak magnetic signal with Hoya filters coated to various degrees of finesse (and a perfect detector).

At each finesse the optimum wavelength range is used. Below a finesse of about 15, the performance drops precipitously due to the large amount of stray light. Above a finesse of about 30, the performance also drops, due to the excessively narrow width and the consequent low transmission, but the effect is surprisingly slight.

Again, the integration times have been calculated on the assumption that we are trying to measure a field with an intrinsic strength of 1000 gauss and a fill factor of .014 to a signal to noise of 4; and that the line 6302 has a central depth 74% of its normal one in the magnetic regions ("26% line weakening).

3.5.5 Choice of the of Spectral Line

The preceding sections may have given the impression that the expected magnetic signal strengths and integration times can be predicted with great precision. This is true only to the extent that we are willing to make somewhat arbitrary assumptions about the nature of the solar fields and the behaviour of the spectral lines. That is, we can be fairly confident about the relative performance of the various filter design choices, but much less confident about the absolute performance of any of them. Figure 3.5.5 gives a more accurate picture of the actual uncertainties:

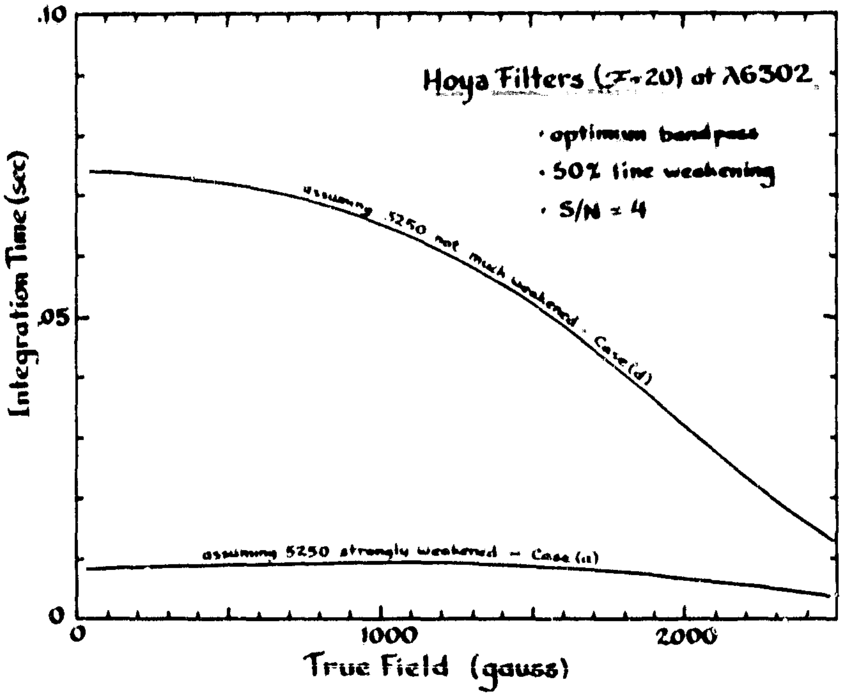

Figure 3.5.5: Integration times required for various possible field and fill factor combinations corresponding to Mt. Wilson 5-gauss contour as a function of intrinsic field strength (perfect detector).

The figure has been calculated using the various combinations of field strength and fill factor listed in Table 3.2. There is up to a factor of 7 uncertainty in the integration time which would be required to bring out this threshold field. In addition, one has to make some assumption about the behavior of the line selected. For example, in generating the figure we have assumed that 6302 is weakened (in central depth) by 50% in the magnetic regions. If it were actually not weakened at all, then the integration times might be four times shorter, whereas if it were even more strongly weakened, the integration times might be longer than stated.

Given these large uncertainties, it is difficult or impossible to make any definitive statement as to which spectral line will give the best results. A line which looks good on the basis of its splitting and nominal undisturbed profile may in fact be a poor choice due to an unusually large amount of weakening in the magnetic features. Moreoever, the line which seems best for one intrinsic field strength will not necessarily be the best choice if the real intrinsic field strength is something different (the fatter lines, like 6103, tend to do better if the true field is very strong; and the skinny ones, like 5250, if it is weak).

In the following Tables we have assumed that the intrinsic field strength is 1000 gauss, and that there is a fill factor of .014. As was seen earlier, this is a likely combination to exist in areas registered as "5 gauss" (even though the real field is 14) on the Mount Wilson magnetograms. We have however for simplicity of comparison uniformly ignored the possibility of line weakening, which will make the estimates of signal strength and integration time somewhat overly optimistic.

In Table 3.5.5a, the performance of the "existing filters" (see Table 3.5.1) has been calculated at various possible wavelengths. The finesse has been kept as stated, and the ± 4 Å blocking width increased or decreased in proportion to the square of the wavelength.

The count rates are for one circular polarization in photons/sec and the integration times in seconds (for a signal-to-noise of 4).

Table 3.5.5a: Performance Obtainable with Existing Filters by Using Different Lines (Perfect Detector and No Line Weakening)

Line (Å)	f-num	Range	R_o	S_{mag}	T
5250	47.2	10 - 70 mÅ	7.02 E7	3.10 E-3	1.18 E-2
5324	37.9	10 - 110 mÅ	4.88 E7	7.46 E-4	2.97 E-1
6103	42.6	10 - 100 mÅ	8.42 E7	2.48 E-3	1.55 E-2
6302	45.6	10 - 90 mÅ	1.09 E8	2.20 E-3	1.52 E-2
8468	39.7	20 - 160 mÅ	1.75 E8	2.15 E-3	9.92 E-3

For the Hoya filters, since they are not yet made, the finesse was also considered as a free variable. It was assumed that both pieces would be finished to the same finesse and combined incoherently, which is not quite the optimum situation (Section 3.5.3).

Table 3.5.5b: Performance Obtainable with the Hoya Filters Under the Same Conditions

Line(Å)	Finesse	F-num	Range	R_0	S_{mag}	T
5250	30	49.3	10 - 60 mÅ	3.71 E7	5.34 E-3	7.58 E-3
5324	20	36.7	10 - 110 mÅ	4.22 E7	2.04 E-3	4.59 E-2
5103	25	43.4	10 - 90 mÅ	5.40 E7	3.93 E-3	9.57 E-3
6302	30	46.8	10 - 80 mÅ	6.00 E7	3.73 E-3	9.60 E-3
8468	30	41.0	20 - 140 mÅ	9.74 E7	3.63 E-2	6.24 E-3

The two tables suggest that there is very little difference between the three principal visible lines (5250, 6103 and 6302); and that all of these are much better than the line λ5324 (which is included for comparison because in spite of its poor signal it was used fairly successfully in early photographic cancellations by Ramsey at Lockheed and in the Smithson videomagnetograph at Big Bear).

The additional loss in performance due to line weakening is difficult to generalize, except in the sense that signal will be reduced in proportion to the loss in central depth, and the integration time increased, therefore, in proportion to its square. For the line λ5250, putting back in the earlier line weakening assumptions, one can estimate that the likely signal with the Hoya filters would be on the order of $S_{mag} = (1.6 - 2.2) \times 10^{-3}$ (which is slightly smaller than the Mt. Wilson "5 gauss" signal due to the less than optimum spectral profile) dictating an integration time of $T = (2.7 - 3.9) \times 10^{-2}$ seconds, that is 3.5 to 5 times longer than the stated time. The other lines probably suffer less from line weakening.

As a final note regarding the selection of the spectral line we might observe that there is a strong bias towards excluding from the standard lists any line with a complicated Zeeman pattern. At least for measuring longitudinal fields there is no particular reason to do this. The things that matter are the shape of the normal and disturbed profiles and the strength of the average splitting, not the detailed pattern. It is, therefore, quite possible that some better lines have been overlooked. A more profitable approach would probably have been to have thought first about what line depths and shapes would be expected to give the best performance (i.e., neither too narrow nor too broad), then to have looked through the Atlases to see what was available with these shapes, and then finally to have asked how much they split and whether they are weakened in the network.

3.5.6 Advantage of Using One Wing of the Line

It was earlier observed that ideally, to obtain the shortest integration time, one would really prefer to work in only one wing of the line with a nearly collimated beam. To indicate exactly how much is lost by using the dual-wing ring plane configuration, the following table indicates for the same lines the performances which could be obtained by operating using the Hoya filters at the optimum point in one wing. Again, the signal strengths and times are based on the assumption of 1000 gauss, .014 fill factor, and zero line weakening (it is therefore directly comparable to Table 3.5.5b). The f-number, if indicated, would be very large.

Table 3.5.6: Integration Times Obtainable with the Hoya Filters Using the Entire Objective at the Optimum Position in One Wing (Perfect Detector)

Line (Å)	Finesse	Position	R_o	S_{mag}	T
5250	25	40 mÅ	5.91 E7	5.26 E-3	4.90 E-3
5324	20	70 mÅ	4.96 E7	2.31 E-3	3.02 E-2
6103	25	60 mÅ	6.60 E7	4.46 E-3	6.10 E-3
6302	30	50 mÅ	7.14 E7	4.25 E-3	6.18 E-3
8468	30	90 mÅ	1.19 E8	4.11 E-3	4.00 E-3

The reduction in integration time in each case amount to a factor of a little over 1.5.

3.6 Effect of Sampling Aperture and Integration Time on the Threshold Field

All of the calculations up to this point have assumed (cf. Section 3.4.3) somewhat arbitrarily (but for the sake of consistency, that the measurements would be performed with a square sampling aperture measuring 10 arc seconds on a side. Whether or not this is an optimum choice depends on the purpose of the program.

To the extent that there is no rigid requirement on spatial resolution there can be an engineering tradeoff between light level and signal strength. Observations made with an extremely small aperture will tend to give larger signals by obtaining (on occasion) a better ratio of field elements to dead space (i.e., a higher effective fill factor). Observations made with a very large aperture, on the other hand will tend to give smaller signals because of the cancellation of opposite polarity featurs in the field of view. The following table, derived from a variety of sources, suggests the approximate dependence of observed field on the dimension, L, of the sampling aperture.

Table 3.6: Maximum Nonsunspot Fields Measured in 5250 by Various Magnetographs

Source	Aperture (L)	Max. Field (B)
Kitt Peak	2.4 arc sec	100 gauss
Mount Wilson	12.6 arc sec	40 gauss
Stanford	180 arc sec	12 gauss
Stanford	1700 arc sec	0.5 gauss

As expected, these measurements show a fairly regular fall-off of field strength with aperture:

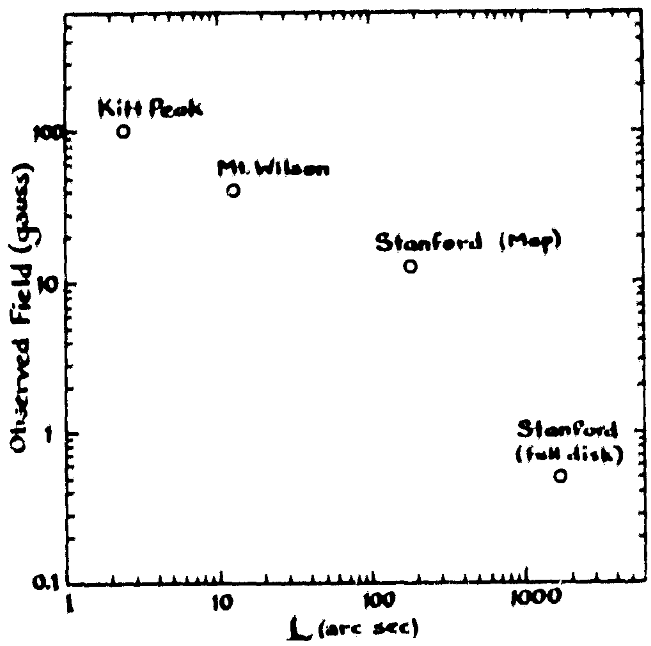

Figure 3.6a: Maximum Observed Non-Sunspot Fields in 5250 with Various Sampling Apertures.

Since presumably no effort has been made to correct any of these values for line weakening or saturation, they do not represent actual physical field strengths. On the other hand, since they were all made with the same line they should be fairly representative of the relative observed signal strengths. That is, we can say $S \sim B$. Likewise, for any fixed magnetograph configuration (ignoring limb darkening) the basic light level will be proportional to the square of the sampling aperture: $R_0 \sim L^2$.

As will be developed in Section 4.2, the implication of these relations for the ability to detect the fields will depend on whether the detectors are operating in a mode where they are limited in accuracy by the intrinsic photon-counting statistics (the high light level situation), or by fixed noise contributions originating in the detector and electronics (the low light level situation). In both cases the time required to make a measurement of a given accuracy is proportional to the square of the expected signal. In the former case it is also inversely proportional to the light level (that is, a fixed number of photons need to be collected). In the latter case it varies with the square of the light level. Thus we are likely to have either:

$$\text{(high light level/photon-limited)} \quad T \sim \frac{1}{R_0 S^2} \sim \frac{1}{L^2 B^2} \qquad (3.6a)$$

or

$$\text{(low light level/noise-limited)} \quad T \sim \frac{1}{R_0^2 S^2} \sim \frac{1}{L^4 B^2} \qquad (3.6b)$$

or something between the two extremes. Using the values from Table 3.6 we can therefore estimate the relative integration times which would be required to detect <u>any</u> non-sunspot field with the various apertures:

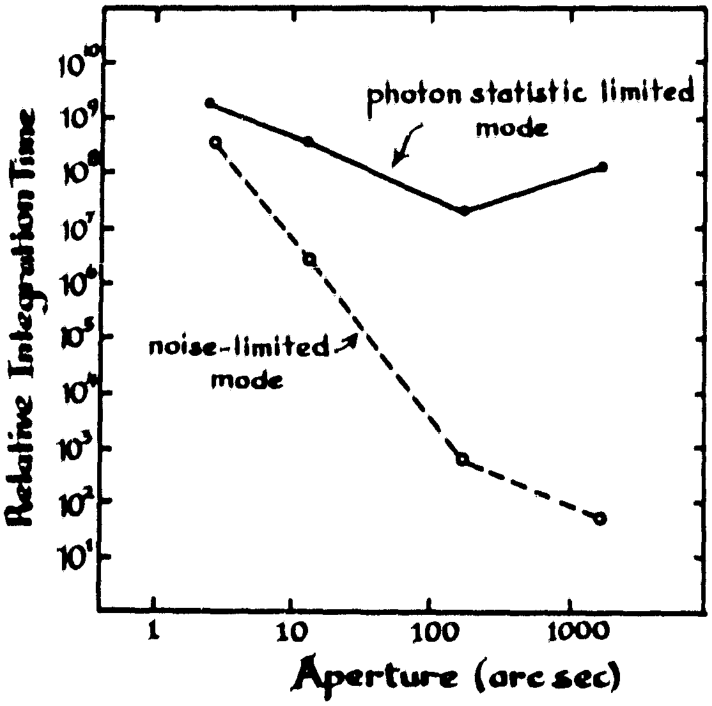

Figure 3.6b: Relative integration times required to detect any non-sunspot field with various sampling apertures. The absolute time scales depend on the magnetograph, and the placement of the two curves is not meant to imply that the "noise-limited" times are shorter than the "photon-limited".

It is clear from the figure that in either counting regime the increase in light level obtained by increasing the sampling aperture will more than outweigh the loss in signal strength, at least up to apertures of several arc minutes. The moral is that one should never use an aperture smaller than absolutely necessary to achieve the required spatial resolution.

While there is a definite physical limit to the strongest fields which will be encountered, the weakest ones are limited only by one's patience and skill in performing the measurement. In general, the noise level will be reduced in proportion to the square root of the sampling time, and since the threshold field strength will be proportional to the noise level, it is therefore apparent that once the minimum time to see any field has been exceeded, the "dynamic range" of the magnetograms should increase in proportion to the square root of the additional integration time.

4. Operational Considerations

4.1 Maximum Time Acceptable for Full Disk Raster Scans

Since the solar magnetic features change more rapidly when examined on a fine than on a large scale, the maximum times which would be considered acceptable for completing a map is also somewhat a function of the nominal resolution. The Mount Wilson full disk maps, with a sampling aperture of 12.6 x 12.6 arc seconds are done in about 2 hours. During this time, features near disk center will rotate by about 20 arc seconds, which is larger than the resolution element, but this does not cause a perceptible shearing in the image since the few scan lines including any particular features will have been completed in a much shorter interval. For a space application, it is not inconceivable that in a continuously scanning mode times as long as 24 hours might be permissible for the complete cycle.

In a ground-based operation, however, in order to have a significant probability of completing the task without undue interruptions from clouds and other problems it would certainly be wise to plan the program so that the scan could be completed in less than, say, 4 hours. If a 10 by 10 arc second aperture is used, it would require approximately 29,000 separate measurements to cover the full disk. To do this in 4 hours, one could not spend more than 0.5 seconds on each point. It is, of course, possible to avoid some of the time limitations by making smaller scans of selected regions rather than of the whole disk.

4.2 Selection of a Suitable Detector

The integration times calculated in the previous sections have assumed that an "ideal" detector could be used. A real detector will, of course, miss some of the photons and add noise and background currents to the apparent light levels. For purposes of demonstrating the feasibility of the magnetograph concept, this is not necessarily a critical problem, since most such defiencies can be corrected simply by extending the integration time. Nonetheless, it seems reasonable to try, as much as possible, to use the optimal detector.

4.2.1 Expected Light Levels

In general, the selection of a suitable detector will depend both on the total quantity of light (photons/sec) and on its expected intensity (photons/cm^2-sec) in the detector plane. In the case of the compact magnetograph, the intensity can be varied almost arbitrarily by changing the diameter of the area into which the light is imaged, but the quantity of light cannot. According to Table 3.5.3b for the line 6302 operating under optimal conditions (that is with the system operated at the minimal range of wavelength coverage, and with very clear skies) we expect to gather about 1×10^8 photons/second in each circular polarization (using half of a 2" diameter objective). This amounts to an available power of about 3.1×10^{11} watts. The spatial distribution of the intensity is reasonably uniform, the ratio between the brightest and darkest parts of the image (i.e., ± 90 mÅ vs. line center) being about 1.5.

4.2.2 CID Cameras

The CID camera being considered for use consists of 244 x 248 silicon elements, or pixels, which can be read out sequentially in a total time of 0.5 seconds, with a readout noise of ± 500 counts/pixel. The faceplate geometry is shown in Figure 4.2.2a:

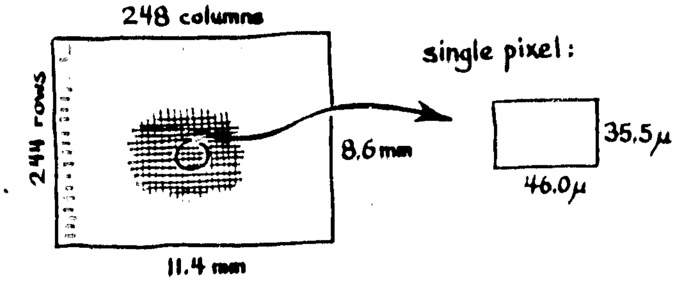

Figure 4.2.2a: Faceplate geometry of the existing GE CID camera.

The sensitivity of the elements appears to increase as the charge builds up, reaching a peak quantum efficiency of about 0.3 in the range between 4 x 10^5 cts/pixel (the "bias level") and 2.5 x 10^6 cts/pixel (saturation). In general, according to the figure distributed by Aikens (AURA Engineering Technical Report #66, 1980), the relationship between the number of photons striking a pixel (N_{in}) and the number of charges collected (N_{out}) can be written in the form:

$$\begin{array}{lll} N_{out} = 1.8 \times 10^{-7}\ N_{in}^2 & \text{for}\quad 0 \leq N_{in} \leq 4.9 \times 10^5 & \\ N_{out} = .195\ N_{in} - 5.23 \times 10^4 & \text{for}\ 4.9 \times 10^5 \leq N_{in} \leq 1.33 \times 10^6 & (4.2.2a) \\ N_{out} = .300 N_{in} - 1.93 \times 10^5 & \text{for}\ 1.33 \times 10^6 \leq N_{in} \leq 8.77 \times 10^6 & \\ N_{out} = 2.44 \times 10^6 & \text{for}\ 8.77 \times 10^6 \leq N_{in} & \end{array}$$

The quadratic behavior at low charge levels is so bothersome that in many applications, it is considered desireable to "prefog" the elements up to the bias level, so that reasonable efficiency and linearity of response can be obtained. Such a mode would probably, however, be incompatible with the rastering action of the magnetograph (see Section 4.2.3), since it would require a shutter to block off the incoming light during the time it takes to pre-expose and readout the background level.

The dark current in the CID, or more precisely, the dark charge per pixel builds up at a rate of about 6000 cts/sec at -32 °C. As with other silicon devices, this can be supressed factor of 2 for every 7-10 °C of additional cooling.

The useability of the CID depends largely on the nature of the associated electronics, which determine the complexity of reading out a particular element. For the present purpose, we shall consider an idealized camera in which it is possible to read out any element instantaneously (that is, with no time lost for "addressing"). In particular we shall consider a situation in which m pixels are used for detecting each circular polarization, and in which the total detector area of 2m pixels is readout sequentially in a total time of T (seconds). The charge on any one pixel will look like:

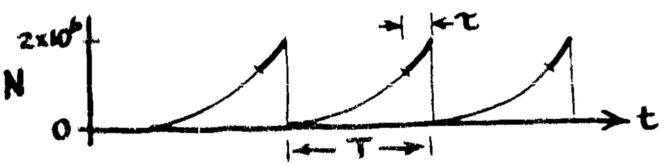

Figure 4.2.2b: Charge on a single CID pixel for a camera used in a continuous scanning mode.

As indicated, the charge on a particular pixel is read out in a short time τ, and then reset. The maximum value of τ is:

$$\tau_{max} = \frac{T}{2m} \qquad (4.2.2b)$$

Since the effective integration time is T - 0.5τ, it may under some circumstances be desireable to shorten τ so that a larger charge will be available for measurement. This would, however, increase the readout noise. Since the readout noise is currently ± 500 counts for a sequential readout of the complete 60,000 pixels in 0.5 sec (8 μsec/pixel), one guesses that the readout noise for an arbitrary τ would be:

$$\delta n = \pm 500 \left(\frac{8\ \mu sec}{\tau}\right)^{0.5} \text{cts.} \qquad (4.2.2c)$$

The total uncertainty, δN, in the number of charges measured is then:

$$\delta N = \sqrt{\bar{N} + \delta n^2} \qquad (4.2.2c)$$

where $\bar{N}$ is the average number of charges recorded, which is related to the input number of photons in the time T - 0.5 τ by equation 4.2.2a.

In the case of the compact magnetograph, we will have R_1 photons/sec of right-hand circular light falling on one set of m pixels, and R_2 photons/sec of left-hand circular light falling on the other set, where $R_1 \approx R_2 \approx R_o$ and will wish to measure the signal:

$$S = (R_1 - R_2)/(R_1 + R_2) \qquad (4.2.2d)$$

If the dark current is negligible, it can be shown that the uncertainty δS in the measured value of S will be given by:

$$(\delta S)^2 = \frac{1}{2m} \frac{\left\{ f\left(\frac{R_o(T-5\tau)}{m}\right) + (500)^2 \left(\frac{8\ \mu sec}{\tau}\right) \right\}}{f^2 \left(\frac{R_o(T-5\tau)}{m}\right)} \qquad (4.2.2e)$$

where R_o (T - 0.5τ)/m is the number of photons collected per pixel and f is the function relating this to the number of counts registered (eqn. 4.2.2a). For any specified values of S and m, this equation can be investigated numerically to determine the readout time which will give the minimum cycle time T. The total number of photons of each circular polarization which must be collected to make the stated measurement is then $N=mR_oT$. By way of comparison, for an ideal noiseless, and perfectly-efficient detector, the number required would be (cf. Sec. 3.4.2):

$$N = \frac{1}{2(\delta S)^2} \qquad (4.2.2f)$$

In the following figure, the calculated integration times are given for the idealized continuous-scanning CID camera with various sizes of image area on the assumption of an incident rate of R_o=10^8 photons/second.

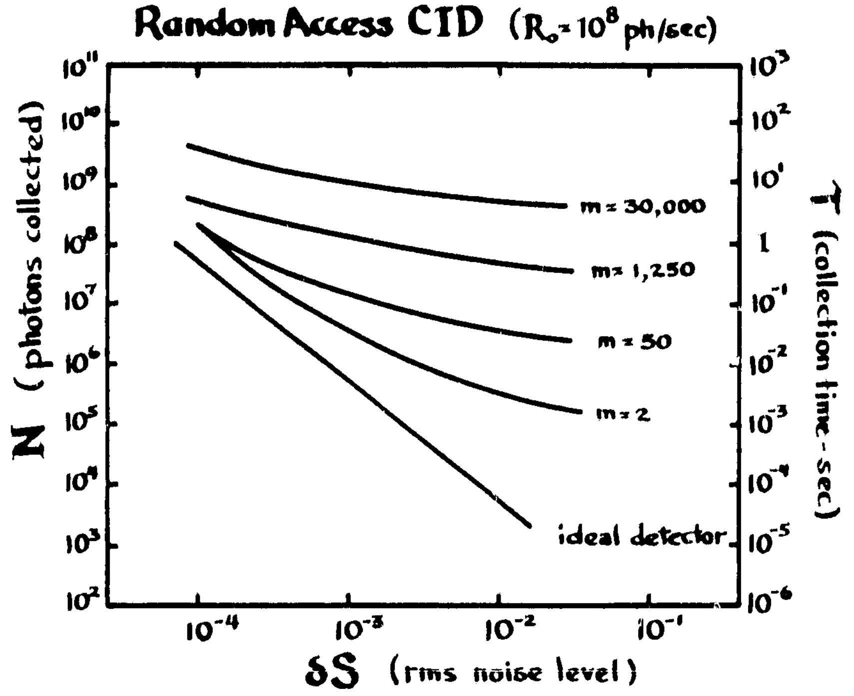

Figure 4.2.2c. Minimum integration times required for various noise levels. m is the number of CID pixels used for each circular polarization. Note that for magnetic measurements we want the noise level to be less than one-fourth the expected signal at the threshold field.

In general, the optimum performance was found by using the longest possible readout times (that is, $\tau = T/2m$). The only exception occurred when a high precision result was wanted using a very small number of pixels ($m=2$). In that case, where relatively long integration times are called for, no improvement in the noise level was found for readout times longer than about .001 sec; in fact longer times would cause a slight deterioration in performance due to the smaller average number of charges which would be present during the readout.

In using eqn. 4.2.2e, allowance must be made for the possibility that the total number of charges accumulated per pixel between resets ($=f(R_o T)$) may try to exceed the saturation level. This occurred, for example, for $m=2$ when $\delta S < 3.5 \times 10^{-4}$. In such cases, the desired noise level can only be obtained by averaging together a number of measurements made with cycle times short enough to avoid saturation. This causes the curve of collection time vs. noise level to become parallel to that for an ideal detector at low noise levels (as shown in Figure 4.2.2c).

The general conclusion would seem to be that when using a CID for the kinds of light level available from the compact magnetograph it is desireable to reduce the image area to the smallest number of pixels consistent with the required spatial resolution. The smallest number of pixels which could be used for each circular polarization for a combined magnetic/temperature measuring capability would be about $m = 6$:

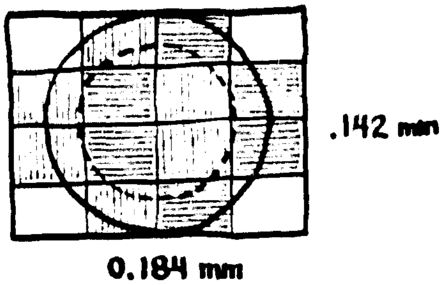

Figure 4.2.2d: A minimal image scale permitting the 4 detection sectors to be sampled for independent "velocity" and magnetic measurements (cf. Figure 2.4a).

However with a very small number of pixels, the performance would be additionally degraded by the fact that some of the pixels would cross the boundaries of the detection sectors, and others would be incompletely illuminated. That is, the sectors are non-optimal and for geometric reasons the signal levels would be somewhat lower, and the noise levels higher, than anticipated.

In summary, for the compact magnetograph, adequate resolution could probably be obtained with $m \approx 10$, and the noise level of $\delta S = 5 \times 10^{-4}$ (which according to Sec. 3.5 is that required to measure the Mount Wilson 5-gauss fields with negligible error in 6302) could be obtained in an integration time of about 0.2 seconds. 2×10^{7} photons of each circular polarization would be collected, which means that 2×10^{6} photons would strike each of the active pixels. According to eqn. 4.2.2a, this in turn means that a total of about 4×10^{5} counts would be accumulated by each pixel between resets. Since this is roughly equal to the room temperature dark charge per pixel for 0.2 seconds, some cooling would be required.

Since the existing CID cannot be used in a random access mode, a longer integration time would obviously be required, but exactly how much longer is somewhat unclear. Even if it were necessary to read out the entire picture using T = 0.5 sec and τ = 8 μsec, we could still choose to use an image covering m = 10 pixels (for each circular polarization) and ignore the others. In such a case, according to eqn. 4.2.2 the noise level would be $\delta S = 2 \times 10^{-4}$. This is more than good enough for the magnetic measurement. Still closer to optimum performance might be achieved if just a portion of the pixture could be read out, or if the unused pixels could be stepped over more rapidly than the "active" ones. The exact solution would depend on the operating possibilities.

For example, if it happened that a few lines of the image could be read out selectively, and if a polarizing mask of type II were used (Figure 2.4b) so that longitudinal magnetic fields produce a pure left-right blinking, it would be possible to use a cylindrical lens to focus the detector plane image down onto those few lines with essentially no loss in magnetic signal:

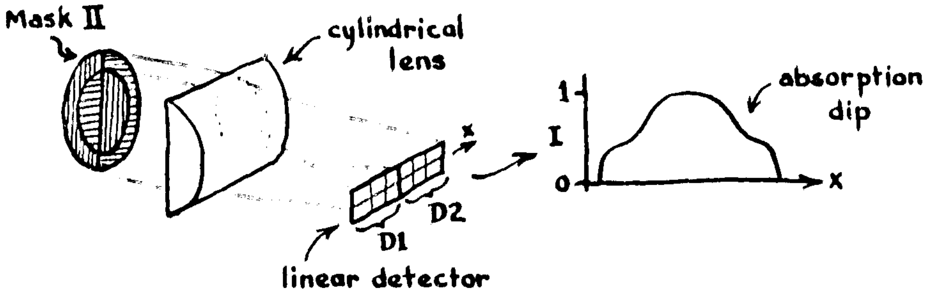

Figure 4.2.2e: Use of a cylindical lens to compress the detector plane image onto a linear detector array. The picture on the right shows the intensity profile along the length of the detector.

The magnetic signal could then be derived in the usual way, by comparing the intensities in two halves of the detector. The temperature information would be derived from the motion of the intensity dip (due to the line absorption) in the linear image:

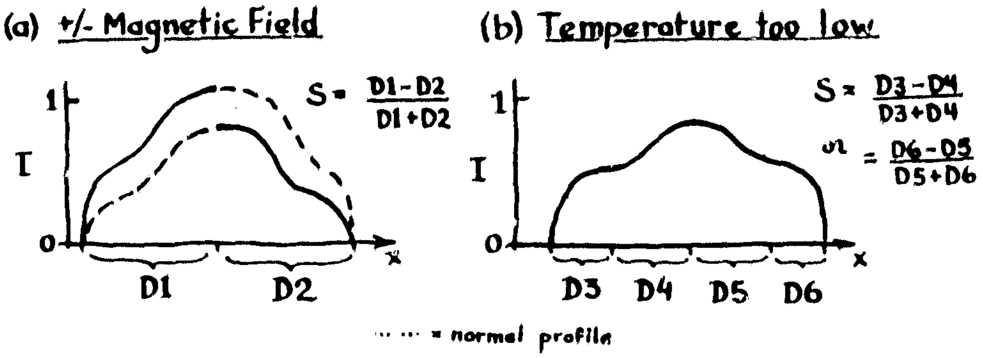

Figure 4.2.2f: Extraction of magnetic and temperature signals from the compressed image.

The temperature signal would be considerably diluted, but it is much stronger to start with and does not need to be measured as frequently or as accurately as the magnetic signal. The effect of the cylindrical lens could probably be simulated electronically by tying together some of the CID lines so that one could rapidly read out the accumulated intensities in complete columns, rather than in individual pixels:

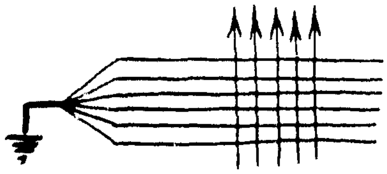

Figure 4.2.2g: Electronic simulation of the integrating effect of a cylindrical lens.

Presumably, however, little real advantage in noise or sensitivity would be gained unless one actually used a smaller physical portion of the detector.

4.2.3. Problem of Compatibility of CID Cameras with Raster Scans

An implicit assumption in the design of the compact magnetograph is that for a given point on the sun one has simultaneous access to the light levels in the various sectors of the detector plane. For a CID operating in a continuously scanning mode, the measurements would clearly not be simultaneous, so that brightness fluctuations between the times at which the right and left-handed polarizations are sampled introduce an additional source of unwanted signal.

In drift scans, the solar image would move by about 8 arc seconds in the 0.5 seconds it takes to readout the existing camera. Although, the important motion is really that occurring between the start and end of the readout of the "active" pixels (which may constitute a much shorter time if $m = 10$), some worry may still persist about light level changes during the readout. It can be minimized by orienting the polarizing mask so that the scan lines will chop between the two circular polarizations as rapidly as possible, rather than reading out all right-handed and then all left-handed pixels. The elimination will not be perfect, however, and even if one used a step scan, pausing at each point, there might still be problems of non-simultaneity associated with seeing and transparency fluctuations between the readouts of the right- and left-handed pixels. Such effects will raise the effective noise level of the CID detection system by an unknown amount.

4.2.4 Photodiode Detectors

Since it turns out that the most efficient mode of operation of the CID is with the smallest possible number of pixels, it seems natural to inquire whether even better performance might not be obtained by using single physically separate detectors for the four detection zones of Figure 2.4a. Likely candidates would be the silicon photodiode devices marketed by United Detector Technology. Physically, these are very similar to the CID elements, but operated in a continuous current rather than a charge integrating/reset mode.* This capability would allow one to avoid entirely the problems cited in the preceding section.

The main drawbacks of the photodiodes appear to be their higher dark currents and noise levels, both the result of their large physical dimensions (compared to a CID pixel). The noise characteristics of these devices are specified by a "noise equivalent power" (NEP - dimensions of joules/$\sqrt{\text{sec}}$).

---

*Because of the very tiny currents generated, the associated electronics would probably actually be operated in an integrating mode where the accumulated charge is digitized to 1 part in 10^4 at the end of each sampling period. However, the digitzations could be performed simultaneously, and in any event, the net effect would be the same as if they were operated in a continuous differential current measurement mode.

According to this definition, the noise in a bandwidth B (Hz) has an amplitude roughly equal to the signal which the device would produce for an input power of:

$$P_{in} \approx NEP \sqrt{B} \tag{4.2.4a}$$

Thus, if the quantum efficiency of the device is Q, and the energy associated with one input photon is ε (joules), the total noise charge accumulated in a sampling time T will be on the order of:

$$\delta n \approx \sqrt{2}\ \frac{NEP}{\varepsilon Q} \sqrt{T} \tag{4.2.4b}$$

since

$$B \approx \frac{1}{T} \tag{4.2.4c}$$

At 6302Å, $\varepsilon = 3.15 \times 10^{-19}$. The square-root of two has been inserted in (4.2.4a) somewhat arbitrarily and possibly erroneously due to uncertainties on the part of the author as to exactly what is meant by the NEP. It is possible that the detectors are slightly less noisy than assumed here.

In any event, if we propose to perform a differential photometric measurement of the sort described by equation 4.2.2d, and if R_o is the basic incident rate in photons per second (of each circular polarization) and R_d is the dark current in charges/second (1 charge = 1.6×10^{-19} coulombs), then it can be shown that the noise level (i.e., the rms uncertainty in the measurement) will be given by:

$$(\delta S)^2 \approx \frac{1}{2R_o^{\,2}T} \left[\frac{R_o}{Q} + \frac{R_d}{Q^2} + 2 \left(\frac{NEP}{\varepsilon}\right)^2 \right] \tag{4.2.4d}$$

This is the equivalent of equation (4.2.2e) for the photodiodes, or other similar devices. In general, the dark current term can be reduced to neglible importance by cooling. The NEP, on the other hand, can be only very slightly reduced.

It should be noted that in equation 4.2.4d it has been assumed that the stated NEP contains only noise contributions in excess of the ultimate photon-counting component. That is, an ideal detector would have NEP = 0. In the more common definition, which we may designate as NEP*, it appears that even a perfect detector would be given a finite value, which is presumably the photon counting contribution at the "minimum detectable" input flux, R_{min} (that is, the one which gives "a signal to noise of 1" or $SS \gtrsim 1$). From equation 4.2.4d $R_{min} = 1/2QT$ for an ideal detector. To explain this entirely by a noise term, we would have to have $NEP^*_{ideal} = e/2Q\sqrt{T}$. This would introduce an arbitrary frequency-dependent term into the definition of NEP* which would not seem to make much sense if it could be avoided.

Of the silicon photodiodes available from UDT, the two most interesting candidates seem to be the PIN Spot/2D and PIN-20A detectors. The former provides two closely spaced rectangular sensors. The latter is a single detector, and is said to provide "the lowest leakage current and lowest noise on the market". Their specifications are as follows:

Table 4.2.4: Characteristics of Commercial Photodiodes

	Area	Q	NEP(joule/sec$^{0.5}$)	R_d(charges/sec @ 25°C)
PIN-Spot/2D (one element)	.032 cm^2	.75	9×10^{-14}	1×10^{10}
PIN-20A	.020 cm^2	.75	6×10^{-15}	3×10^{8}

For an incident rate of $R_0 = 1 \times 10^8$ photons/sec, the PIN-Spot/2D would have to be cooled essentially to its minimum operating temperature of -55° C to make the dark current small compared to the incident rate. The PIN-20A would only need to be cooled slightly. On the assumption that the dark current is negligible, equation 4.2.4d can be used to generate a figure analogous to 4.2.2c showing the expected performance of the photodiodes:

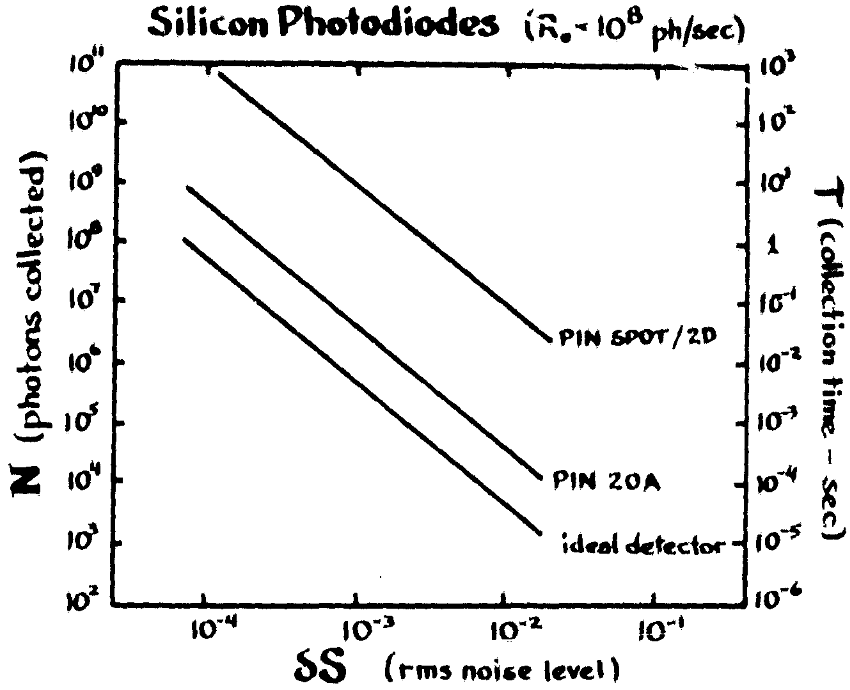

Figure 4.2.4: Noise level as a function of integration time for photodiodes with stated specifications ($R_o = 10^8$ photons/sec). The curves will move closer to the ideal for high R_o and further away for lower R_o.

From the figure, it is evident that the PIN-Spot/2D is considerably inferior to the PIN-20A, and it appears that for weak signals the latter offers essentially the same performance as the idealized CID with a small number (m = 10) of active pixels. That is, a noise level of $\delta S = 5 \times 10^{-4}$ can be achieved with an integration time of slightly under 0.2 sec. The reasons for this coincidence are not fundamental to the detection mechanism. The CID uses a much smaller physical area, and for that small number of pixels has negligible, or at least manageable, readout noise. It is limited mainly by its relatively low quantum efficiency. The photodiode uses a much larger area and is strictly noise-limited.

For coarser measurements, the PIN-20A gains an increasing advantage over the CID. This is because if only a rough measurement is needed, a short integration time (or equivalently, a small number of collected photons) is called for. This condition places the CID in a regime where it has an even lower effective quantum efficiency. The photodiodes supposedly don't suffer from this problem, and are linear over many orders of magnitude.

It should be noted that since the predicted photodiode performance curves are dominated by the NEP term, if the square root of two in equation 4.2.4b were incorrect, the actual integration times might be less by a factor of two. On the other hand, the NEP given in the specifications (Table 4.2.4) is evaluated using a 1 kHz sampling rate, and is likely to underestimate the value which actually applies at the much slower sampling rates considered here (the "flicker effect"). Additional noise would also undoubtedly be introduced by the rather sophisticated electronics which would be needed to measure the extremely tiny ($\approx$ 12 pico-amp) currents which would be generated by the compact magnetograph. Thus it is likely that Figure 4.2.4 gives a somewhat overly optimistic appraisal of the potential performance of the PIN-20A photodiode.

4.2.5 Photomultipliers

For very low light levels, photomultiplier tubes, which have noise equivalent powers as low as 5×10^{-17} joule/sec$^{0.5}$ (for a 1P21 at -55^{0}C), are generally considered to be the best choice. Their main disadvantage is a relatively low quantum efficiency ($\sim$ .1) and an inability to cope with very high count rates. For the compact magnetograph, with fluxes $\lesssim 1 \times 10^{8}$ photons/sec, the maximum count rate would be about 10 MHz which is towards the upper end of the acceptable range.

The noise level in a photomultiplier-based detection system would be governed by the same considerations as for photodiodes (i.e., eqn. 4.2.4d). In the present case, however, it is the photon counting rather than the noise term which supplies the limiting factor. The net result (because of the lower quantum efficiency) is that the predicted performance curve is essentially identical to that of the PIN-20A in Figure 4.2.4.

The problem with using photomultipliers would most likely be the difficulty of finding separate tubes so closely matched that meaningful differential intensity measurements could be made over any extended period. This problem would disappear if the system could be modulated so that the same detector could be used alternately for the two circular polarizations.

4.2.6 Conclusions Regarding Detector Choice

The results of the preceding section suggest that available detectors will fall short by about an order of magnitude of the optimum possible time for detecting the small signals produced by the compact magnetograph. Ideally, a differential measurement good to $\delta S \approx 5 \times 10^{-4}$ would require the collection of only about 2×10^6 photons of each sign, which at a basic light level of about 1×10^8 photons/sec would require only .02 seconds of time. At the same light level, a very low noise photodiode (the PIN-20A) or a photomultiplier would require about 10x as many photons, or 0.2 seconds to make a measurement of the same accuracy. The existing CID camera would also be capable of achieving this noise level in a single 0.5 second readout provided the image is confined to a small portion of the available area.

For purposes of setup and demonstrating the feasibility of the overall concept, it may would sufficient to make a few measurements at a leisurely pace with fixed telescope pointing. Under such circumstances, where efficiency is not a major concern, the CID would seem to be the logical choice. It would permit one to actually examine the ring pattern and to arbitrarily vary the zones used for sampling.

For an actual operational system in which the measurements are to be made in the smallest possible time, discrete photodiodes of very small area would appear to be a more attractive choice. The principal difficulty would be in development of adequate peripheral electronics to deal with the very small signals. If the signal is to be modulated, photomultipliers might also be considered.

4.2.7 Ramifications of Detector Choice on Previously Calculated Integration Times, and on Profile Shaping and Threshold Field

In Section 3, the theoretical integration times required to detect various expected magnetic signals were evaluated on the assumption that one could use an ideal detector, that is one with unit quantum efficiency and zero intrinsic noise. In addition, various filter configurations were suggested which would minimize this time. Those considerations may require some modification depending on the choice of detector.

For an imperfect detector whose performance (like that of the photomultiplier) is limited by photon statistics, rather than by internally-generated noise, the integration time specified by equation 4.2.4d (for a specified noise level) is a simple fixed multiple of that given by equation 3.4.2b. Thus the same optimum will be selected and all previously calculated integration times need simply to be multiplied by the appropriate correction factor.

On the other hand, for a detector (such as the photodiode), whose performance is limited by internal noise, equation 4.2.4c says that

$$T \approx \left(\frac{NEP}{\varepsilon R_o \; \delta S} \right)^2 \qquad (4.2.7)$$

The tradeoff between R_o and signal strength (δS) is slightly different than for the ideal detector, or in other words, the correction factors implied by Figure 4.2.4 are rate-dependent. (Note that the NEP is an equivalent <u>input</u> power, and therefore includes the quantum efficiency of the detector).

To explore the effect of noiseness in the detectors on the optimization of the design the integration times previously provided in Table 3.5.5b and 3.5.6 were re-examined using the noise equation 4.2.4d with the NEP for the PIN-20A photodiode (from Table 4.2.4) and assuming negligible dark current. The calculations are for a signal to noise of 4 at a signal strength corresponding to 1000 gauss with a fill factor of .014. That is, for a quantum efficiency of Q, a basic rate of R_o (in each circular polarization), and a calculated signal strength S, the time will be:

$$T = \frac{8}{QR_o S^2} + \frac{5.8 \times 10^9}{R_o^2 \; S} \qquad (4.2.8)$$

Again, the undisturbed profiles are used, and the possibility of line weakening is ignored.

Table 4.2.7a: Performance Obtainable with Hoya Filters Using PIN-20A Photodiode Detectors (cf. Table 3.5.5b).

Line(Å)	Q	Finesse	f-num	Range	R_o	S_{mag}	T
5250	.60	10	40.3	10- 90 mA	2.04 E8	1.56 E-3	8.41 E-2
5324	.61	8	29.5	10-170 mA	2.50 E8	6.33 E-4	3.63 E-1
6103	.64	10	33.6	0-150 mA	2.79 E8	1.17 E-3	8.72 E-2
6302	.65	15	39.9	0-110 mA	1.78 E8	1.82 E-3	7.61 E-2
8468	.52	15	35.2	10-190 mA	2.75 E8	1.81 E-3	4.05 E-2

Table 4.2.7b: Performance Obtainable with the Hoya Filters and PIN-20A Photodiode Detectors Using One Wing of the Line Only (cf. Table 3.5.6)

Line(Å)	Q	Finesse	Position	R_o	S_{mag}	T
5250	.60	15	50 mA	1.24 E8	3.52 E-3	4.59 E-2
5324	.61	7	110 mA	3.61 E8	6.08 E-4	2.19 E-1
6103	.64	10	80 mA	2.81 E8	1.55 E-3	4.91 E-2
6302	65	15	70 mA	1.88 E8	2.29 E-3	4.38 E-2
8468	.52	15	120 mA	3.03 E8	2.21 E-3	2.33 E-2

It will be observed that under these real-life circumstances the detectors are very hungry for light and are willing to give up signal strength to get it. On the average, the optimum finesse's turn out to be less than half of what formerly appeared to be optimum, and in some cases the effective FWHM of the best filter combination actually exceeds that of the line.

On the average, the integration times required with the PIN-20A photodiodes are found to be 3.5 times longer than those calculated for a perfect detector, which is fairly close to the factor indicated in Figure 4.2.4.

It is also evident that when noisy detectors must be used, the single-wing mode of operation is even more advantageous than before. In the present case, the integration times are reduced, on the average, by a factor of 1.75.

4.3 Calibration of the Detector

4.3.1 Calibration Prior to Use

Whatever detector is selected, it is extremely important that it be well calibrated.

In most magnetographs the signal on a fixed detector is alternated between right and left-hand circular polarizations so that roughly speaking one needs only the capability of measuring fluctuations, and not the capability of measuring absolute light levels. In the compact magnetograph it is proposed to measure the two light levels by means of physically separate detectors, and it is apparent that if differences are to be measured over any significant range of light levels that the relative photometric properties of the two detectors must be very well established. That is, given the reading in one detector, one must be able to anticipate very accurately what the reading should be in the other detector if the same light level were falling on it. Indeed, the prediction has to be at least as good as the expected signal; that is, we would like to be within 1 part in 10^3 or better.

An obvious difficulty in producing such a calibration is that of devising a source in which the overall intensity on the two detectors can be varied with minimal probability of altering the pattern. For example, if we developed a sufficiently uniform source of illumination and then tried to vary the intensity on the two detectors by placing a neutral density filter in front of them, it would not be obvious how much of the observed imbalance could be due to non-uniformities in the filter. Similarly, an ordinary light bulb can be varied in intensity by changing the voltage, but one wonders how uniformly the filament will brighten.

A possible solution would be to use a pinhole aperture illuminated by a laser, as shown in Figure 4.3.1:

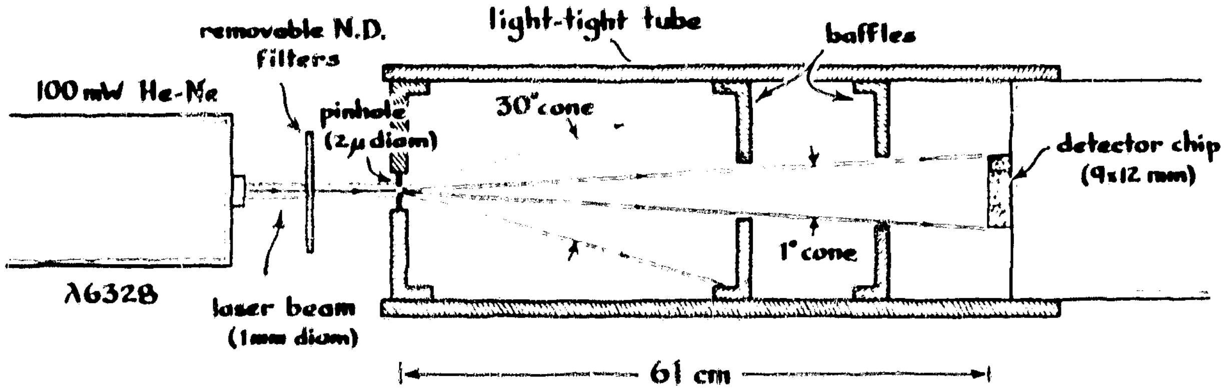

Figure 4.3.1: Possible light source for performing a photometric calibration of detectors.

In general, if the diameter of the pinhole is D, and the distance to the detector is ℓ, then the intensity incident on the detector plane will be given by:

$$\begin{aligned} I &= I_o \left[\frac{2J_1\left(\frac{\pi D \sin r/\ell}{\lambda}\right)}{\frac{\pi D \sin r/\ell}{\lambda}} \right]^2 \\ &= I_o \left[1 - 2.47\ldots\left(\frac{Dr}{\lambda \ell}\right)^2 \right]. \end{aligned} \qquad (4.3.1a)$$

where r is the radial coordinate from the optical axis. For example, for the situation illustrated, the intensity would be uniform to about 0.15% from center to edge.

The light level can be easily varied by introducing neutral density filters. If the incident intensity is I_{inc}, then the intensity in the center of the diffraction pattern is given by:

$$I_o = \frac{.659\ldots\ D^4\ I_{inc}}{\lambda^2\ \ell^2} \qquad (4.3.1b)$$

For a 100 mW laser with a uniform 1 mm diameter beam, the dimensions indicated in the figure would give $I_o = 9.10 \times 10^{-10}$ watts/cm^2. This compares favorably with the 5×10^{-11} watts/cm^2 which would be obtained if the entire 2×10^8 photon/second compact magnetograph image at 6302 were spread over a 9mm diameter (the size of the CID chip), but is considerably less than the intensities which might be obtained if that image were refocussed onto a very small portion of the CID.

While the central axis of the diffraction cone would tend to move with the direction of the input beam, deflections of up to about 1 arc minute would produce less than a 1 x 10^{-4} change in the intensity at any fixed point in the detector. Similarly, lateral motions of the pinhole of up to about .007" would have negligible effect. Thus, the intensity of the image over the entire detector would be varied by inserting density filters in the input beam. Density variations over the dimensions of the pinhole, even if present, would have negligible effect on the image; however, it would be wise the jiggle or rotate the filter a little to make sure that there is not wedging or inhomogeneities in the index of refraction (i.e., phase errors) which would tend to tip the output.

4.3.2 Calibration in Use

It is obviously not practical to calibrate a solar magnetograph in the sense of checking the output for a known test field. In general, "calibration" refers rather to an empirical determination of the average line profile by measuring the Doppler signal corresponding to a known line shift. For the compact magnetograph this kind of calibration would presumably be accomplished by measuring the offset between the east and west limbs at a fixed filter temperature.

For the compact magnetograph calibration is also necessary in the sense of keeping track of the photometric properties of the separate detectors which are used to extract the difference signals. The primary effect of calibration errors will be to shift the zero of the magnetic scale. A fingerprint on one side of the objective, for example, would cause a permanent apparent imbalance between the two circular polarizations. Fortunately, the sun provides its own null signal, since at a resolution of 10 arc seconds large areas of the sun should appear at close to zero field strength. Thus it should be a fairly straightforward matter to shift the magnetic scale by a suitable amount to compensate for the fixed calibration errors. Indeed, ability to pick out visually the "true" zero is, after all, the rationale behind the Leighton technique of displaying "white" and "black" fields against a "gray" background. The only strong requirement would seem to be that the calibration not change significantly during the time it takes to complete a raster scan.

4.4 Temperature Control Requirements

In order to keep the filter assembly properly centered on the solar spectral line it is necessary to maintain it in an actively controlled thermal environment. Typical wavelength shifts, which are a function of the expansion coefficient of the substrate material, are about 36 mÅ/°C according to the proposal.

The precision with which the temperature needs to be controlled is indicated in Figure 4.4a:

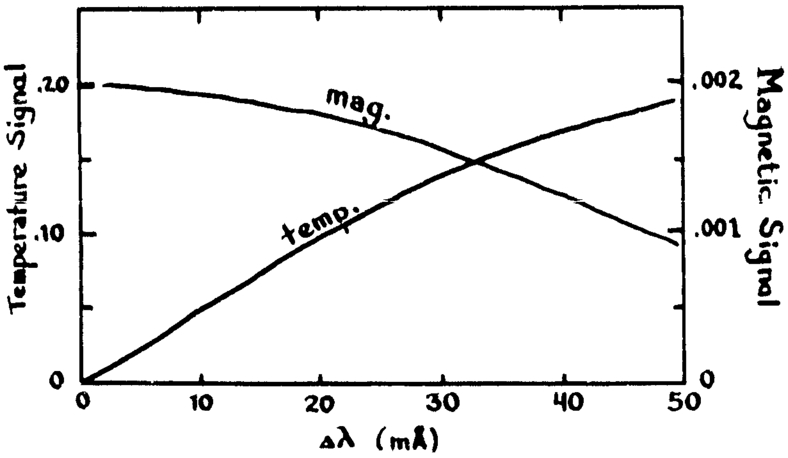

Figure 4.4a: Magnetic and temperature signals for a decentered detection system.

This indicates the magnetic signal (for ~ "5 gauss") calculated for the Hoya filters operated at 6302 using the detection scheme of Figure 2.4a, but allowing the central wavelength to drift by the indicated amount. The assummptions are the same as in Table 3.6b. With no shift, the detectors sample 10 - 90 mÅ in each wing. It is apparent that a shift of as much as 20 mÅ, which would produce a temperature signal of 0.10 (in terms of eqn. 2.4b), would cause negligible deterioration in the magnetic sensitivity. This means that temperature control is only needed to about ± 0.5 °C, and that the signal indicating such an error would be quite easily detectable.

On the other hand, the operating temperature has to be varied to compensate for solar rotation as the instrument is scanned across the sun. This motion corresponds to about ± 1.89 km/sec at the equatorial limbs, and for a rigid rotator, varies linearly with apparent distance from the central meridian. At λ6302 this corresponds to a Doppler shift of ± 40 mÅ, which if uncompensated, would severely weaken the magnetic signals already weakened by geometric effects.

The need for rapid temperature control can be minimized by performing the raster scans along lines parallel to the central meridian, rather than parallel to the equator (as seems to be traditional):

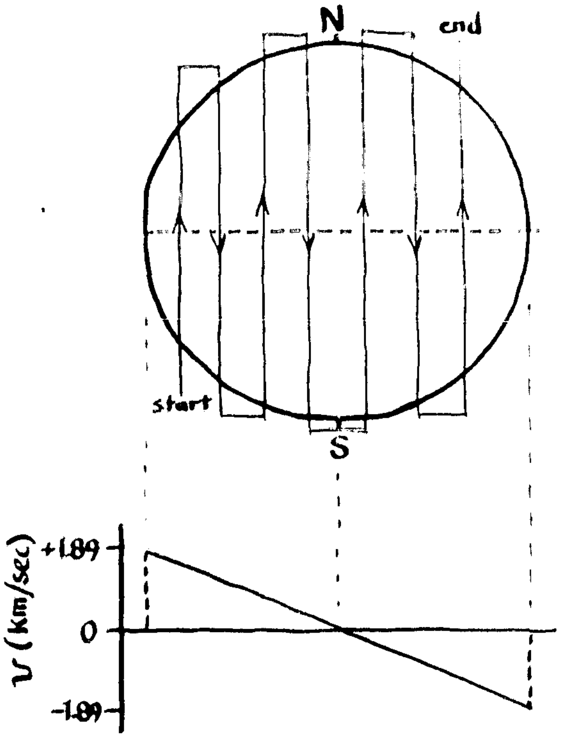

Figure 4.4b: Raster scan pattern to minimize need for temperature adjustment.

Using this pattern, the temperature can be varied slowly and continuously over the time it takes to complete the raster, rather than needing to be completely cycled on each line.

4.5 Requirements on the Uniformity of Bandpass and Temperature over the Aperture of the Filter

The results illustrated in Figure 4.4a apply also, but in a more complicated way, to the losses in sensitivity which occur if the thickness of the filter, or its temperatue are non-uniform over the aperture used by the beam. Roughly speaking, fixed errors of less than about ± 20 mÅ from point to point would have little effect on the sensitivity of the instrument for detecting the changes associated with magnetic fields, but depending on their exact pattern (that is, where they lie with respect to the detection sectors) they could have an extremely large effect on the zero of the magnetic scale.

The same argument applies to the effect of fixed temperature gradients. The problem is that the magnitude of the temperature gradients is likely to change as the controller applies more or less heat, and also, possibly as the brightness of the solar beam (which governs how much heat is dissipated at that point) varies. If we ignore convection, the effects of these gradients can be minimized by taking care that the beam passes through the axis of symmetry. In that case, the (radial) temperature gradients will simply cause a non-linear stretching of the wavelength scale in the detector plane. To first order, this would be interpretted solely as a temperature error, and be rejected from the magnetic signal (see Figures 2.2b and 2.4c).

The problem with convection is that it is likely to cause the temperature to stratify vertically inside the oven, and this would cause a linear gradient to develop in the filter, whose magnitude would vary with the heating. The effect in the detector plane of the temperature being too high on the top and too low on the bottom would be very much like that of the vertical tilt shown in Figure 2.2b (except upside down). Although the magnitude of this effect is likely to be very small, the magnetic signal is also very tiny. To minimize the chance of this being interpretted as a magnetic imbalance, care should be taken that the vertical axis of the polarizing mask is suitably aligned.

4.6 Seeing Problems

A potential difficulty with a magnetograph of the compact Fabry Perot design is that atmospheric inhomogeneities between the instrument and the sun will cause fluctuating differences in the intensity distribution over the objective which could be misinterpreted as magnetic or temperature signals.

To anticipate how large this source of noise might be, one would like to know the rms magnitude of the short-time-period fluctuations in the light level from a 10 arc-sec portion of the sun viewed through a 1" objective. The differential measurement between two closely spaced apertures (as used by the compact magnetograph) should show less fluctuation, but probably not by a great deal.

An upper limit is presumably provided by the observations of shadow bands at solar eclipse. [illegible] These indicate roughly sinusoidal intensity variations of about 5% with a wavelength of 5 cm and a speed of about 10^3 cm/sec. After a time T (seconds), the peak to peak intensity fluctuations over a 2" aperture should be on the order of:

$$\frac{\delta I}{I} \approx \frac{8\times10^{-5}}{T} \qquad (4.6)$$

To reduce this below the desired photometric noise level of $\delta S = 5 \times 10^{-4}$ would take T ~ .2 sec. However, only a small part of the shadow band effect is thought to be due to genuine transparency variations (they probably mostly come from "seeing"). Thus, even though the compact magnetograph could potentially act as a very sensitive probe of atmospheric inhomogeneities it does not seem likely that this will prove a limiting factor.

4.7 Feasibility of a Doppler Mode

The Fabry Perot magnetograph is not particularly well suited for the measurement of solar velocities over prolonged periods because of the confusion between temperature and velocity signals. The spatially and time-varying components of the solar velocity field (5-minute oscillations and supergranulation), are expected to have an amplitude of at most a few tenths of a km/sec when viewed with a 10 arc sec aperture. According to Section 4.4, this would cause shifts of less than 5 mÅ in the position of the line in the detector plane, which in themselves would not be meaningful unless one were confident that the temperature of the filter was stable to considerably better than 0.1°C.

To make useable velocity measurements over any extended time it would therefore be necessary to use a differential signal based on the relative positions of a solar and a telluric line.* Since the nearest telluric line to

---

* [illegible]

6302 is 280 mÅ to the red, this would require increasing the coverage available to the detector from the normal -90 to +90 mÅ up to about -90 to +350 mÅ. This can easily enough be accomplished by lowering the f-number of the beam through the filter (i.e., by using a more divergent beam - cf. Figure 2.2a), but it would be at the expense of a significant loss in magnetic sensitivity. For the coverage range indicated above, only about 40% of the area of the objective would be useable for the magnetic measurement. This means that to achieve a specified noise level the integration times would have to be increased by about 2.5 times (for an ideal detector). For a real detector, the increase would be even greater due to the added importance of the fixed noise terms at low light levels.

Since the solar beam through the filter is expected to have quite small physical dimensions, a possible solution to this problem would be to use a completely separate beam through a neighboring portion of the filter for purposes of temperature control. A suitably tilted and slightly divergent He-Ne laser beam might be used, for example (cf. § 5.3). The success of such a scheme would, of course, depend on the temperature changes being reasonably uniform over the distance separating the beams.

4.8 Electro-Optic Modulators

The possibility of using electro-optic modulators in the design has not been considered up to this point, both because such devices require high voltages, and because they are considered too failure-prone for prolonged periods of unattended operation (as on a long spaceflight).

These failures are primarily associated with the deterioration of the transparent electrodes, and for the compact magnetograph this may not be such a serious objection. At least with a 10 arc sec sampling aperture, the physical size of the light beam is quite small (cf. § 5.4) and if the KDP were placed at that point a device with an open-work metallic grid, or even one with specially-constructed solid electrodes having a small clear aperture in the middle, could be used (the beam passing through a clear point in either case).

There are obviously many advantages to be gained by substituting an electrically modulated crystal for the fixed quarter waveplate (which explains why this procedure has been adopted in virtually every successful groundbased magnetograph). The advantages derive primarily from the fact that the modulator reduces by a factor of two the number of detectors which are required to monitor the magnetic signal. For example, in the design of Figure 5.1, instead of using half the objective so that both circular polarizations can be monitored simultaneously by physically separate detectors, with the KDP the entire objective would be used alternately for the two circular polarizations and only one detector would be needed (the magnetic signal being derived from the AC component of its output).

This reduction greatly alleviates the requirements on the stability of the detectors: instead of having two separate devices which must remain photometrically matched over the length of the complete raster scan (and over the variety of light levels which will be encountered), one has only one device which need not be particularly linear nor stable over much more than the time it takes to make a single measurement.

A more subtle, but possibly equally important advantage, is that one has effectively doubled the intensity of light (photons/sec) available to the detector. As can be seen from Section 4.2.7, if the light level is very low to start with, so that the noise originates primarily in the detector rather than in the intrinsic photon statistics, the signal derived from a single fully illuminated detector will be $\sqrt{2}$ less noisy than that from two partially illuminated ones, allowing measurements to be made in half the integration time.

Finally, by being able to use the full aperture one avoids also the problems (intrinsic to the two-detector designs) of transient non-uniformities (such as shadows, dirt and temperature gradients) being mistaken for magnetic signals.

It should perhaps be noted that by using the KDP one does not give up the possibility (described in Sections 5.5 and 5.6) of still further reducing the integration times by doubling the light level with a polarizing beam-splitter. Although the KDP itself could obviously not be fabricated in the complicated segment quarter waveplate designs of Section 5.5, these patterns can be precisely simulated by using a simple modulated ± quarter-waveplate in conjunction with a suitable fixed, segmented half-waveplate.

5. Suggested Designs

5.1 Basic Two Detector Magnetograph

In the simplest design a simple two element detector is used:

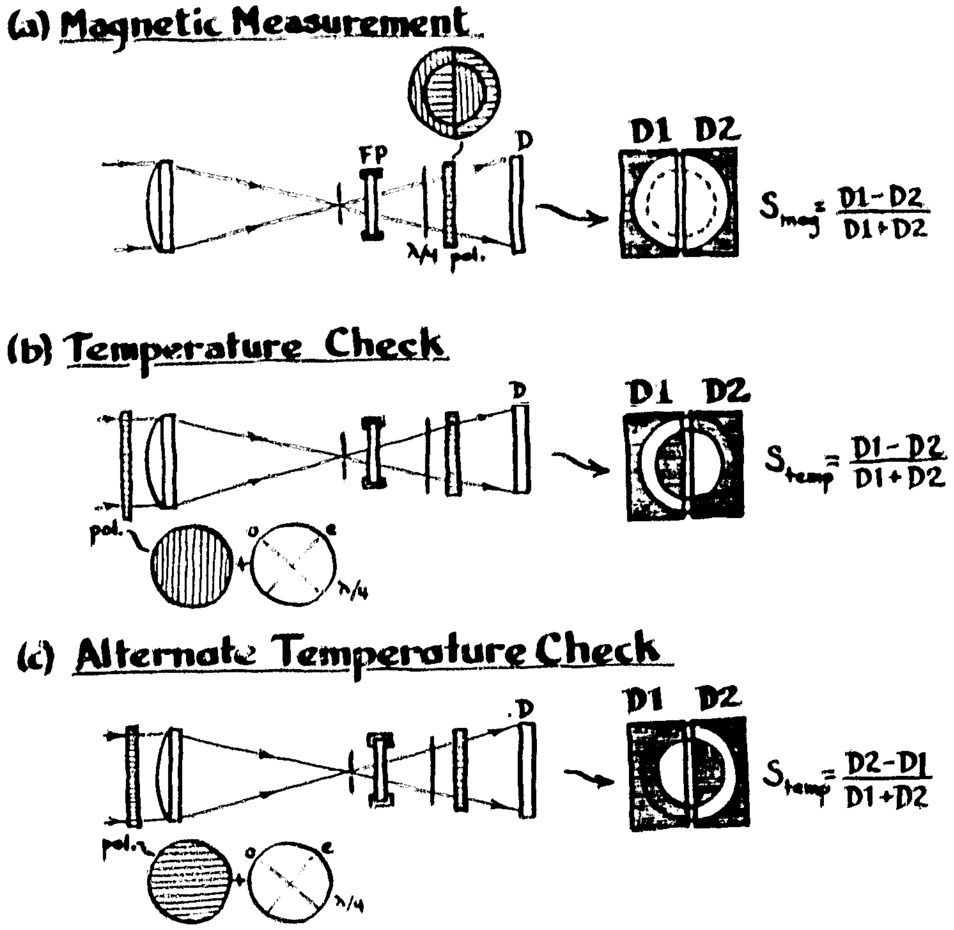

Figure 5.1: A compact magnetograph design using two detectors. The shaded portions of the detectors are those on which no light falls.

A polarizing mask of the variety shown in Figure 2.4b is used. This design provides the optimum trade-off between magnetic signal and detector sensitivity, but sacrifices the capability for continuous temperature monitoring.

To check the temperature, an auxilliary circular polarizer would be inserted in front of the objective lens in either of two configurations

(Figure 5.1, parts b&c). Acting in conjunction with the permanent analyzer, this would block off half of the light to each detector, and permit the temperature measurement to be made using the same electronics as for the magnetic measurement, as shown.

5.2 Four Detector Designs

In order to simultaneously monitor the magnetic and the temperature signals, that is, in order to simultaneously extract two independent difference signals, it is necessary to have at least four detectors. Figure 5.2 shows two options involving four detectors:

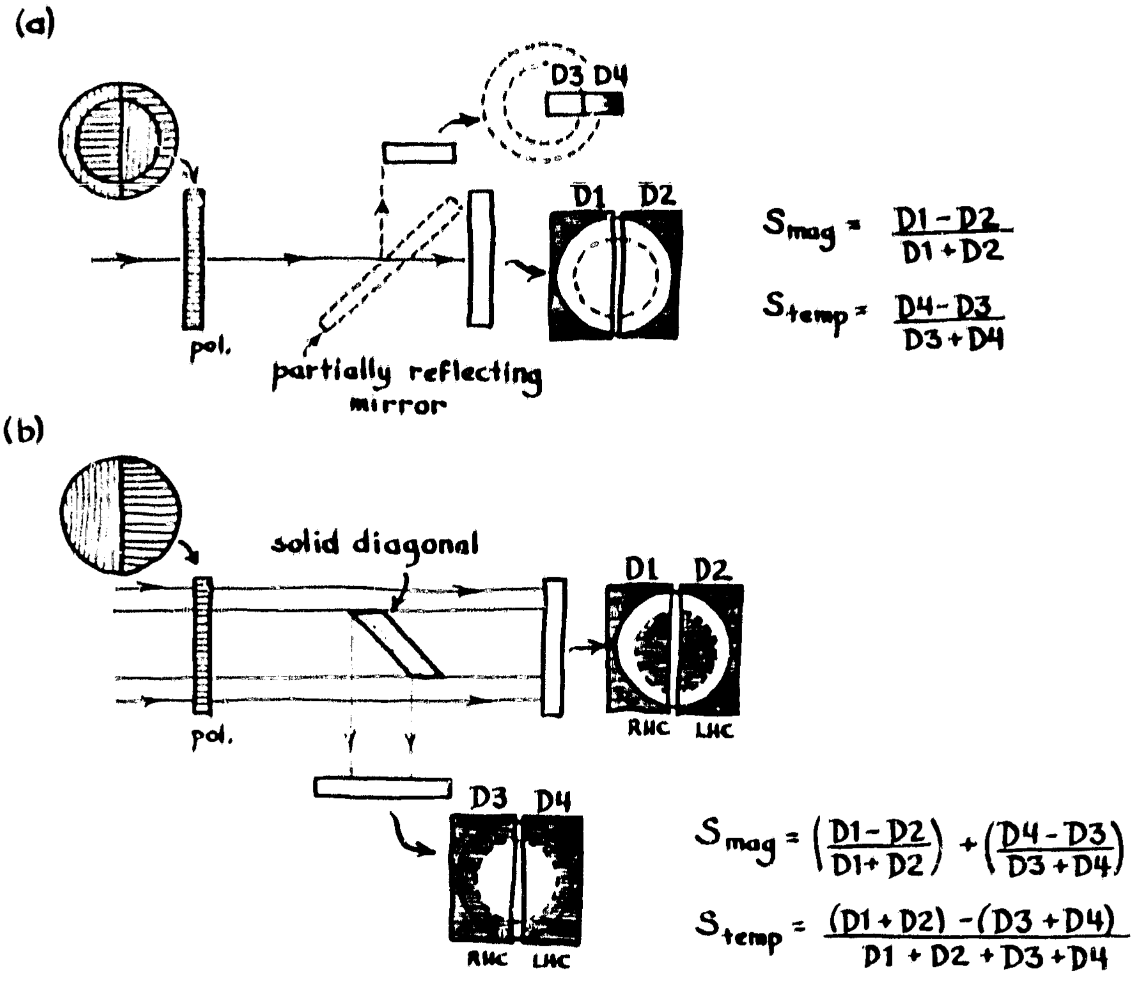

Figure 5.2: Designs employing four detectors. Again, the shaded portions of the detectors are those on which no light falls.

In the first design (Figure 5.2a), which is a simple variation of Figure 5.1, a small amount of the light is stolen to permit the temperature measurement. It is based on the observation that the temperature signal is much larger, and it does not needed to be evaluated as frequently. The two small detectors D3 and D4 obviously do not make the most efficient use of the reflected light, and a more elaborate scheme (involving a diagonal mirror as in Figure 5.2b) could be used if necesssary.

To achieve any fixed noise level, the configuration of Figure 5.2a would require a longer integration time than that of Figure 5.1 in direct proportion to the amount of light lost by reflection and absorption (i.e., the effective transmission or quantum efficiency is lower).

In the second design (Figure 5.2b) a diagonal mirror is used to physically separate the inner and outer parts of the ring plane image. Either version of the polarizing mask could be used, but that of Figure 2.4.1 was chosen for clarity. The design suffers from a relatively inefficient use of the rectangular detectors which is likely to increase the noise and dark current problems. Since the two independent measurements of the field strength can be averaged together, the individual measurements can be a factor of $\sqrt{2}$ coarser than required in design 5.1, however, the light level is only half as much, and for a noise-limited photodiode, according to equation 4.2.7, the intrinsic noise level would be twice as great. The upshot is that if the same diodes are used in both cases, twice as long an integration time would be required to achieve the same noise level. On the other hand, if a photon-counting-limited detector were used, no increase in integration time would be needed.

5.3 A Design Using Only One Wing

As indicated in Section 3.5.6, and again in Section 4.2.7, there is for any line and field strength a reasonable advantage (a factor of 1.5 - 1.75 in integration time) to be gained by operating the magnetograph in one wing only. Figure 5.3 suggests one possible design in which this is done:

C - 2

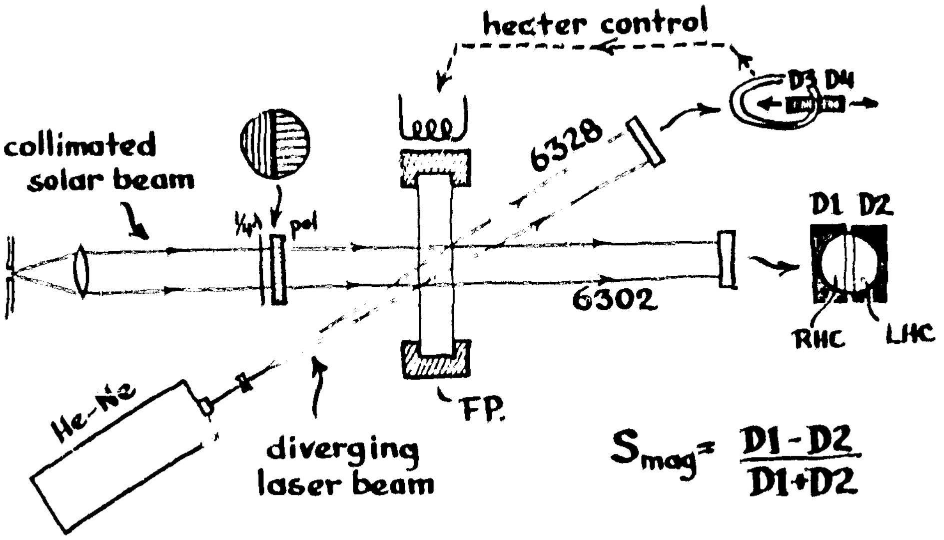

Figure 5.3: A design using the filter in a single wing of the solar line. The laser reference source is added for temperature control.

Since two detectors are used for the magnetic signal, the advantage in integration time would be relative to design 5.1, which is already the most efficient of those suggested so far. The disadvantage of the design is that it cannot be used in a Doppler mode and therefore needs some auxilliary means of temperature control. In the one suggested, a slightly divergent laser beam is used. Since it is unlikely that there will be a bandpass exactly at the wavelength of the laser light when the filter temperature is correct for the solar line, the laser beam is passed through at an angle. The transmission pattern will then be a somewhat flattened annulus whose diameter varies with the temperature and whose width depends on the FWHM of the filter. The laser light annulus is monitored by the detectors D3 and D4 which are connected by a servo mechanism to the temperature controller. The operating temperature is varied by shifting the lateral position of D3 and D4. The temperature control requirements are similar to those in the full ring plane mode (Section 4.4). An error of 20 mÅ would decrease the magnetic signal by about 15%. The problem is that one would need to have a table giving the operating position for each point on the Sun.

When using a single wing there should be a slight additional advantage to using the blue one, since the absorption core from the undisturbed photosphere will be shifted in that direction relative to the profile of the magnetic features. Thus, in the blue wing a lower background level will be found at the point of maximum magnetic modulation.

If the laser idea is unacceptable, a modification is possible (cf. Section 5.6) in which a segmented quarter-waveplate is placed over the objective and a polarizing prism is used to produce two appropriately skewed but individually collimated beams which could be passed through the Fabry Perot at slightly different angles, one corresponding to the red wing, and the other to the blue. Each transmitted beam could then be sampled in the fashion indicated in Figure 5.3 and they would provide independent estimates of the magnetic field. Temperature information could be extracted from the difference in the two total intensities, in the same manner as indicated in Figure 5.6.

5.4 Clarification of the Designs

5.4.1 What are the Detectors?

As indicated in Section 4.2 there are a number of possibilities for what the detectors might be, and the fact that they happen to have been represented by two neighboring rectangular areas does not mean to imply that the PIN-Spot/2D detector has been chosen. Figure 5.4.1a illustrates a number of ways in which combinations of photodiodes or photomultipliers could be used to equivalently sample the detection sectors:

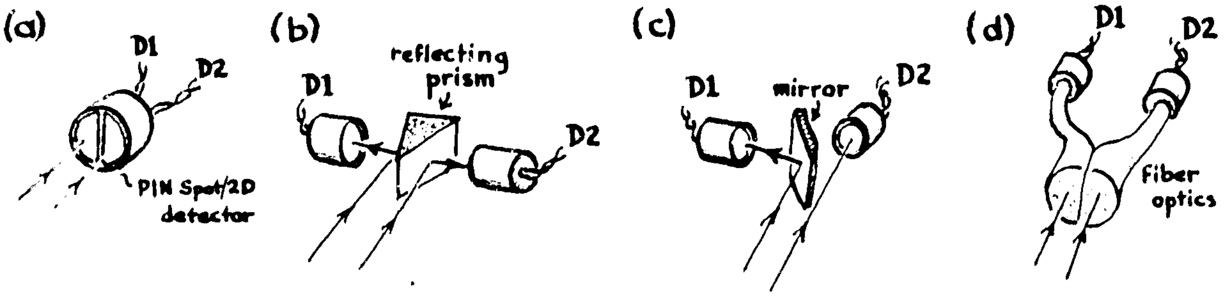

Figure 5.4.1a: Four practical possibilities for the detector pairs.

They could equally well be portions of the CID image plane, either obtained by software by summing over the appropriate pixels, or by a hardware modification:

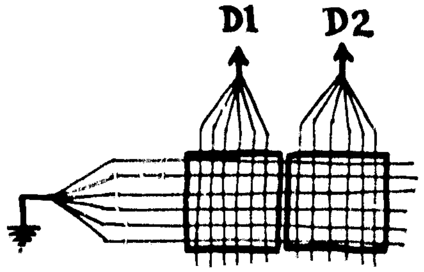

Figure 5.4.1b: An electronic modification of the CID to obtain a detector pair.

5.4.2 How Large are They?

The figures are also somewhat unclear in that they seem to show the detectors as being about the same size as the objective lens. In fact, the actual physical dimensions are likely to be extremely small (cf. Table 4.2.4 and Figure 4.2.2d). For example, to provide a scale one might note that for a 2" objective and an f/45 beam the actual size of the 10 arc second field stop would be about 0.1 mm. The ring plane image will be larger, of course, depending on how far back is is placed. If too large, it can be reduced down to the size of the detectors by means of an additional converging lens. On the other hand, it is desireable for the polarization analyzer to really be of reasonable size, so that it can be easily fabricated. This can be accomplished by placing it in a more appropriate position (such as in front of the objective), or by adding even more lenses.

5.5 Reciprocity Between Polaroids and Waveplates

For purposes of clarity, in all the figures the polarization analyzer has been shown as consisting of the combination of a single simple quarter waveplate and a segmented polaroid. While this is much easier to draw, this configuration is optically completely equivalent to a segmented quarter waveplate followed by a single simple polaroid:

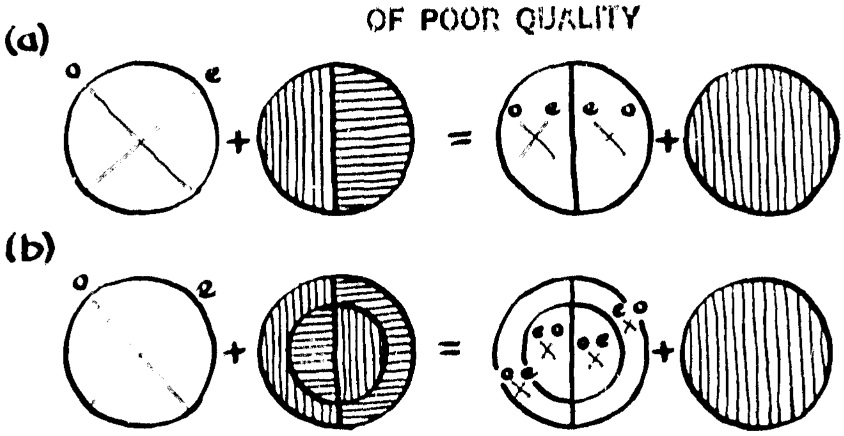

Figure 5.5: Demonstration of reciprocity between polaroids and quarter-waveplates. The configurations on right and left are optically equivalent.

5.6 A Method for Doubling the Light Level

In the designs of Sections 5.1 thru 5.3 half of the light incident on the objective is lost by absorption in the polaroid element of the polarization analyzer. If we use the concept of Section 5.5, that element could as easily as not be a single simple sheet of linear polaroid; and if that is the case it could equally well be a polarizing beam splitter, in which case both the transmitted and the reflected beams would provide complementary and equally useable polarized ring-plane images. Figure 5.6 indicates how this modification could be applied to design 5.1, in which the simple polaroid has been replaced by a segmented quarter-waveplate of the configuration shown in Figure 5.5b cemented to a suitably oriented polarizing beamsplitter.

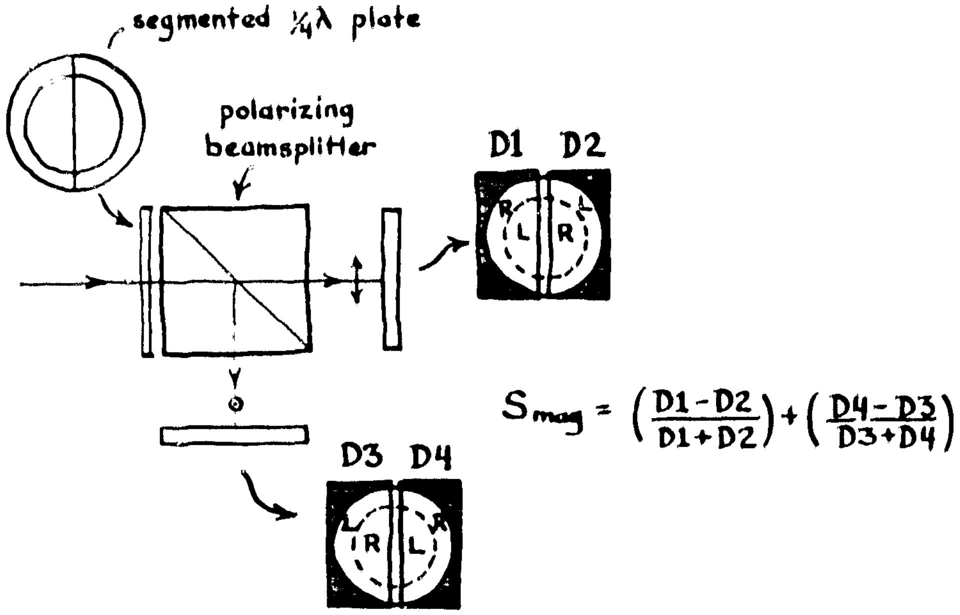

Figure 5.6: Design 5.1 modified to permit dual, simultaneous focal planes.

If there are no losses in the beamsplitter, the noiseness of the averaged measurement would be $\sqrt{2}$ better than that for either focal plane separately, which means that the integration time could be reduced by a factor of 2. If the detectors were of the noise-limited variety governed by equation 4.2.7, and if it were possible optically to invert and superimpose the two focal plane images on the same detector, so that the intensity as well as the light level is increased by a factor of 2, then an even greater improvement in integration time could be realized (up to a factor of 4).

A further advantage of the beamsplit design is that erroneous signals due to non-uniformities over the aperture (shadowing, temperature gradients, fingerprints and atmospheric effects) will tend to appear in the two channels with opposite signs, and therefore cancel in the average.

6. Conclusions

1. The basic outlook for the success of a compact Fabry Perot magnetograph is favorable.

2. Although currently referred to as a "telecentric" system, the only corrector lens which is likely to be needed is the one to re-image the objective, and that only in cases where (to accomodate the detectors) it is desired to have a final "ring plane" image smaller than, or comparable in size to the field stop (§ 2.3).

3. Of the spectral lines which might be used in the visible, λ6302 seems to be about as good as any, and much better than some which have been used successfully in the past (λ5324). The only better lines, at least among the simple Zeeman triplets, seem to be in the infra-red (§§ 3.5 & 4.2.7).

4. Efforts to supress the filter wings help slightly in improving the magnetic response; however, at λ6302, for a given signal to noise, the existing filter pair is already within 2.8X of the ultimate integration time which could be achieved with a perfectly square bandpass. The Hoya filters, if successful and combined incoherently would be within 1.6X of it (finesse = 20). If combined coherently they would presumably be slightly closer still (§ 3.5.3).

5. If the position of the line center must be monitored to maintain temperature control, then at 6302 the best magnetic response can be obtained by having the objective lens (and hence the ring plane "image") correspond to a wavelength range of approximately ± 90 mÅ about line center, which dictates a beam of about f/45 through the filter. Portions of the objective lens transmitting light outside this band (and also within ± 10 mÅ of line center) are counter-productive, and would be rejected at the detector, if present (§ 3.5.2).

6. If the temperature can be monitored separately, the f-number could be increased (i.e. the beam made more parallel) so the whole objective would be used near the point of maximum sensitivity in one wing of the line. This would reduce the integration times required for a fixed signal-to-noise by about a factor of 1.5 - 1.8 (§§ 3.5.6 and 4.2.7).

7. On the other hand, it might for some purposes by desireable to decrease the f-number (i.e. make the beam more divergent) so that one of the

nearby telluric lines could be used as an absolute velocity reference. This would require a minimum spectral range of about 400 mA, which would reduce the light available for magnetic measurements and increase the integration times by a factor of 2 to 5, depending on the detectors (§ 4.7). A better way to make velocity measurements would be to use a separate temperature monitoring system (§§ 4.7 and 5.3).

8. The major source of uncertainties regarding the predicted performance of the instrument are (a) knowledge of the true weak field configuration on the sun; and (b) uncertainties regarding the behavior of the spectral lines in the unresolved magnetic elements (§§ 3.1 and 3.5.5).

9. Nonetheless, it is clear that the basic problem is not so much what is or how to improve the expected signal, but rather, how to efficiently sample and process it. At 6302, the expected magnetic signal corresponding to the lowest contours on the Mount Wilson daily magnetograms ("5 gaus") is about 2×10^{-3} (Table 3.5.3b). We would like to be able to detect this with a signal to noise of 4, that is, with a noise level of about 5×10^{-4} (§ 3.4.2). With a 2 inch aperture, a 10 arc sec sampling area, and optmistic assumptions about the obtainable atmospheric and optical transmissions (§ 3.4.3) we would expect to have, in the optimum ring-plane mode, a light level of about 1×10^{8} photons/sec for each circular polarization (using half of the objective). With an ideal detector, the desired noise level could be reached in about .02 seconds (Table 3.5.3b).

10. Actual detectors will be limited by quantum efficiency and noise. If the detector is in a quantum efficiency (photon statistic) limited mode, the integration times required will be in (inverse) proportion to the light level. In the noise limited regime (very low light levels), the integration times are (inversely) proportional to the <u>square</u> of the light level. The behavior of the CID is even more complicated because the effective quantum efficiency depends on the charge level. In general, the best results, both from the standpoint of noise and dark current will be achieved by using detectors of the smallest possible physical area. For available detectors, even if the design is modified towards higher light levels at the expense of signal strength, the best achievable integration times are about an order of magnitude larger than the ultimate ones (§ 4.2).

11. In general, except possibly for purposes of set-up and demonstration, a complete ring-plane detection system would not be required. By appropriate choice of the polarization analyzing mask, only two simple detectors would be required to measure longitudinal magnetic field strengths, and four to extract both temperature and magnetic information (§ 2.4 and § 5).

12. One project of modest scientific interest which could be performed using the basic compact magnetograph with a full ring-plane configuration and CID detector would be the simultaneous measurement of the strength of circular polarization throughout a line profile; which would require a much longer integration time and/or larger aperture. If the sampling area is sufficiently small, the shape of the magnetically disturbed profile can be inferred. Even for large sampling areas, regions in which the majority of the field is above about 1500 gauss would show a distinctive signature. It is difficult to see, however, how these results would improve over those which could be obtained by the microdensitometry of photographic spectra obtained simultaneously in the two circular polarization.

13. The temperature-monitoring problems do not seem to be as severe as might be imaged. At $\lambda 6302$, signals of as large as $\sim 10\%$ ($\approx 0.5^{\circ}$C) could be allowed to develop without noticeably affecting the magnetic sensitivity (§ 4.4).

14. Because of the intensity-dependence of the relative detector noise levels, not all focal plane configurations are equivalent. To achieve the optimum integration time, care should be taken to make the most efficient possible use of the available light, and to minimize the number of detectors, particularly if photodiodes are used (§ 5).

15. The introduction of a KDP crystal to modulate the magnetic signal would offer many potential advantages, both in terms of reducing the number and complexity of the detectors, and in alleviating the possibility of extraneous imbalances. The disadvantages are minimal, and it would seem that this option should be reconsidered (§ 4.8).

16. In all cases, the efficiency can be improved by substituting polarizing beam-splitters for the polaroid elements. In effect, two independent focal planes are created, the results from which can be averaged (§ 5.6).

17. If spatial resolution is not a primary concern, the dynamic range of the measurements (for a given integration time) can be increased considerably if a larger sampling aperture is used, particularly for photodiode detectors (§ 3.6). An increase in the size of the objective would have a similar effect.

APPENDIX: Detector Characteristics

ORIGINAL PAGE IS
OF POOR QUALITY

CID Characteristics

From Richard S. Aikens (1980): "A Large CID for Use in Astronomy," AURA Engineering Technical Report #66 (KPNO).

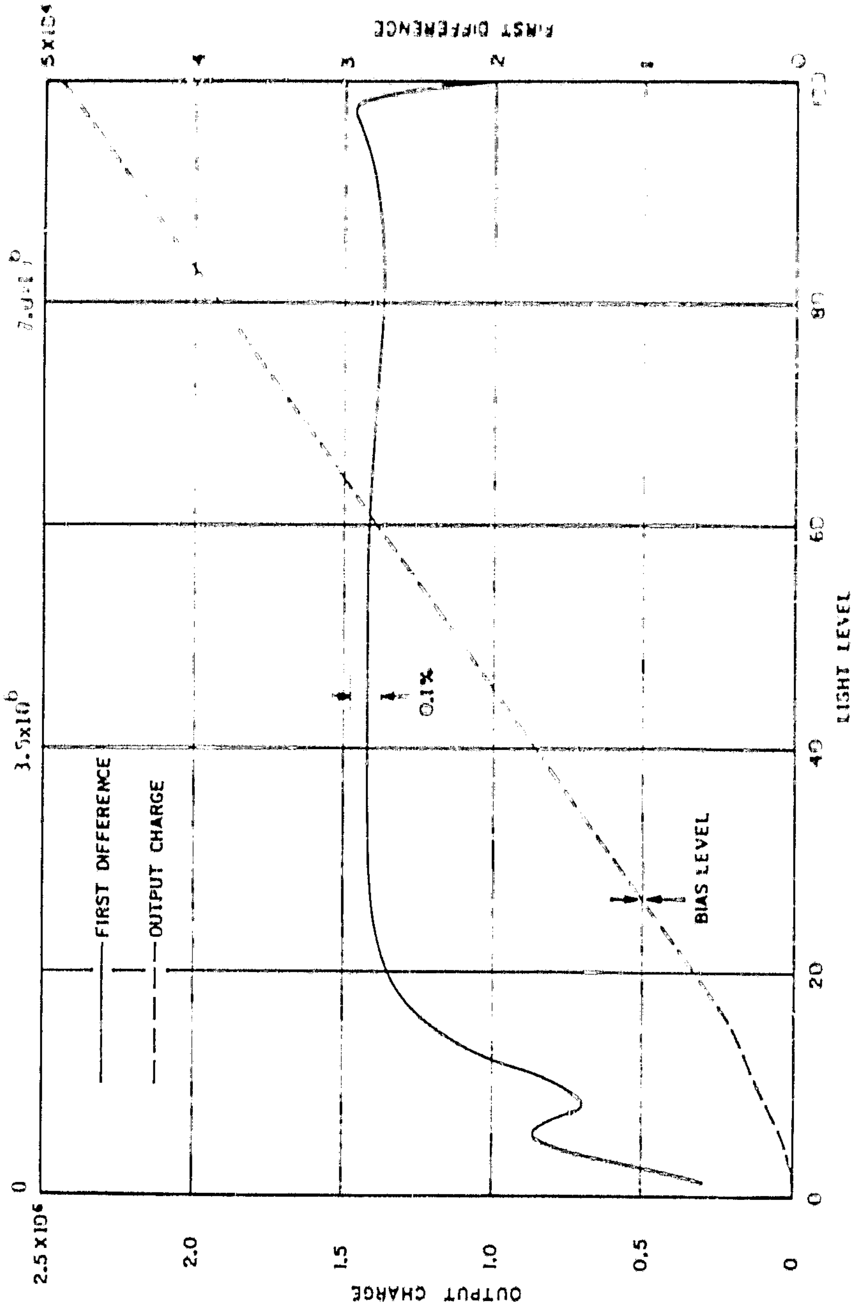

CID LINEARITY DATA

ORIGINAL PAGE IS
OF POOR QUALITY

POSITION SENSING DETECTORS
PIN Spot/2D, Spot/4D

UNITED DETECTOR TECHNOLOGY, INC.

UDT's "Spot" series position sensors are bi-cell or quadrant detectors ideally suited for a wide range of nulling and centering applications.

The devices consist of two or four discrete elements on a single substrate with an active output lead from each element. When a light beam is centered on the detector (null or center position is the intersection of active elements) output current from each quadrant is equal. As the beam moves, current imbalance indicates off-center position. These devices exhibit excellent stability over time and temperature, high responsivity and fast response times necessary for pulse operation.

The PIN-Spot/2D is a single axis position sensor with two discrete elements. The PIN-Spot/4D quadrant detector is ideal for systems allowing light movement in two axes.

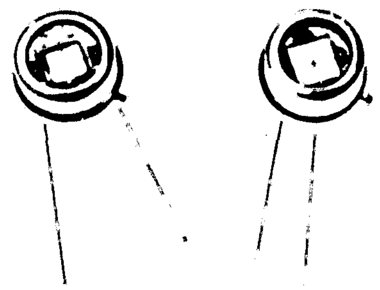

FEATURES

- Broad frequency response
- Fast rise time
- Low capacitance
- High accuracy, long term stability of null position
- Easy hookup

APPLICATIONS

- Lens manufacturing
- Feedback control systems
- Guidance systems
- Laser alignment
- Machine tool alignment
- Targeting
- Process machinery alignment

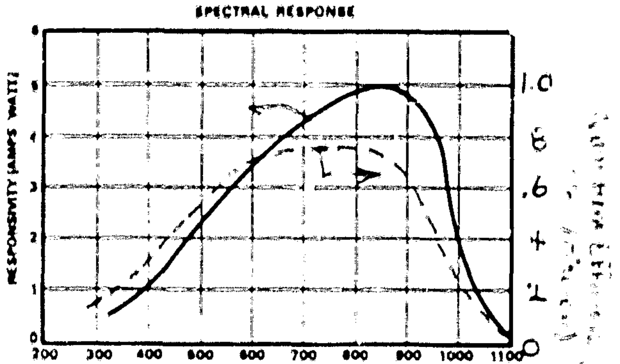

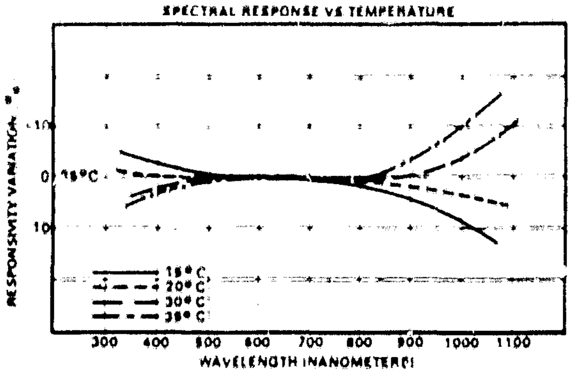

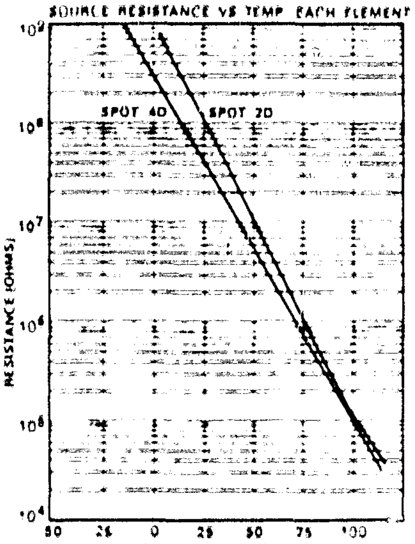

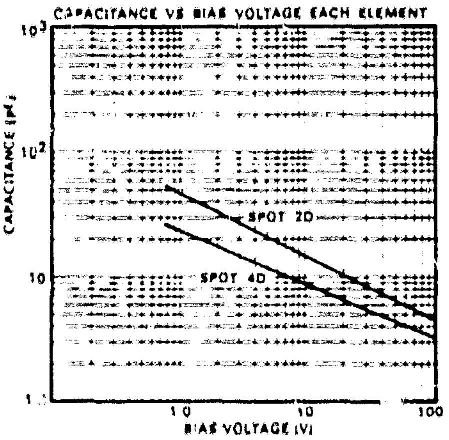

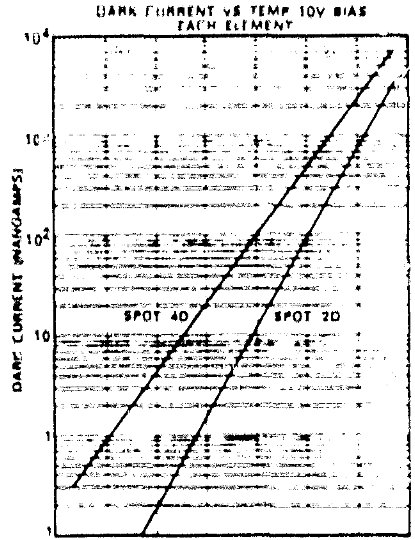

ORIGINAL PAGE IS
OF POOR QUALITY

ELECTRICAL CHARACTERISTICS

PARAMETER AND (UNITS)		PIN-Spot/2D MIN	PIN-Spot/2D TYP	PIN-Spot/2D MAX	PIN-Spot/4D MIN	PIN-Spot/4D TYP	PIN-Spot/4D MAX
Recommended Mode of Operation			Photovoltaic/Photoconductive			Photovoltaic/Photoconductive	
Spectral Range @ 5% Peak (nm)			350 - 1100			350 - 1100	
Responsivity at Peak λ (amps/watt)		0.4	0.5	–	0.4	0.5	–
Uniformity of Response (with 1 mm spot dia)		–	±2%	±5%	–	±2%	±5%
Dark Current per element (μa)	@ 10V Bias	–	0.002	0.05	–	0.002	0.05
	@ 50V Bias	–	0.006	0.15	–	0.006	0.15
Source Resistance per element (MΩ)		–	60	–	–	70	–
Breakdown Voltage @ 10 μa (volts)		50	100	–	50	100	–
Capacitance per element (pF)	@ 0V Bias	–	54	81	–	29	44
	@ 10V Bias	–	15	22	–	7	10
	@ 50V Bias	–	6.7	10	–	4	6
Rise Time at 632.8 nm 10% - 90% (ns)		–	–	–	–	–	–
	@ 10V Bias	–	10.0	–		10	–
	@ 50V Bias	–	10.0	–	–	10	–
Fall Time at 632.8 nm 90% - 10% (ns)		–	–	–	–	–	–
	@ 10V Bias	–	10.0	–	–	10	–
	@ 50V Bias	–	10.0	–	–	10	–
Frequency Response at 632.8 nm into 50Ω Load (MHz)		–	–	–	–	–	
	@ 10V Bias	–	35	–	–	35	–
	@ 50V Bias	–	35	–	–	35	–
Max. Output for 10% Linearity (ma)	@ 0V Bias	–	0.2	–	–	0.5	–
	@ 10V Bias	–	0.25	–	–	1.0	–
NEP @ Peak λ, 1 kHz, 10V (w/Hz½)		–	9×10^{-14}	–	–	9×10^{-14}	–
Noise Current (rms amp/Hz½) @ 1 kHz	@ 0V Bias	–	2×10^{-14}	–	–	2×10^{-14}	–
	@ 10V Bias	–	3×10^{-14}	–	–	3×10^{-14}	–
	@ 50V Bias	–	5×10^{-14}	–	–	5×10^{-14}	–
Forward Resistance (Ω)		–	45	–	–	55	–

MECHANICAL SPECIFICATIONS

SPECIFICATION	PIN-Spot/2D	PIN-Spot/4D
Active Area/Element		
Area (cm²)	0.032	0.016
Dimensions (in.)	0.05x0.1	0.05x0.05
Package		
Type	TO-5	TO-5
Window	Glass	Glass
Field of View Full Angle	96⁰	96⁰
Temperature Range		
Operating (⁰C)	-55 to +125	-55 to +125
Storage (⁰C)	-55 to +125	-55 to +125

OUTLINE DIMENSIONS

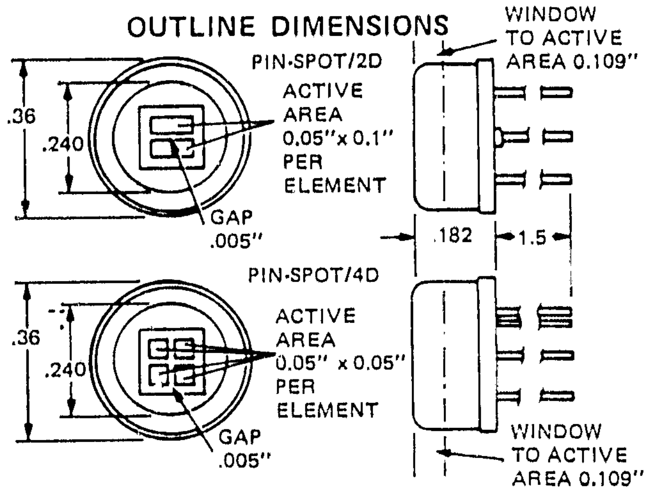

SCHEMATIC DIAGRAMS

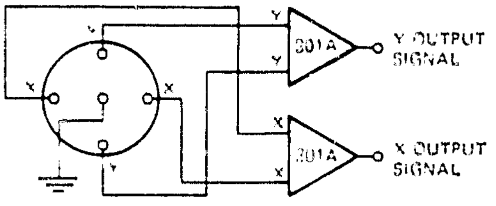

TYPICAL CONNECTIONS FOR PIN-SPOT/4D
TO MODIFIED UDT 301A AMPLIFIER*

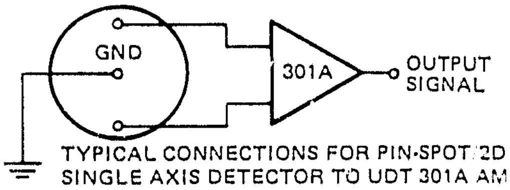

TYPICAL CONNECTIONS FOR PIN-SPOT/2D
SINGLE AXIS DETECTOR TO UDT 301A AMPLIFIER

*AMPLIFIER BIAS POLARITY MUST BE CHANGED

SPECIFICATIONS SUBJECT TO CHANGE WITHOUT NOTICE

D-017-0777

UNITED DETECTOR TECHNOLOGY, INC.

2644 30TH STREET, SANTA MONICA, CA 90405 ■ TELEPHONE (213) 396-3175 ■ TELEX 65-2413

Data Sheet No. 9F010

LOW NOISE SER

UNITED DETECTOR TECHNOLOGY INC.

PIN SILICON PHOTODIODE ULTRA LOW DARK CURRENT ULTRA LOW NOISE

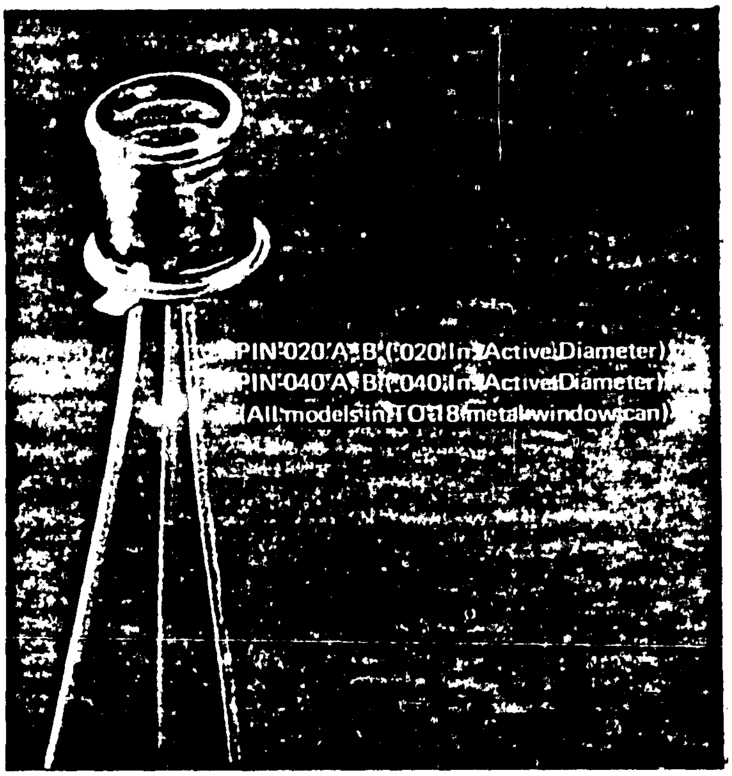

PIN-020 A, B (.020 In. Active Diameter)
PIN-040 A, B (.040 In. Active Diameter)
(All models in TO-18 metal window can)

Description

The UDT Low Noise Series (Model 020 A, B and Model 040A, B) of PIN photodiodes offer the lowest leakage current and lowest noise on the market. They are planar passivated and hermetically sealed. The detector active element is electrically isolated from the case.

The quantum detection efficiency is constant over ten decades of light intensity, providing a linear output current signal with input light level. The speed of response is less than 5 nanoseconds, allowing the observation of laser pulses of a few nanoseconds. The frequency response extends from dc to over 100 MHz. Both biased (photoconductive) and unbiased (photovoltaic) operation give excellent results with this device.

UNIQUE FEATURES

- 50×10^{-12} A leakage (PIN-020A)
- 200×10^{-12} A leakage (PIN-040A)
- 6×10^{-15} W N.E.P. (PIN-020A)
- Planar Passivated
- Hermetically Sealed TO-18 Metal Can
- Photodiode Isolated from Case

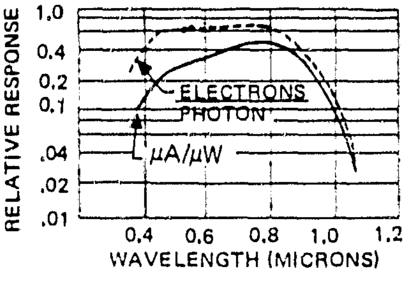

Applications

Because of their unrivaled low leakage current and low noise, these devices are especially suited to low light level detection systems. They are currently being used in star trackers, earth resources scanners, and spectrophotometers.

Specials

The low leakage characteristics of these devices can be built into many custom array geometries by UDT.

PIN SILICON PHOTODIODE ULTRA LOW DARK CURRENT ULTRA LOW NOISE

UNITED DETECTOR TECHNOLOGY, INC.

2644 30TH STREET, SANTA MONICA, CA 90405 • TELEPHONE (213) 450-8585 • TELEX 65-2413

ORIGINAL PAGE IS
OF POOR QUALITY

ELECTRICAL AND OPTICAL CHARACTERISTICS

	Pin-020A			Pin-020B			Pin-040A			Pin-040B			Units
Dark Current	Min	Typ	Max	Min	Typ	Max	Min	Typ	Max	Min	Typ	Max	
–5 V		50	150			800		200	400			4000	pA
–10 V		75	250			1000		300	600			6000	pA
Responsivity Peak		.42			.42			.42			.42		A/W
N.E.P. 1000 c.p.s. Center 1 c.p.s. Bandwidth 1-5 V Bias 8500 Å		6×10^{-15}			2×10^{-14}			10^{-14}			9×10^{-14}		W
Capacity													
–5 V		5			5			20			20		pF
–10 V		4			4			16			16		pF
–20 V		3			3			12			12		pF
Response Time 20 V, 50 Ω			5			5			5			5	ns
Maximum Steady Reverse Voltage			25			25			25			25	V
Active Diameter		.020			.020			.040			.040		in.
Active Area		2×10^{-3}			2×10^{-3}			8×10^{-3}			8×10^{-3}		cm^2

MECHANICAL DETAIL

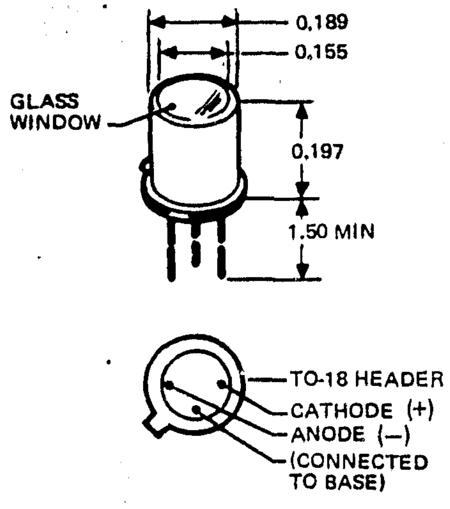

EQUIVALENT CIRCUIT

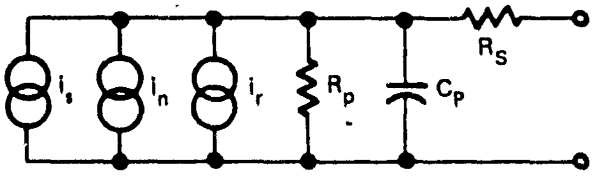

i_s = Signal current ≈ 0.5 μA/μW

i_n = Shot noise current

$< 3 \times 10^{-15}$ A/Hz$^{1/2}$ PIN-020A

$< 10^{-14}$ A/HZ$^{1/2}$ PIN-040A

i_r = Dark current

R_p = $\approx 10^{11}\ \Omega$

R_S = $< 50\ \Omega$

UNITED DETECTOR TECHNOLOGY, INC.

APPENDIX

Line and Magnetograph Characteristics

1. Unpolarized 5250 Profiles

(a) J. Harvey & W.C. Livingston (1969): "Magnetograph Measurements with Temperature Sensitive Lines", Solar Phys. 10, 283.

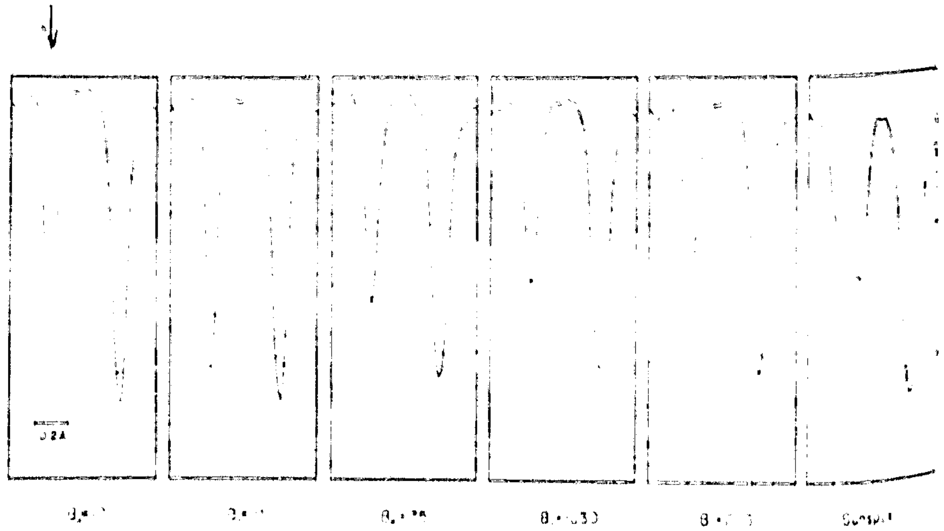

Fig. 2. Double-pass photoelectric scans of 5250.22 Å (left) and 5250.65 Å (right) with one arc second resolution in regions with various longitudinal magnetic-field strengths as measured with the 5373.7 Å line and given in units of gauss. It is very likely that the 5373.7 Å line is temperature sensitive and therefore the magnetic fields are probably underestimated by a factor of two or more

(b) G.A. Chapman & N.R. Sheeley, Jr. (1977): "An Improved Measurement of a Spectrogram of a 'Gap'", Solar Phys. 51, 61.

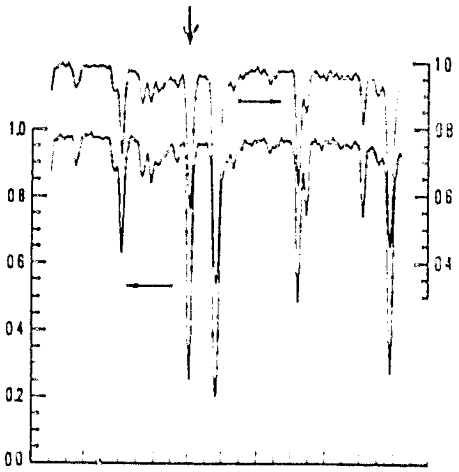

Fig. 2. The spectrum of the quiet Sun and the 'gap' covering the region from 5237 Å to 5253 Å in three parts. The facular spectrum is shifted upwards by 0.2 in I/I_c for clarity. The wavelength scale is 0.5614 Å between each large tick mark on the abscissa and runs left to right on each. The arrows indicate the correct scale for that portion of the spectrum.

ORIGINAL PAGE IS
OF POOR QUALITY

2. Inferred Single-Component Profile from Harvey and Livingston (1969) (based on a weak-field interpretation.)

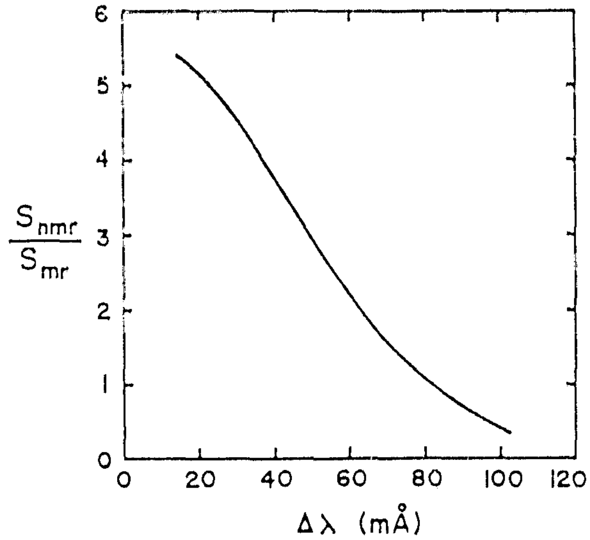

. 4 Ratio of the slope of the 5250.2 Å line profile in non-magnetic regions to the slope in magnetic regions as a function of the position of the magnetograph exit slit. This is the factor by which 5250 longitudinal magnetic measurements with Babcock-type magnetographs should be multiplied to correct for line profile changes in magnetic regions outside of sunspots.

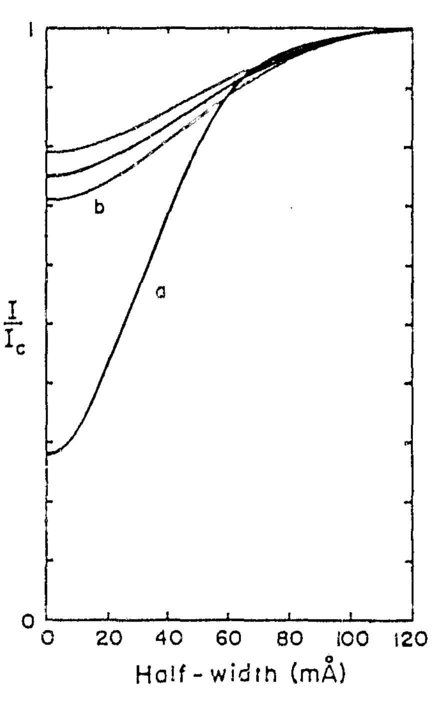

Fig. 3. One half of the width of the 5250.2 Å line as a function of intensity relative to the local continuum in (b) and out (a) of magnetic regions. Curve (a) is derived from direct observation. Curve (b) is derived indirectly (see text). About 67% of the magnetic region line profiles fall within the range indicated about curve (b).

ORIGINAL PAGE IS
OF POOR QUALITY

3. Theoretical (2) 5250 Profiles

from J.O. Stenflo (1974): "A Model of the Supergranulation Network and of Active Region Plages", Solar Phys. 42, 79.

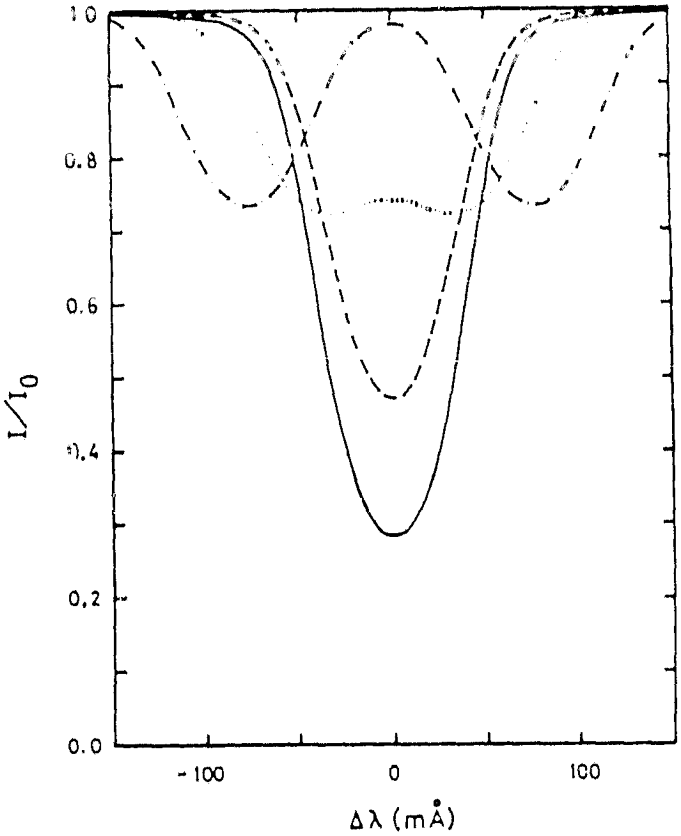

Fig. 5. Line profiles of Fe I λ5250 calculated from our plage and network model for various values of the field strength. Dashed line: $B = 0$ G. Dotted line: $B = 1000$ G. Dashed-dotted line: $B = 2000$ G. Solid line: undisturbed photosphere (HSRA), $B = 0$ G.

ORIGINAL PAGE IS
OF POOR QUALITY

4. Optical Efficiency of an Actual Magnetograph

(a) W.C. Livingston, J. Harvey, A.K. Pierce, D. Schrage, B. Gillespie, J. Simmons, and C. Slaughter (1976): "Kitt Peak 60-cm Vacuum Telescope," Applied Optics 15, 33.

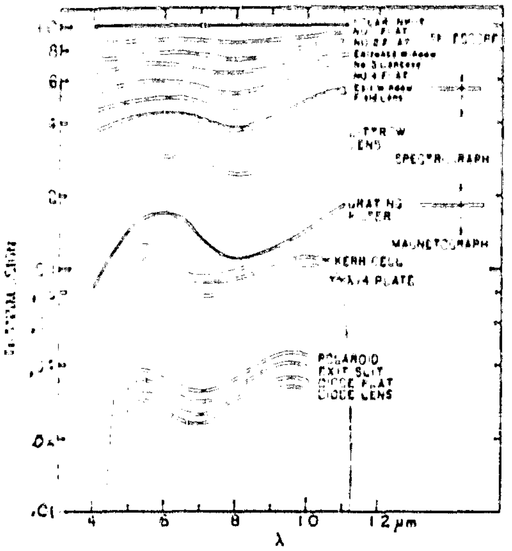

Fig 6 Where do the photons go? Measured transmission telescope, spectrograph, and accompanying magnetograph.

(b) W.C. Livingston, J. Harvey, C. Slaughter, D. Trumbo (1976): "Solar Magnetograph Employing Integrated Diode Arrays," Applied Optics 15, 40.

Table II. Optical Transmission at λ0.8688 μm

Element	Transmission	(Total) Trans.
(Telescope)[a]		0.40
Kerr cell	0.90	
RG [illegible]	0.92	
λ/4 plate	0.92	
Polaroid [illegible][b]	0.45	
(polarization analyzer)		0.34
Field lens	0.97	
Littrow lens	0.82 x 0.82	
Grating	0.45	
(spectrograph)		0.29
Exit [illegible]	0.90	
[illegible]	0.85	
[illegible]	0.92	
([illegible] assembly)		0.70
Total system		0.028

[a] See Ref. 5.
[b] Polarization effect not removed.
[c] From manufacturer's data.

In the first design (Figure 5.2a), which is a simple variation of Figure 5.1, a small amount of the light is stolen to permit the temperature measurement. It is based on the observation that the temperature signal is much larger, and that it does not needed to be evaluated as frequently. The two small detectors D3 and D4 obviously do not make the most efficient use of the reflected light, and a more elaborate scheme (involving a diagonal mirror as in Figure 5.2b) could be used if necesssary.

To achieve any fixed noise level, the configuration of Figure 5.2a would require a longer integration time than that of Figure 5.1 in direct proportion to the amount of light lost by reflection and absorption (i.e., the effective transmission or quantum efficiency is lower).

In the second design (Figure 5.2b) a diagonal mirror is used to physically separate the inner and outer parts of the ring plane image. Either version of the polarizing mask could be used, but that of Figure 2.4.1 was chosen for clarity. The design suffers from a relatively inefficient use of the rectangular detectors which is likely to increase the noise and dark current problems. Since the two independent measurements of the field strength can be averaged together, the individual measurements can be a factor of $\sqrt{2}$ coarser than required in design 5.1, however, the light level is only half as much, and for a noise-limited photodiode, according to equation 4.2.7, the intrinsic noise level would be twice as great. The upshot is that if the same diodes are used in both cases, twice as long an integration time would be required to achieve the same noise level. On the other hand, if a photon-counting-limited detector were used, no increase in integration time would be needed.

5.3 A Design Using Only One Wing

As indicated in Section 3.5.6, and again in Section 4.2.7, there is for any line and field strength a reasonable advantage (a factor of 1.5 - 1.75 in integration time) to be gained by operating the magnetograph in one wing only. Figure 5.3 suggests one possible design in which this is done:

C-2

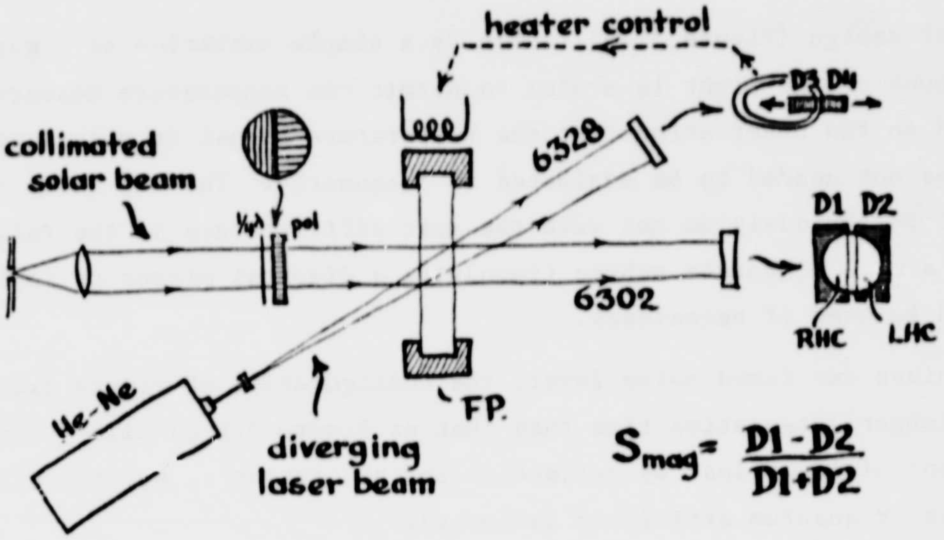

Figure 5.3: A design using the filter in a single wing of the solar line. The laser reference source is added for temperature control.

Since two detectors are used for the magnetic signal, the advantage in integration time would be relative to design 5.1, which is already the most efficient of those suggested so far. The disadvantage of the design is that it cannot be used in a Doppler mode and therefore needs some auxilliary means of temperature control. In the one suggested, a slightly divergent laser beam is used. Since it is unlikely that there will be a bandpass exactly at the wavelength of the laser light when the filter temperature is correct for the solar line, the laser beam is passed through at an angle. The transmission pattern will then be a somewhat flattened annulus whose diameter varies with the temperature and whose width depends on the FWHM of the filter. The laser light annulus is monitored by the detectors D3 and D4 which are connected by a servo mechanism to the temperature controller. The operating temperature is varied by shifting the lateral position of D3 and D4. The temperature control requirements are similar to those in the full ring plane mode (Section 4.4). An error of 20 mÅ would decrease the magnetic signal by about 15%. The problem is that one would need to have a table giving the operating position for each point on the Sun.

When using a single wing there should be a slight additional advantage to using the blue one, since the absorption core from the undisturbed photosphere will be shifted in that direction relative to the profile of the magnetic features. Thus, in the blue wing a lower background level will be found at the point of maximum magnetic modulation.

If the laser idea is unacceptable, a modification is possible (cf. Section 5.6) in which a segmented quarter-waveplate is placed over the objective and a polarizing prism is used to produce two appropriately skewed but individually collimated beams which could be passed through the Fabry Perot at slightly different angles, one corresponding to the red wing, and the other to the blue. Each transmitted beam could then be sampled in the fashion indicated in Figure 5.3 and they would provide independent estimates of the magnetic field. Temperature information could be extracted from the difference in the two total intensities, in the same manner as indicated in Figure 5.6.

5.4 Clarification of the Designs

5.4.1 What are the Detectors?

As indicated in Section 4.2 there are a number of possibilities for what the detectors might be, and the fact that they happen to have been represented by two neighboring rectangular areas does not mean to imply that the PIN-Spot/2D detector has been chosen. Figure 5.4.1a illustrates a number of ways in which combinations of photodiodes or photomultipliers could be used to equivalently sample the detection sectors:

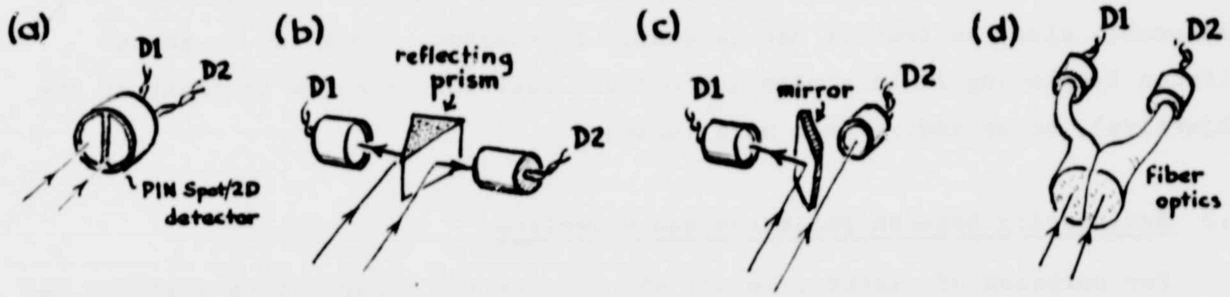

Figure 5.4.1a: Four practical possibilities for the detector pairs.

They could equally well be portions of the CID image plane, either obtained by software by summing over the appropriate pixels, or by a hardware modification:

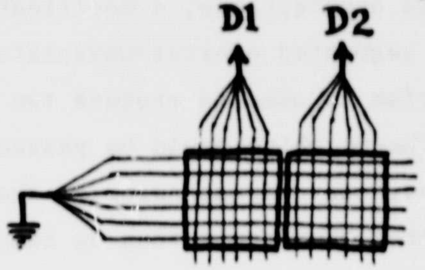

Figure 5.4.1b: An electronic modification of the CID to obtain a detector pair.

5.4.2 How Large are They?

The figures are also somewhat unclear in that they seem to show the detectors as being about the same size as the objective lens. In fact, the actual physical dimensions are likely to be extremely small (cf. Table 4.2.4 and Figure 4.2.2d). For example, to provide a scale one might note that for a 2" objective and an f/45 beam the actual size of the 10 arc second field stop would be about 0.1 mm. The ring plane image will be larger, of course, depending on how far back is is placed. If too large, it can be reduced down to the size of the detectors by means of an additional converging lens. On the other hand, it is desireable for the polarization analyzer to really be of reasonable size, so that it can be easily fabricated. This can be accomplished by placing it in a more appropriate position (such as in front of the objective), or by adding even more lenses.

5.5 Reciprocity Between Polaroids and Waveplates

For purposes of clarity, in all the figures the polarization analyzer has been shown as consisting of the combination of a single simple quarter waveplate and a segmented polaroid. While this is much easier to draw, this configuration is optically completely equivalent to a segmented quarter waveplate followed by a single simple polaroid:

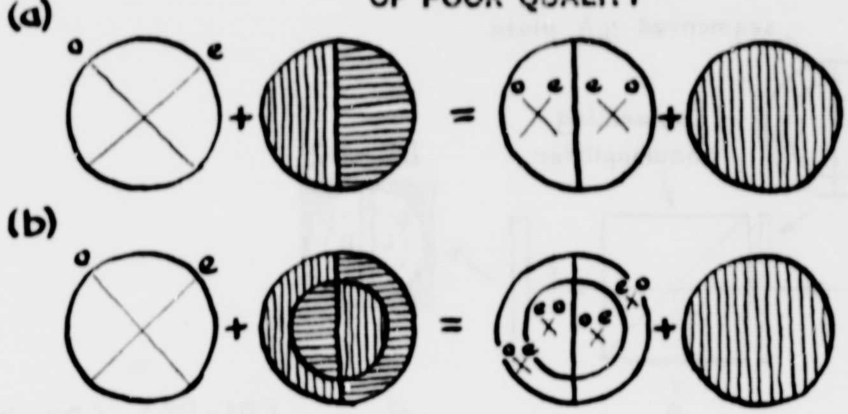

Figure 5.5: Demonstration of reciprocity between polaroids and quarter-waveplates. The configurations on right and left are optically equivalent.

5.6 A Method for Doubling the Light Level

In the designs of Sections 5.1 thru 5.3 half of the light incident on the objective is lost by absorption in the polaroid element of the polarization analyzer. If we use the concept of Section 5.5, that element could as easily as not be a single simple sheet of linear polaroid; and if that is the case it could equally well be a polarizing beam splitter, in which case both the transmitted and the reflected beams would provide complementary and equally useable polarized ring-plane images. Figure 5.6 indicates how this modification could be applied to design 5.1, in which the simple polaroid has been replaced by a segmented quarter-waveplate of the configuration shown in Figure 5.5b cemented to a suitably oriented polarizing beamsplitter.

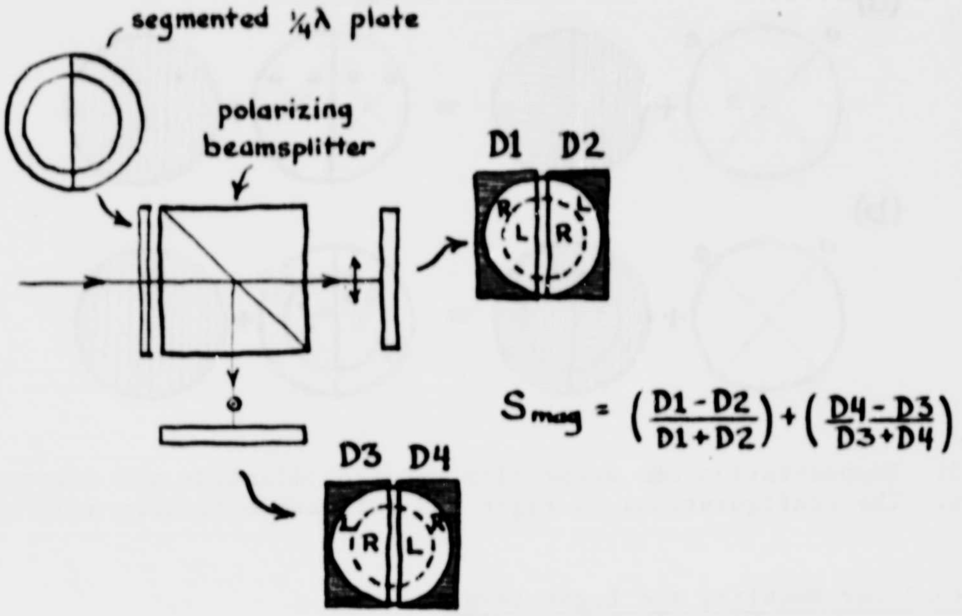

Figure 5.6: Design 5.1 modified to permit dual, simultaneous focal planes.

If there are no losses in the beamsplitter, the noiseness of the averaged measurement would be $\sqrt{2}$ better than that for either focal plane separately, which means that the integration time could be reduced by a factor of 2. If the detectors were of the noise-limited variety governed by equation 4.2.7, and if it were possible optically to invert and superimpose the two focal plane images on the same detector, so that the <u>intensity</u> as well as the light level is increased by a factor of 2, then an even greater improvement in integration time could be realized (up to a factor of 4).

A further advantage of the beamsplit design is that erroneous signals due to non-uniformities over the aperture (shadowing, temperature gradients, fingerprints and atmospheric effects) will tend to appear in the two channels with opposite signs, and therefore cancel in the average.

6. Conclusions

1. The basic outlook for the success of a compact Fabry Perot magnetograph is favorable.

2. Although currently referred to as a "telecentric" system, the only corrector lens which is likely to be needed is the one to re-image the objective, and that only in cases where (to accomodate the detectors) it is desired to have a final "ring plane" image smaller than, or comparable in size to the field stop (§ 2.3).

3. Of the spectral lines which might be used in the visible, λ6302 seems to be about as good as any, and much better than some which have been used successfully in the past (λ5324). The only better lines, at least among the simple Zeeman triplets, seem to be in the infra-red (§§ 3.5 & 4.2.7).

4. Efforts to supress the filter wings help slightly in improving the magnetic response; however, at λ6302, for a given signal to noise, the existing filter pair is already within 2.8X of the ultimate integration time which could be achieved with a perfectly square bandpass. The Hoya filters, if successful and combined incoherently would be within 1.6X of it (finesse = 20). If combined coherently they would presumably be slightly closer still (§ 3.5.3).

5. If the position of the line center must be monitored to maintain temperature control, then at 6302 the best magnetic response can be obtained by having the objective lens (and hence the ring plane "image") correspond to a wavelength range of approximately ± 90 mÅ about line center, which dictates a beam of about f/45 through the filter. Portions of the objective lens transmitting light outside this band (and also within ± 10 mÅ of line center) are counter-productive, and would be rejected at the detector, if present (§ 3.5.2).

6. If the temperature can be monitored separately, the f-number could be increased (i.e. the beam made more parallel) so the whole objective would be used near the point of maximum sensitivity in one wing of the line. This would reduce the integration times required for a fixed signal-to-noise by about a factor of 1.5 - 1.8 (§§ 3.5.6 and 4.2.7).

7. On the other hand, it might for some purposes by desireable to decrease the f-number (i.e. make the beam more divergent) so that one of the

ORIGINAL PAGE IS
OF POOR QUALITY

nearby telluric lines could be used as an absolute velocity reference. This would require a minimum spectral range of about 400 mÅ, which would reduce the light available for magnetic measurements and increase the integration times by a factor of 2 to 5, depending on the detectors (§ 4.7). A better way to make velocity measurements would be to use a separate temperature monitoring system (§§ 4.7 and 5.3).

8. The major source of uncertainties regarding the predicted performance of the instrument are (a) knowledge of the true weak field configuration on the sun; and (b) uncertainties regarding the behavior of the spectral lines in the unresolved magnetic elements (§§ 3.1 and 3.5.5).

9. Nonetheless, it is clear that the basic problem is not so much what is or how to improve the expected signal, but rather, how to efficiently sample and process it. At 6302, the expected magnetic signal corresponding to the lowest contours on the Mount Wilson daily magnetograms ("5 gaus") is about 2×10^{-3} (Table 3.5.3b). We would like to be able to detect this with a signal to noise of 4, that is, with a noise level of about 5×10^{-4} (§ 3.4.2). With a 2 inch aperture, a 10 arc sec sampling area, and optmistic assumptions about the obtainable atmospheric and optical transmissions (§ 3.4.3) we would expect to have, in the optimum ring-plane mode, a light level of about 1×10^{8} photons/sec for each circular polarization (using half of the objective). With an ideal detector, the desired noise level could be reached in about .02 seconds (Table 3.5.3b).

10. Actual detectors will be limited by quantum efficiency and noise. If the detector is in a quantum efficiency (photon statistic) limited mode, the integration times required will be in (inverse) proportion to the light level. In the noise limited regime (very low light levels), the integration times are (inversely) proportional to the <u>square</u> of the light level. The behavior of the CID is even more complicated because the effective quantum efficiency depends on the charge level. In general, the best results, both from the standpoint of noise and dark current will be achieved by using detectors of the smallest possible physical area. For available detectors, even if the design is modified towards higher light levels at the expense of signal strength, the best achievable integration times are about an order of magnitude larger than the ultimate ones (§ 4.2).

11. In general, except possibly for purposes of set-up and demonstration, a complete ring-plane detection system would not be required. By appropriate choice of the polarization analyzing mask, only two simple detectors would be required to measure longitudinal magnetic field strengths, and four to extract both temperature and magnetic information (§ 2.4 and §5).

12. One project of modest scientific interest which *could* be performed using the basic compact magnetograph with a full ring-plane configuration and CID detector would be the simultaneous measurement of the strength of circular polarization throughout a line profile; which would require a much longer integration time and/or larger aperture. If the sampling area is sufficiently small, the shape of the magnetically disturbed profile can be inferred. Even for large sampling areas, regions in which the majority of the field is above about 1500 gauss would show a distinctive signature. It is difficult to see, however, how these results would improve over those which could be obtained by the microdensitometry of photographic spectra obtained simultaneously in the two circular polarization.

13. The temperature-monitoring problems do not seem to be as severe as might be imaged. At $\lambda 6302$, signals of as large as $\sim 10\%$ ($\approx 0.5^{\circ}$C) could be allowed to develop without noticeably affecting the magnetic sensitivity (§ 4.4).

14. Because of the intensity-dependence of the relative detector noise levels, not all focal plane configurations are equivalent. To achieve the optimum integration time, care should be taken to make the most efficient possible use of the available light, and to minimize the number of detectors, particularly if photodiodes are used (§ 5).

15. The introduction of a KDP crystal to modulate the magnetic signal would offer many potential advantages, both in terms of reducing the number and complexity of the detectors, and in alleviating the possibility of extraneous imbalances. The disadvantages are minimal, and it would seem that this option should be reconsidered (§ 4.8).

16. In all cases, the efficiency can be improved by substituting polarizing beam-splitters for the polaroid elements. In effect, two independent focal planes are created, the results from which can be averaged (§ 5.6).

17. If spatial resolution is not a primary concern, the dynamic range of the measurements (for a given integration time) can be increased considerably if a larger sampling aperture is used, particularly for photodiode detectors (§ 3.6). An increase in the size of the objective would have a similar effect.

APPENDIX: Detector Characteristics

CID Characteristics

from Richard S. Aikens (1980): "A Large CID for Use in Astronomy," AURA Engineering Technical Report #66 (KPNO).

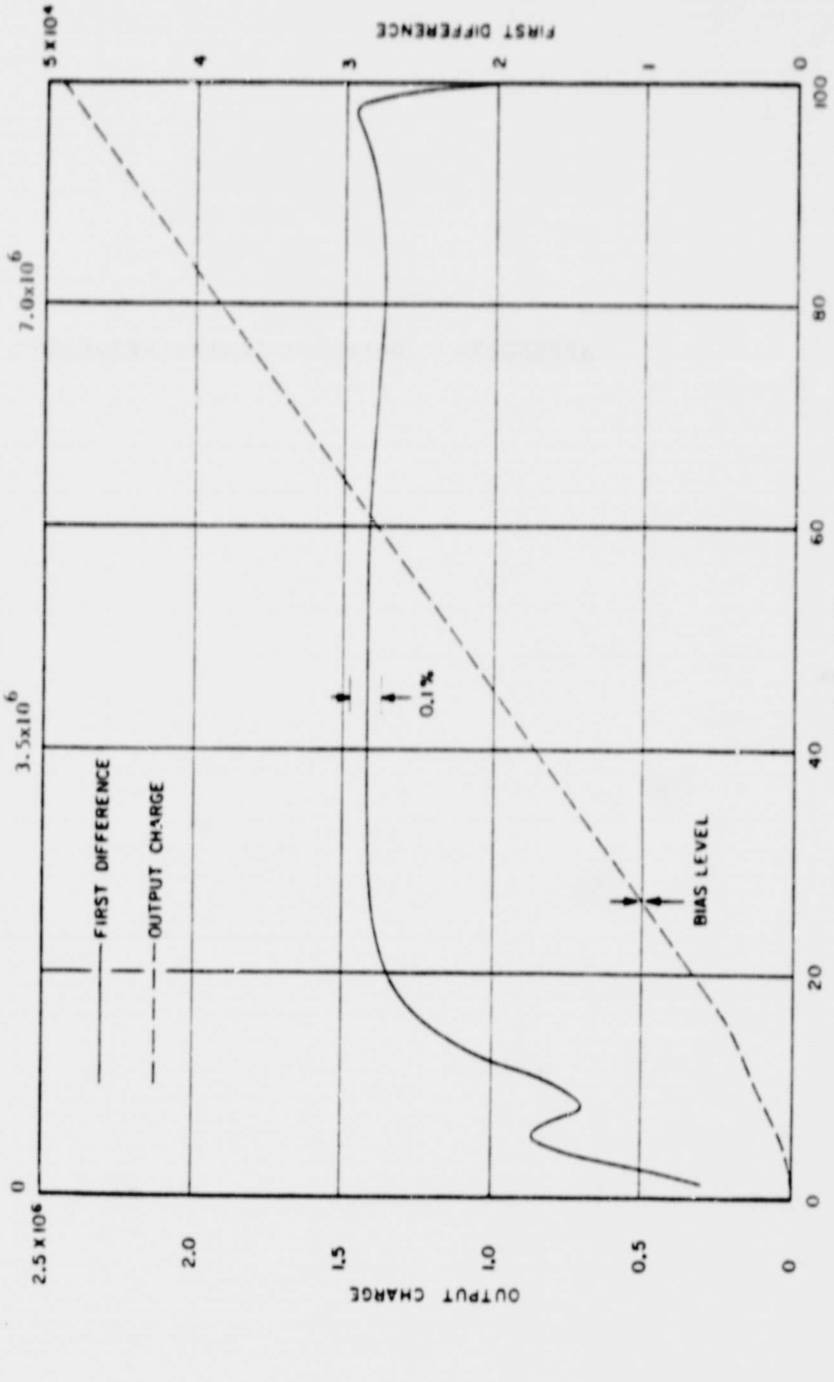

CID LINEARITY DATA

ORIGINAL PAGE IS
OF POOR QUALITY

POSITION SENSING DETECTORS
PIN Spot/2D, Spot/4D

UNITED DETECTOR TECHNOLOGY, INC.

UDT's "Spot" series position sensors are bi-cell or quadrant detectors ideally suited for a wide range of nulling and centering applications.

The devices consist of two or four discrete elements on a single substrate with an active output lead from each element. When a light beam is centered on the detector (null or center position is the intersection of active elements) output current from each quadrant is equal. As the beam moves, current imbalance indicates off-center position. These devices exhibit excellent stability over time and temperature, high responsivity and fast response times necessary for pulse operation.

The PIN-Spot/2D is a single axis position sensor with two discrete elements. The PIN-Spot/4D quadrant detector is ideal for systems allowing light movement in two axes.

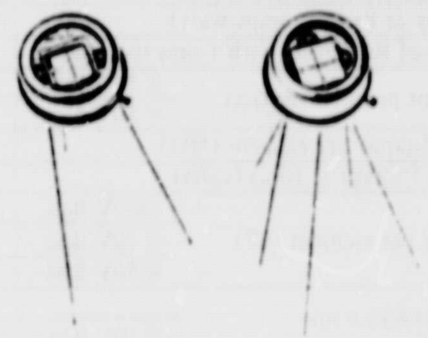

FEATURES:

- Broad frequency response
- Fast rise time
- Low capacitance
- High accuracy, long term stability of null position
- Easy hookup

APPLICATIONS:

- Lens manufacturing
- Feedback control systems
- Guidance systems
- Laser alignment
- Machine tool alignment
- Targeting
- Process machinery alignment

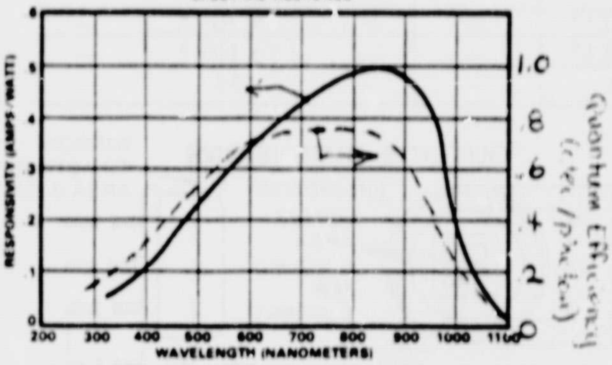

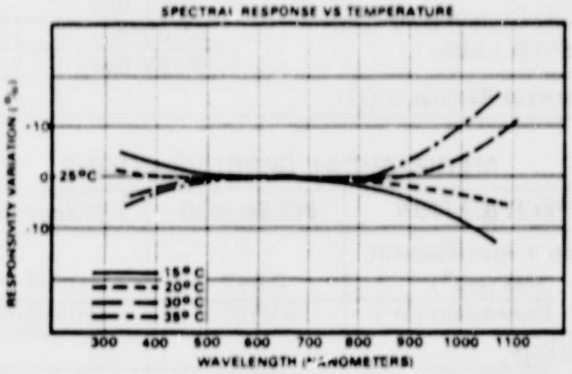

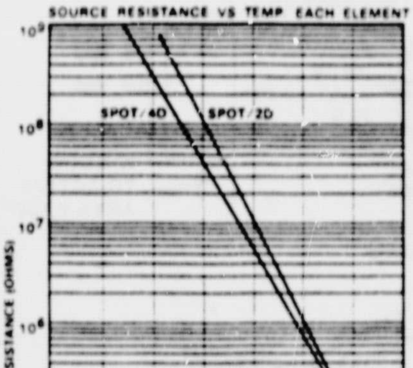

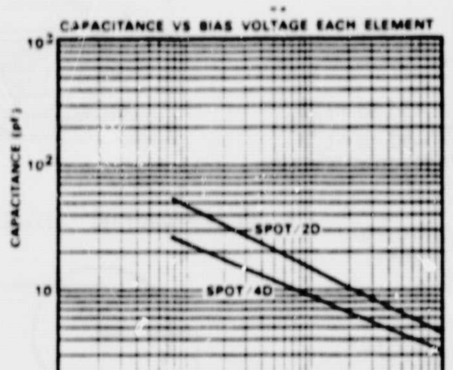

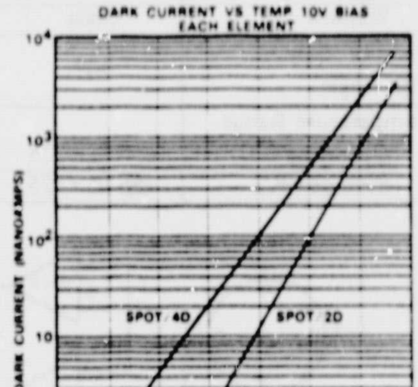

ELECTRICAL CHARACTERISTICS

PARAMETER AND (UNITS)		PIN-Spot/2D MIN	PIN-Spot/2D TYP	PIN-Spot/2D MAX	PIN-Spot/4D MIN	PIN-Spot/4D TYP	PIN-Spot/4D MAX
Recommended Mode of Operation		Photovoltaic/Photoconductive			Photovoltaic/Photoconductive		
Spectral Range @ 5% Peak (nm)		350–1100			350–1100		
Responsivity at Peak λ (amps/watt)		0.4	0.5	–	0.4	0.5	–
Uniformity of Response (with 1 mm spot dia)		–	±2%	±5%	–	±2%	±5%
Dark Current per element (μa)	@ 10V Bias	–	0.002	0.05	–	0.002	0.05
	@ 50V Bias	–	0.006	0.15	–	0.006	0.15
Source Resistance per element (MΩ)		–	60	–	–	70	–
Breakdown Voltage @ 10 μa (volts)		50	100	–	50	100	–
Capacitance per element (pF)	@ 0V Bias	–	54	81	–	29	44
	@ 10V Bias	–	15	22	–	7	10
	@ 50V Bias	–	6.7	10	–	4	6
Rise Time at 632.8 nm 10%–90% (ns)		–	–	–	–	–	–
	@ 10V Bias	–	10.0	–	–	10	–
	@ 50V Bias	–	10.0	–	–	10	–
Fall Time at 632.8 nm 90%–10% (ns)		–	–	–	–	–	–
	@ 10V Bias	–	10.0	–	–	10	–
	@ 50V Bias	–	10.0	–	–	10	–
Frequency Response at 632.8 nm into 50Ω Load (MHz)		–	–	–	–	–	–
	@ 10V Bias	–	35	–	–	35	–
	@ 50V Bias	–	35	–	–	35	–
Max. Output for 10% Linearity (ma)	@ 0V Bias	–	0.2	–	–	0.5	–
	@ 10V Bias	–	0.25	–	–	1.0	–
NEP @ Peak λ, 1 kHz, 10V (w/Hz$^{1/2}$)		–	9×10^{-14}	–	–	9×10^{-14}	–
Noise Current (rms amp/Hz$^{1/2}$) @ 1 kHz	@ 0V Bias	–	2×10^{-14}	–	–	2×10^{-14}	–
	@ 10V Bias	–	3×10^{-14}	–	–	3×10^{-14}	–
	@ 50V Bias	–	5×10^{-14}	–	–	5×10^{-14}	–
Forward Resistance (Ω)		–	45	–	–	55	–

MECHANICAL SPECIFICATIONS

SPECIFICATION	PIN-Spot/2D	PIN-Spot/4D
Active Area/Element		
Area (cm^2)	0.032	0.016
Dimensions (in.)	0.05x0.1	0.05x0.05
Package		
Type	TO-5	TO-5
Window	Glass	Glass
Field of View Full Angle	96°	96°
Temperature Range		
Operating (°C)	-55 to +125	-55 to +125
Storage (°C)	-55 to +125	-55 to +125

OUTLINE DIMENSIONS

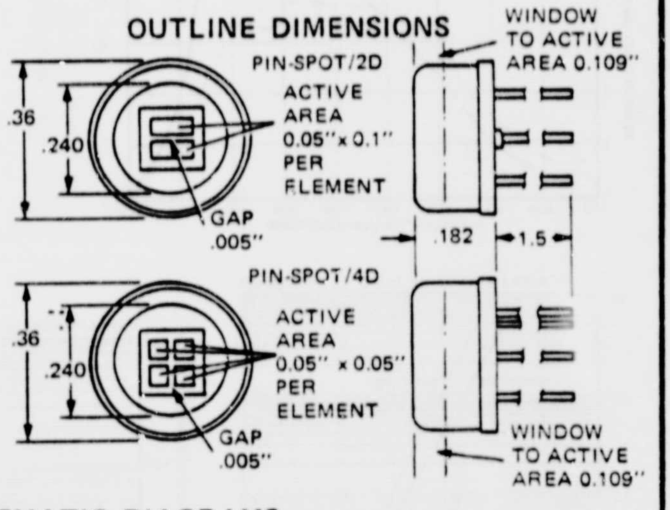

SCHEMATIC DIAGRAMS

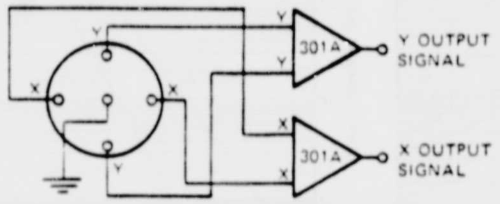

TYPICAL CONNECTIONS FOR PIN-SPOT/4D
TO MODIFIED UDT 301A AMPLIFIER*

TYPICAL CONNECTIONS FOR PIN-SPOT/2D
SINGLE AXIS DETECTOR TO UDT 301A AMPLIFIER

*AMPLIFIER BIAS POLARITY MUST BE CHANGED

SPECIFICATIONS SUBJECT TO CHANGE WITHOUT NOTICE

D-017-0777

UNITED DETECTOR TECHNOLOGY, INC.

2644 30TH STREET, SANTA MONICA, CA 90405 ■ TELEPHONE (213) 396-3175 ■ TELEX 65-2413

Data Sheet No. 9F010

LOW NOISE SERIES

UNITED DETECTOR TECHNOLOGY INC.

PIN SILICON PHOTODIODE ULTRA LOW DARK CURRENT ULTRA LOW NOISE

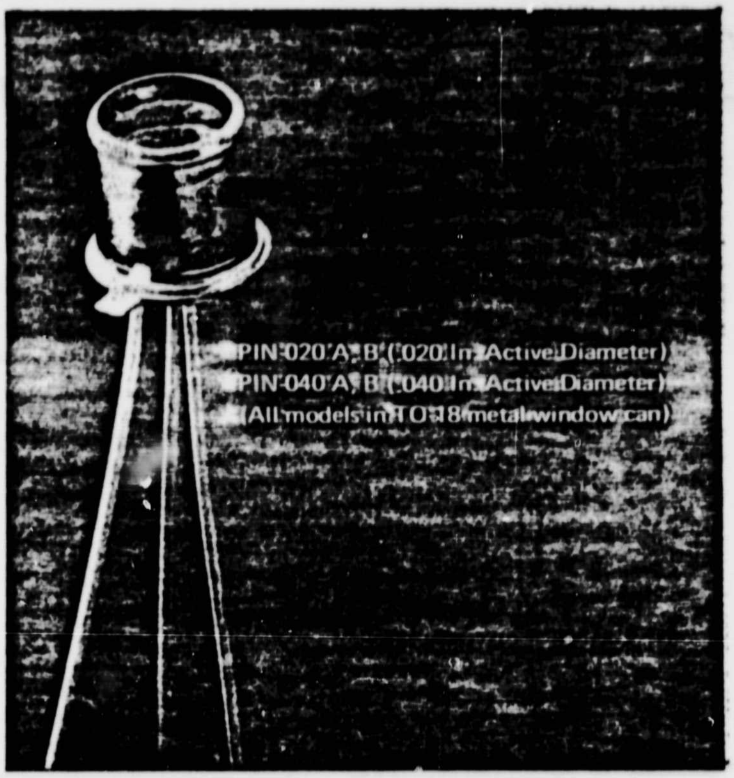

PIN-020 A, B (.020 In. Active Diameter)
PIN-040 A, B (.040 In. Active Diameter)
(All models in TO-18 metal window can)

Description

The UDT Low Noise Series (Model 020 A, B and Model 040A, B) of PIN photodiodes offer the lowest leakage current and lowest noise on the market. They are planar passivated and hermetically sealed. The detector active element is electrically isolated from the case.

The quantum detection efficiency is constant over ten decades of light intensity, providing a linear output current signal with input light level. The speed of response is less than 5 nanoseconds, allowing the observation of laser pulses of a few nanoseconds. The frequency response extends from dc to over 100 MHz. Both biased (photoconductive) and unbiased (photovoltaic) operation give excellent results with this device.

UNIQUE FEATURES

- 50×10^{-12} A leakage (PIN–020A)
- 200×10^{-12} A leakage (PIN-040A)
- 6×10^{-15} W N.E.P. (PIN-020A)
- Planar Passivated
- Hermetically Sealed TO-18 Metal Can
- Photodiode Isolated from Case

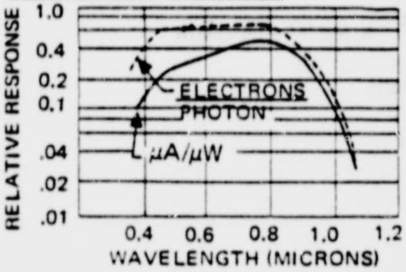

Applications

Because of their unrivaled low leakage current and low noise, these devices are especially suited to low light level detection systems. They are currently being used in star trackers, earth resources scanners, and spectrophotometers.

Specials

The low leakage characteristics of these devices can be built into many custom array geometries by UDT.

PIN SILICON PHOTODIODE ULTRA LOW DARK CURRENT ULTRA LOW NOISE

UNITED DETECTOR TECHNOLOGY, INC.
2644 30TH STREET, SANTA MONICA, CA 90405 • TELEPHONE (213) 450-8585 • TELEX 65-2413

ORIGINAL PAGE IS
OF POOR QUALITY

ELECTRICAL AND OPTICAL CHARACTERISTICS

	Pin-020A			Pin-020B			Pin-040A			Pin-040B			Units
	Min	Typ	Max	Min	Typ	Max	Min	Typ	Max	Min	Typ	Max	
Dark Current													
−5 V		50	150			800		200	400			4000	pA
−10 V		75	250			1000		300	600			6000	pA
Responsivity Peak		.42			.42			.42			.42		A/W
N.E.P. 1000 c.p.s. Center 1 c.p.s. Bandwidth 1.5 V Bias 8500 Å		6×10^{-15}			2×10^{-14}			10^{-14}			9×10^{-14}		W
Capacity													
−5 V		5			5			20			20		pF
−10 V		4			4			16			16		pF
−20 V		3			3			12			12		pF
Response Time													
20 V, 50 Ω			5			5			5			5	ns
Maximum Steady Reverse Voltage			25			25			25			25	V
Active Diameter		.020			.020			.040			.040		in.
Active Area		2×10^{-3}			2×10^{-3}			8×10^{-3}			8×10^{-3}		cm^2

MECHANICAL DETAIL

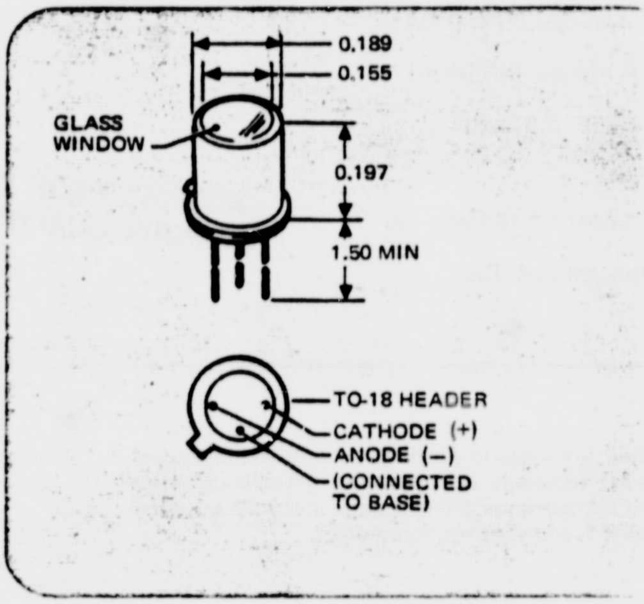

EQUIVALENT CIRCUIT

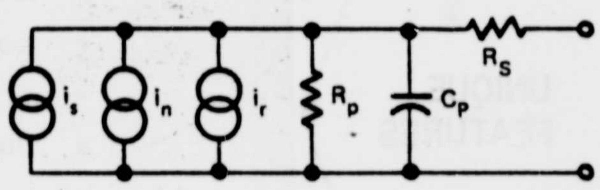

i_s = Signal current ≈ 0.5 μA/μW

i_n = Shot noise current

< 3×10^{-15} A/Hz$^{1/2}$ PIN-020A

< 10^{-14} A/HZ$^{1/2}$ PIN-040A

i_r = Dark current

R_p = ≈ 10^{11} Ω

R_S = < 50 Ω

UNITED DETECTOR TECHNOLOGY, INC.

APPENDIX

Line and Magnetograph Characteristics

ORIGINAL PAGE IS
OF POOR QUALITY

1. Unpolarized 5250 Profiles

(a) J. Harvey & W.C. Livingston (1969): "Magnetograph Measurements with Temperature Sensitive Lines", Solar Phys. 10, 283.

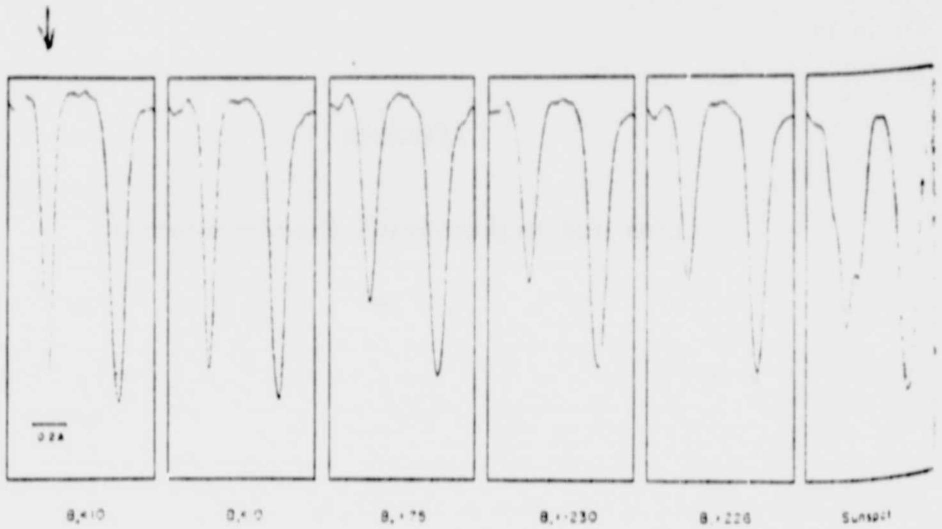

Fig. 2. Double-pass photoelectric scans of 5250.22 Å (left) and 5250.65 Å (right) with one arc second resolution in regions with various longitudinal magnetic-field strengths as measured with the 5373.7 Å line and given in units of gauss. It is very likely that the 5373.7 Å line is temperature sensitive and therefore the magnetic fields are probably underestimated by a factor of two or more

(b) G.A. Chapman & N.R. Sheeley, Jr. (1977): "An Improved Measurement of a Spectrogram of a 'Gap'", Solar Phys. 51, 61.

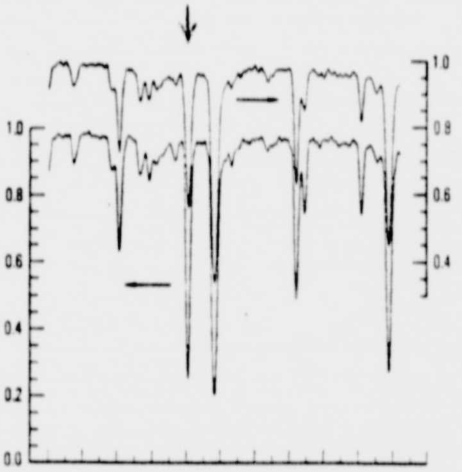

Fig. 2. The spectrum of the quiet Sun and the 'gap' covering the region from 5237 Å to 5253 Å in three parts. The facular spectrum is shifted upwards by 0.2 in I/I_c for clarity. The wavelength scale is 0.5614 Å between each large tick mark on the abscissa and runs left to right on each. The arrows indicate the correct scale for that portion of the spectrum.

2. Inferred Single-Component Profile from Harvey and Livingston (1969)
(based on a weak-field interpretation?)

MAGNETOGRAPH MEASUREMENTS WITH TEMPERATURE-SENSITIVE LINES 291

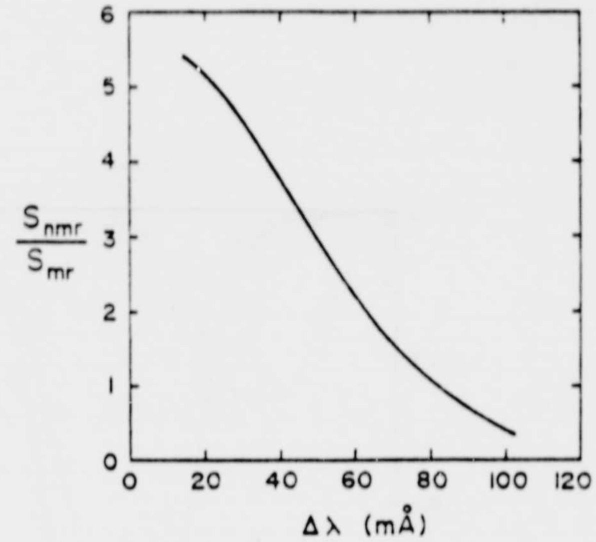

4. Ratio of the slope of the 5250.2 Å line profile in non-magnetic regions to the slope in magnetic regions as a function of the position of the magnetograph exit slit. This is the factor by which 5250 longitudinal magnetic measurements with Babcock-type magnetographs should be multiplied to correct for line profile changes in magnetic regions outside of sunspots.

290 J. HARVEY AND W. LIVINGSTON

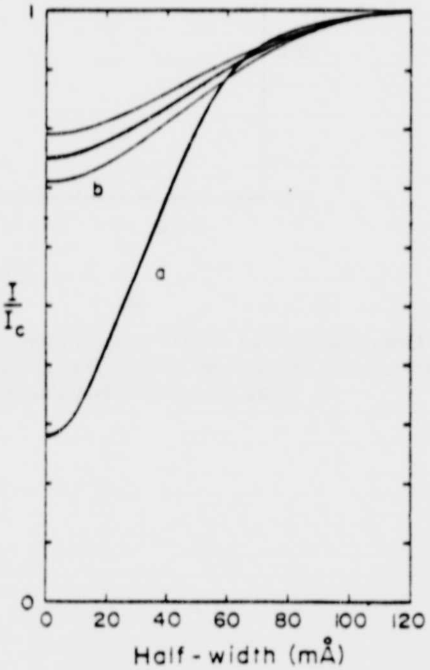

Fig. 3. One half of the width of the 5250.2 Å line as a function of intensity relative to the local continuum in (b) and out (a) of magnetic regions. Curve (a) is derived from direct observation. Curve (b) is derived indirectly (see text). About 67% of the magnetic region line profiles fall within the range indicated about curve (b).

3. Theoretical (?) 5250 Profiles

from J.O. Stenflo (1974): "A Model of the Supergranulation Network and of Active Region Plages", Solar Phys. 42, 79.

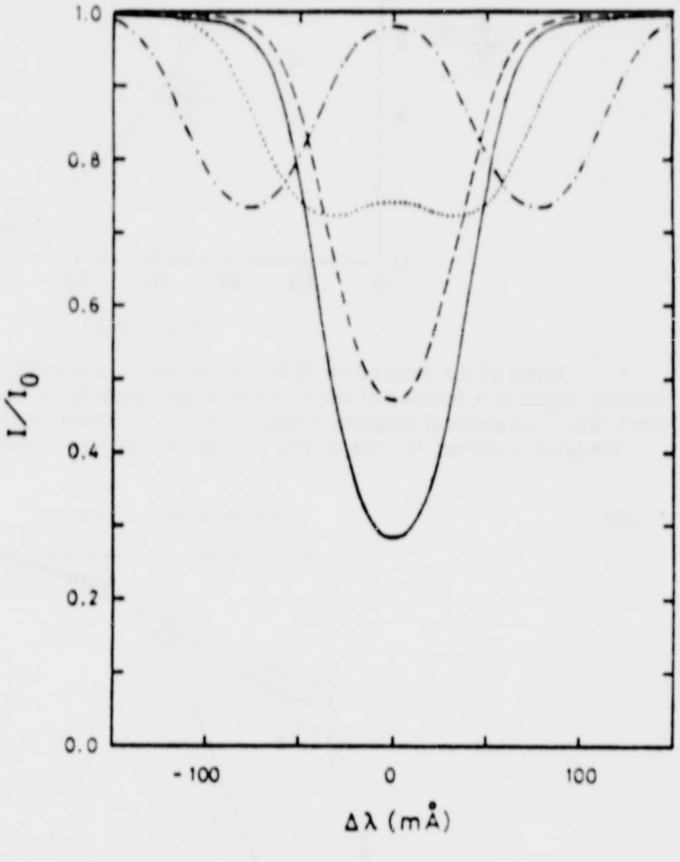

Fig. 5. Line profiles of Fe I λ5250 calculated from our plage and network model for various values of the field strength. Dashed line: $B=0$ G. Dotted line: $B=1000$ G. Dashed-dotted line: $B=2000$ G. Solid line: undisturbed photosphere (HSRA), $B=0$ G.

ORIGINAL PAGE IS
OF POOR QUALITY

4. Optical Efficiency of an Actual Magnetograph

(a) W.C. Livingston, J. Harvey, A.K. Pierce, D. Schrage, B. Gillespie, J. Simmons, and C. Slaughter (1976): "Kitt Peak 60-cm Vacuum Telescope," Applied Optics 15, 33.

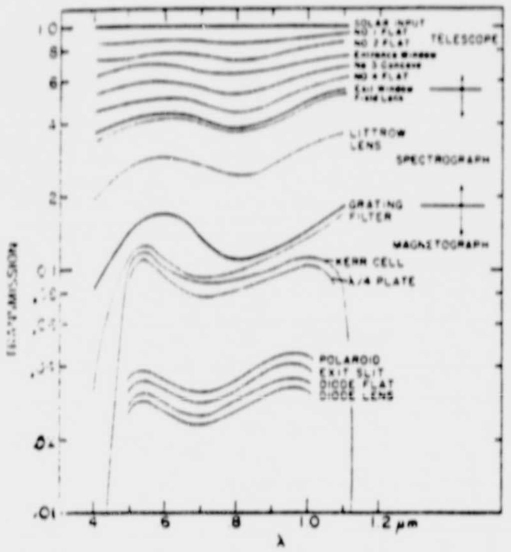

Fig. 6 Where do the photons go? Measured transmission telescope, spectrograph, and accompanying magnetograph.

(b) W.C. Livingston, J. Harvey, C. Slaughter, D. Trumbo (1976): "Solar Magnetograph Employing Integrated Diode Arrays," Applied Optics 15, 40.

Table II. Optical Transmission at λ0.8688 μm

Element	Transmission	(Total) Trans.
(Telescope)[a]		0.40
Kerr cell	0.90	
RG 715[c]	0.92	
λ/4 plate[c]	0.92	
Polaroid HN7[b]	0.45	
(polarization analyzer)		0.34
Field lens	0.97	
Littrow lens	0.82 × 0.82	
Grating	0.45	
(spectrograph)		0.29
Exit slit	0.90	
Folding flats	0.85	
Transfer lens	0.92	
(diode assembly)		0.70
Total system		0.028 ←

[a] See Ref. 5.
[b] Polarization effect not removed.
[c] From manufacturer's data.